

Aus dem Deutschen Krebsforschungszentrum Heidelberg
(Vorstand: Prof. Dr. Michael Baumann, Ursula Weyrich)
Abteilung X-Ray Imaging and CT
(Abteilungsleiter: Prof. Dr. Marc Kachelrieß)

Novel Contrast Agents in Photon-Counting Computed Tomography

Inauguraldissertation
zur Erlangung des Doctor scientiarum humanarum (Dr. sc. hum.)
an der
Medizinischen Fakultät Heidelberg
der
Ruprechts-Karls-Universität

vorgelegt von
Carlo Amato
aus
Scorrano (Italien)
2022

Dekan: Prof. Dr. Hans-Georg Kräusslich
Doktorvater: Prof. Dr. Marc Kachelrieß

To my father,
he would have been proud.

Contents

List of Acronyms	VII
List of Figures	IX
List of Tables	XI
1 Introduction	1
2 Fundamentals	5
2.1 X-ray Computed Tomography	5
2.1.1 X-Ray Generation	5
2.1.2 X-Ray Interaction with Matter	6
2.1.3 X-Ray Detection	9
2.1.4 CT System	11
2.2 Photon-Counting CT	12
2.2.1 Spectral Response and Bin Sensitivity	13
2.2.2 Material Decomposition	14
2.3 Contrast Agents in CT	16
2.3.1 High-Z Elements	17
2.3.2 Nanoparticle-based Contrast Agents	20
3 Materials and Methods	21
3.1 Assembling a New Experimental Micro-CT	21
3.1.1 Novel Photon-Counting Detector by Dectris	21
3.1.2 Gantry Geometry	23
3.1.3 CT-system and Hardware	25
3.1.4 Projection Processing and Image Reconstruction	30
3.2 A Novel Contrast Agent for Preclinical Imaging	32
3.2.1 Novel Bismuth-Based Contrast Agent by NanoPET Pharma	32
3.2.2 Characterization of the Contrast Agent Biodistribution	33
3.2.3 Multi Contrast Agent Protocol	36

3.3	Potential of High-Z Elements for Clinical Contrast-Enhanced CT .	38
3.3.1	Contrast in Photon-Counting CT	38
3.3.2	Experimental Setup	39
3.3.3	Simulations	41
3.3.4	Image Analysis	44
4	Results	47
4.1	A Novel Contrast Agent for Preclinical Imaging	47
4.1.1	Characterization of the Contrast Agent Biodistribution . .	47
4.1.2	Multi Contrast Agent Protocol	51
4.2	Potential of High-Z Elements for Clinical CT	56
4.2.1	Measurements	56
4.2.2	Simulations	60
5	Discussion	65
5.1	A Novel Contrast Agent for Preclinical Imaging	65
5.1.1	Comparison with Iodinated Contrast Agent	66
5.1.2	Multi Contrast Agent Protocol	67
5.2	Potential of High-Z Elements for Clinical CT	69
5.2.1	Comparison with EI detectors	72
6	Summary	75
7	Zusammenfassung	77
8	Reference list	81
9	Personal Publications	89
10	Curriculum Vitae	93
11	Acknowledgements	95
12	Eidesstattliche Erklärung	97

List of Acronyms

CNR	Contrast-to-noise ratio
CNRCD	CNR at unit dose and concentration
CT	Computed tomography
EI	Energy integrating
FOV	Field of view
micro-CT	Micro-computed tomography
PC	Photon counting
ROI	Region of interest

List of Figures

2.1	Example of a 120 kV x-ray spectrum	6
2.2	Attenuation coefficient of water	7
2.3	Attenuation coefficient of elements with K-edge in the diagnostic energy interval	8
2.4	Energy-integrating and photon-counting detector schematic	10
2.5	CT schematic	12
2.6	Example of the spectral response and bin sensitivity of a PC detector	14
2.7	Example of material decomposition	16
2.8	Iodinated contrast agent molecules and nanoparticles	17
2.9	Example of a 100 kV transmitted spectrum and K-edges	18
2.10	Candidate high-Z elements for CT contrast agents	19
3.1	Dectris Säntis photon-counting detector	22
3.2	Spectral response of the Dectris Säntis detector	23
3.3	Schematic of the experimental gantry geometry	24
3.4	Plots of the spatial resolution, field of view and z-coverage for the new experimental gantry	25
3.5	Experimental gantry before the assembling of the new components	26
3.6	Water cooling system and dry air supply	27
3.7	Mouse table	28
3.8	Experimental gantry after the assembling of the new components	29
3.9	Experimental gantry closed with sample table installed	30
3.10	Bad pixels and intermodule gaps inpainting at the experimental gantry	31
3.11	Ring artifact correction at the experimental gantry	32
3.12	Anaesthesia vaporizer	34
3.13	Mouse anesthetized during the acquisition	35
3.14	Schematic of the multi contrast agent protocol	37
3.15	Mouse-size multi contrast agent phantom	38
3.16	Adult liver phantom with high-Z inserts	40
3.17	Spectral response of the Siemens SOMATOM CounT	43

4.1	Time-dependent signal enhancement curves for the mouse experiments with the novel bismuth-based contrast agent	48
4.2	Mouse thorax before the injection	48
4.3	Mouse abdomen before the injection	49
4.4	Mouse thorax right after the injection	50
4.5	Mouse thorax 5 h after the injection	50
4.6	Mouse abdomen 3.5 h after the injection	51
4.7	Multi contrast agent protocol: CT images	52
4.8	Material decomposition of the mouse thorax right after the injection of iodine	53
4.9	Material decomposition of the mouse shoulders 3 h after the injection of iodine	54
4.10	Material decomposition of the mouse thorax 3 h after the injection of iodine	54
4.11	Material decomposition of the mouse shoulders after the injection of bismuth	55
4.12	Material decomposition of the mouse thorax right after the injection of the bismuth agent	55
4.13	Measured and simulated CNRCD vs. tube voltage for the different high-Z solutions	57
4.14	Measured and simulated CNRCD vs. the high energy threshold for the different high-Z solutions	58
4.15	Material decomposition CNRCD vs. energy threshold for the different high-Z solutions	59
4.16	Material map of gadolinium and material map of bismuth for the adult liver phantom	60
4.17	Infant patient simulations: CNRCD and dose reduction vs. tube voltage	61
4.18	Adult patient simulations: CNRCD and dose reduction vs. tube voltage	62
4.19	Obese patient simulations: CNRCD and dose reduction vs. tube voltage	63
5.1	Attenuation coefficients of iodine and bismuth	66
5.2	Example of the importance of multi contrast agent protocols . . .	68
5.3	Schematic of a multi contrast agent protocol for abdominal imaging	69
5.4	Comparison between PC and EI detectors	73

List of Tables

3.1	Technical specifications of the Dectris Säntis PC detector	22
3.2	Mouse experiments parameters	34
3.3	High-Z solutions for measurements	41
3.4	Parameters for measurements and simulations at the SOMATOM CounT	42
3.5	Ideal high-Z water solutions for simulations	44
4.1	CNRCD improvement of one threshold vs. two thresholds	58
5.1	Summary of the CNRCD for different high-Z solutions, patient sizes and filtration settings	70
5.2	Summary of the best performing high-Z elements for contrast enhanced PC-CT	71

1 | Introduction

Computed tomography (CT) is an imaging modality developed by Godfrey N. Hounsfield (Hounsfield 1972) and Allan M. Cormack (Cormack 1963), who were awarded with the Nobel prize for Medicine in 1979. CT exploits X-ray to measure the 3D distribution of the attenuation coefficient of matter in a non-invasive/non-destructive way, and has countless applications in both the medical and industrial fields. Because of its high spatial and temporal resolution, and relatively short acquisition times, CT is one of the most essential imaging modalities in clinics, with around 300 million examinations performed every year (Shahid et al. 2020).

Approximately 40% of CT scans are performed with the injection of contrast agent, which distributes in different tissues and locally enhances the attenuation coefficient thanks to the contained heavy element. Contrast agents are used for cardiovascular imaging, detection of organ perforations, cancer monitoring, and patient triage in emergency settings. All the contrast agents approved for intravascular injection in CT are based on iodine. The first iodine-based contrast agent was developed by Guerbet in 1901 shortly after the discovery of X-rays (Röntgen 1898). In the past century, iodine-based contrast agents have been thoroughly investigated and developed to improve their safety profile and efficiency. Despite more than one century of research, the fundamental structure containing the iodine (tri-iodinated benzene ring) remained almost unchanged. From a physical point of view, iodine may not be the best heavy element concerning the x-ray attenuation properties. One of the main properties to consider is the presence of a K-edge in the diagnostic energy range (20 keV-150 keV). The K-edge is a rapid increase of the attenuation coefficient, and for iodine it is located at 33.2 keV, which is at relatively low energy if compared to the usual X-ray spectra used in CT. Other elements, heavier than iodine and with a K-edge at higher energies, may in principle provide more contrast and other benefits than iodine. The possibility of exploiting heavier elements as contrast agent has to face the challenge of biocompatibility, since some of them are toxic or not stable. Recently, structures like nanoparticles and liposomes have been investigated to densely pack a specific element and increase its biocompatibility (Bhavane et al. 2013; Aydogan

et al. 2010; Rabin et al. 2006). Nanoparticles can be manufactured with a size up to hundreds of nm, which is much larger than the size of usual iodinated contrast agents, which is between 1.3 nm and 2.1 nm (Fitzgerald et al. 2016). Therefore, nanoparticle agents are cleared from the system via the liver and not by the faster renal system. This means that their circulation time is much longer than usual contrast agents. This behavior is defined as *blood-pool*, and it is of interest for cardiac imaging, especially for preclinical applications. An additional coating can be applied to nanoparticles to improve their biocompatibility, to increase the circulation time, or to target specific tissues.

Another recent innovation in CT has been the introduction of photon-counting (PC) detectors (Ballabriga et al. 2016), which substantially differ from conventional energy-integrating (EI) detectors commonly used in state-of-the-art scanners. PC detectors are based on a semiconductor technology that allows, in combination with a fast front-end electronic, individual photon counting and assigns to each detected photon an equal weight. Conversely, EI detectors use scintillators coupled with photodiodes, which generate a signal proportional to the energy of the impinging photon. Furthermore, the signal generated by all the photons detected within one time frame is integrated and the information about each individual photon is lost. PC detectors have many advantages compared to EI detector, especially concerning image noise (Klein et al. 2020), spatial resolution (Mannil et al. 2018) and iodine contrast (Sawall et al. 2020b). One of the main features of PC detectors is the possibility to have adjustable energy thresholds in the front-end electronic. Such thresholds can be used to classify the detected photons in different energy bins according to their energy and therefore obtain spectral information. Spectral imaging is achievable also with EI detectors, but using strategies like dual-source CT, rapid kV-switching, twin beams, or sandwich detectors (Faby et al. 2015). Spectral information can be used to differentiate between materials whose attenuation coefficients have different dependencies on the photon energy. This process is called material decomposition (Alvarez et al. 1976; Roessl et al. 2007) and it is extremely valuable in scenarios when two different materials or tissues have the same attenuation value, hence no contrast is present. One of the main examples of this situation is the imaging of calcified plaques, which may have the same attenuation of the iodine-enhanced vasculature. This can lead to an underestimation of the eventual stenosis caused by the plaque or the plaque can remain undetected (De Santis et al. 2019).

The combination of new high-Z contrast agents and novel PC detectors can unlock new imaging technologies and provide new diagnostic information. The K-edge of elements heavier than iodine is at higher energies, and can therefore become accessible for diagnostic x-ray imaging. This means that such high-Z

elements may provide more contrast than iodine at the same concentration and can also be used for material decomposition purposes. In fact, the spectral information provided by PC detectors can be used to detect a K-edge (Schlomka et al. 2008) and to generate the material map of the corresponding element (K-edge imaging). In case such element is embedded in a nanoparticle for a contrast agent, it is possible to obtain the 3D distribution of the agent. If the energy resolution of the PC detector is sufficient, multiple K-edge elements can be simultaneously decomposed and multi contrast agent imaging can be achieved. This fascinating possibility is being investigated and examples can already be found in the literature. In a swine study, Ren et al. 2020 administered iodine via intravascular route and bismuth via enteric route. The two materials have been simultaneously decomposed to generate maps of the vasculature enhanced by the iodine and of the intestine lumen enhanced by the bismuth. In another example, Symons et al. 2017b tested on rabbits a multi contrast agent protocol for multi-phase liver imaging with a single CT acquisition. In the study, iodine and gadolinium-based agents were injected at different times so that the portal phase could be visualized in the iodine map (injected first) and the arterial phase could be visualized in the gadolinium map (injected 12 s after the iodine).

In this thesis, the development of new contrast agents in combination with the new PC technologies is addressed both at a preclinical and clinical level. In preclinical settings, a novel nanoparticle contrast agent based on bismuth is tested for the first time *in-vivo*. To perform the mice experiments, an experimental gantry equipped with a PC detector is designed and assembled. The new micro-CT is used to characterize the biodistribution of the bismuth-based agent in healthy mice and time-enhancement curves are measured for the main organs. Furthermore, a protocol for multi contrast agent imaging is herein designed and a proof of concept on mice is also provided. In clinical settings, the potential of several high-Z elements heavier than iodine is investigated specifically for contrast enhancement applications. The contrast provided by each element is compared to the gold standard iodine using simulations and phantom measurements at a whole-body PC-CT Siemens prototype. The potential radiation dose reductions associated with contrast improvements are quantified as well. Furthermore, for each high-Z element, a two material decomposition with soft tissue was performed and evaluated. Then, to investigate a wide range of scenarios for contrast-enhanced CT, a systematic investigation is carried out by varying tube voltage, spectrum prefiltration, patient size, and energy threshold settings. In the end, the results for a PC detector are compared to the results previously obtained for EI detectors.

2 | Fundamentals

This chapter provides an introduction to x-ray and how they are used for CT imaging. Furthermore, the novel photon-counting detectors are described and the usage of contrast agents in CT is discussed.

2.1 X-ray Computed Tomography

X-ray radiation has been discovered by W. C. Röntgen at the end of the 19th century (Röntgen 1898) and consists of photons with energy between 100 eV and several MeV. X-rays are extensively used for medical and industrial imaging thanks to their ability to traverse the matter and to be attenuated according to the matter's properties.

2.1.1 X-Ray Generation

In medical applications, x-rays are generated using an x-ray tube. In these devices, a high voltage (U , 10-150 kV) is applied between an incandescent cathode and a tungsten-alloy anode, both placed in a vacuum tube. The electrons emitted by the cathode are accelerated towards the anode by the tube voltage up to an energy of $e \cdot U$, where e is the elemental charge. Once the electrons impinge on the anode, they dissipate the $\sim 99\%$ of their energy as heat and the remaining 1% as bremsstrahlung radiation. Also, some characteristic fluorescent peaks are generated by the relaxation of the excited atoms of the anode, and they contribute to the x-ray spectrum generated by the tube. The fluorescent peaks are denoted according to the final shell of the transition (K for the innermost shell, L for the second, M , ...), the difference between the initial and the final shell ($\alpha = 1$, $\beta = 2$, ...) and the fine structure of the sub-shells (1, 2, ...). In Figure 2.1, a typical 120 kV x-ray spectrum used in the clinic is shown. It is possible to see how the maximum energy of the bremsstrahlung spectrum is given by the maximum energy of the accelerated electrons inside the tube. For the specific tungsten target, the characteristic fluorescent peaks are visible in correspondence of the transition to the innermost shell (K).

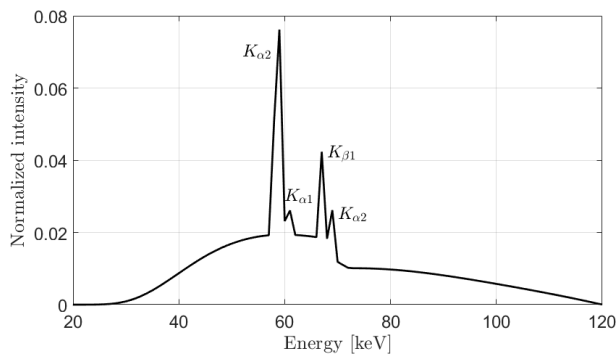


Figure 2.1: Example of a 120 kV x-ray spectrum used clinically. The spectrum modeled for a reflection tube and it is filtered according to the specification of the Siemens SOMATOM CounT (6.8 mm Al, 1.0 mm C, 0.7 mm Ti and 0.008 mm W). The fluorescent peaks of tungsten are visible and over imposed to the continuous bremsstrahlung emission.

X-ray tubes can be divided into transmission and reflection tubes, according to the anode geometry. In the transmission tube, the anode consists of a thin slab ($\sim 10 \mu\text{m}$) of tungsten: the electron beam impinges on one face of the anode, and the x-ray beam exits from the other face of the slab. In the reflection tube, the anode is a thick layer of tungsten on which the electron beam impinges at an angle ($\sim 7^\circ$) and the x-ray beam is collected at 90° from the electron beam direction. Reflection tubes can also be equipped with a liquid-cooled rotating anode, which provides better heat dissipation. This is a requirement for clinical and big industrial applications, where a high photon rate is needed. Transmission tubes are used instead in low-power applications, like preclinical imaging, where the imaging system can benefit from the smaller focal spot size.

2.1.2 X-Ray Interaction with Matter

When x-ray photons travel through matter, they are exponentially attenuated according to the Beer-Lambert law (Beer 1852, Lambert 1760). In the simple case of monochromatic radiation and homogeneous absorber, the Beer-Lambert law is:

$$N(L) = N_0 \cdot e^{-\mu \cdot L}, \quad (2.1)$$

where N_0 is the incoming number of photons, and $N(L)$ is the number of photons transmitted through an absorber thick L with attenuation coefficient μ . The attenuation coefficient μ is measured in inverse-length units and describes the attenuation properties of the material. In the diagnostic energy range (20 keV - 150 keV), the main photon-matter interactions that contribute to μ are the

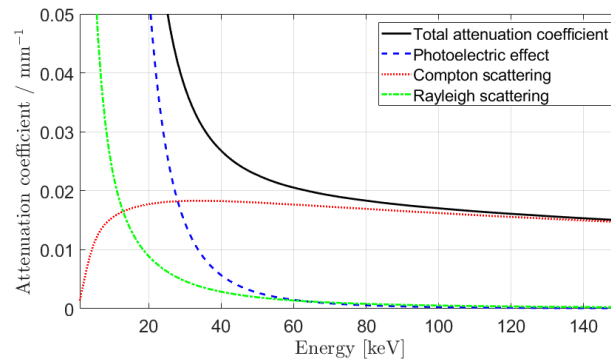


Figure 2.2: Attenuation coefficient of water with the individual contributions by the photoelectric effect, Compton scattering and Rayleigh scattering.

photoelectric effect, the Compton scattering, and the Rayleigh scattering, whereas pair production processes do not take place since they require photon energy higher than 1022 keV.

In detail:

- **Photoelectric effect:** absorption of a photon by an atom, with consequent emission of an inner-shell electron (K or L shell). This process is possible when the photon energy E is higher than the binding energy E_b of the electron. The emitted electron is removed from the shell with a kinetic energy $T = E - E_b$. The photoelectric attenuation coefficient μ_{PH} is:

$$\mu_{\text{PH}} \propto \rho \frac{Z^4}{A \cdot E^3}, \quad (2.2)$$

where E is the photon energy, and ρ , A , and Z are the material density, the atomic mass, and the atomic number of the material, respectively. Due to the strong dependency on the photon energy and on the material atomic number, the photoelectric effect is more relevant for heavier elements or at lower energies (Figure 2.2). A sharp increase in the attenuation coefficient can be seen if the binding energy of an electron is in the energy range of interest. This is the case of high- Z materials like iodine, gadolinium, bismuth, whose binding energy of the K-shell electrons is at 33.2 keV, 50.2 keV, and 90.5 keV, respectively. In these cases, the sharp increase of the attenuation coefficient is called K-edge (Figure 2.3).

- **Compton scattering:** inelastic scattering of a photon on an atomic electron of the outermost shells. The attenuation coefficient due to the Compton scattering μ_{CS} is:

$$\mu_{\text{CS}} \propto \rho \frac{Z}{A \cdot E^m}, \quad (2.3)$$

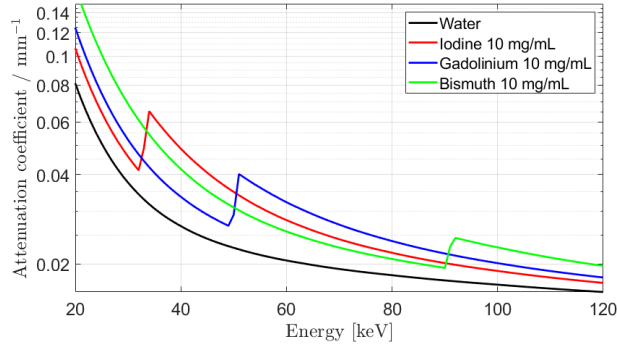


Figure 2.3: Attenuation coefficients of elements with the K-edge in the diagnostic energy interval. The K-edge of a 10 mg/mL water-solution of iodine is visible at 33.3 keV, the one of gadolinium at 50.2 keV and the one of bismuth at 90.5 keV. The attenuation coefficient of water is displayed as well for comparison.

with $0 \leq m \leq 1$ (Attix 1986, p. 140). Since the ratio Z/A is almost constant for stable elements, the Compton scattering is almost independent of the specific material. As it can be seen in Figure 2.2, the Compton scattering is the most relevant effect for water in the diagnostic energy range.

- **Rayleigh scattering:** elastic scattering of a photon on an atom. The photon does not lose energy and its direction is only slightly changed. The attenuation coefficient due to Rayleigh scattering is (Attix 1986, p. 153):

$$\mu_{\text{RS}} \propto \rho \frac{Z^2}{A \cdot E^2}. \quad (2.4)$$

In medical imaging, the contribution of the Rayleigh scattering to the overall attenuation is minimal (Figure 2.2). Furthermore, since the photon is elastically scattered, it does not deposit any dose in the patient.

Since the attenuation coefficient of matter is energy-dependent, Equation (2.1) can be rewritten to calculate the transmitted photons for a polychromatic spectrum $N_0(E)$:

$$N = \int_0^{E_{\text{max}}} dE N_0(E) e^{-\mu(E) \cdot l}, \quad (2.5)$$

where E_{max} is the maximum energy of the spectrum.

In realistic scenarios, the object being transverse by x-rays is not homogeneous and μ is a function of the position \mathbf{r} inside the object. By integrating along the path L of a ray, we obtain the Beer-Lambert law for polychromatic spectrum transmitted through a heterogeneous object:

$$N = \int_0^{E_{\text{max}}} dE N_0(E) e^{-\int_L \mu(\mathbf{r}, E) \cdot dl}. \quad (2.6)$$

In transmission imaging, the x-rays transverse the object to be imaged, get attenuated, and then are collected by a pixelated detector. The Beer-Lambert law in Equation (2.6) models the photons transmitted through the object, but not the photons detected by the detector. The detection process will be described in the following section.

2.1.3 X-Ray Detection

The aim of detectors is to absorb x-ray photons and convert them into a measurable electric signal. In order to quantify the fraction of photons that are detected, Equation (2.5) can be rearranged into:

$$\eta(E) = 1 - e^{-\mu_{\text{Det}}(E) \cdot d}, \quad (2.7)$$

where $\eta(E)$ is the detection efficiency of photons of energy E , $\mu_{\text{Det}}(E)$ is the attenuation coefficient of the detector and d is its thickness. This simple definition of the detection efficiency does not take into consideration the inter-pixel exchange of energy or the escape of fluorescent photons. These effects will be treated in detail in Section 2.2.1.

The detection of photons can be achieved using two different technologies: indirect and direct conversion.

Indirect conversion: this is the technology generally used in clinical CT scanners. It is defined *indirect* because the x-ray photons interact with a pixelated scintillator generating multiple visible photons which are then detected by photodiodes (Figure 2.4, left). An x-ray photon of 100 keV usually generates $10^3 - 10^4$ visible photons which are guided towards the photodiode thanks to the reflective layers covering the top and the sides of each pixel. For a $\text{Gd}_2\text{O}_2\text{S}$ scintillator coupled with a photodiode, the signal detected for each photon has a width of ~ 2500 ns. This duration is long compared to the incoming photon rate, therefore the signal generated by photons within the readout time is integrated (Knoll 2000, p. 816). Since the number of optical photons generated in the scintillation process is proportional to the energy of the incoming photon, these detectors are also called energy-integrating (EI) detectors. The intensity measured at the photodiode can therefore be evaluated as:

$$I = \int_0^{E_{\text{max}}} E \cdot \eta(E) N_0(E) e^{-\int_L \mu(r,E) \cdot dl} dE, \quad (2.8)$$

where the Beer-Lambert law is combined with the detection efficiency and the factor E due to the scintillation process.

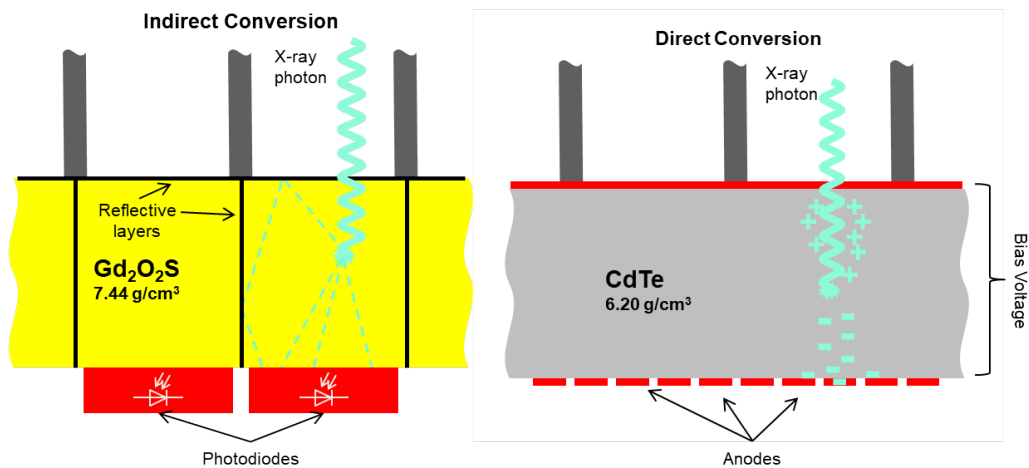


Figure 2.4: Schematics of an energy-integrating detector (left) and of a photon-counting detector. For the energy-integrating detector, the x-ray photons interacting with the pixelated scintillator are converted into multiple visible photons which are then detected by the photodiodes. For the photon-counting detector, the x-ray photons interacting with the semiconductor are converted into electron-hole pairs. The cathode and the anode (pixelated) collect the electron-hole pairs thanks to the applied bias voltage. On the surface of both detectors, an antiscatter grid is present.

Direct conversion: this technology is based on a semiconductor layer on which a bias voltage (500 V - 1000 V) is applied through electrodes. Only the anode is pixelated, whereas the cathode and the semiconductor layer are solid (Figure 2.4, right). Since there is no need of a reflective layer in the semiconductor, the pixels can be manufactured with a smaller size compared to EI detectors. When an x-ray photon interacts with the semiconductor, electron-hole pairs are generated and then collected by the electrodes. Thus, a current proportional to the photon energy can be measured. The pulse generated by each photon (~ 25 ns for CdTe) is much shorter than the one generated for an indirect-conversion detector, therefore single photon-counting (PC) is possible with direct-conversion detectors. Each pixel of the PC detectors is equipped with multiple energy thresholds (2 to 4 thresholds) which can be used to sort the detected signal according to its energy. Therefore each individual photon can be classified into different energy bins. For PC detectors, the signal detected in the energy bin b , defined by a lower energy E_b and an upper energy E_{b+1} , is:

$$I_b = \int_{E_b}^{E_{b+1}} \eta(E) N_0(E) e^{-\int_L \mu(r,E) \cdot dl} dE. \quad (2.9)$$

As it will be explained in Section 2.2.1, some further effects must be taken into account in order to model a realistic response of a direct conversion detector.

CT prototypes equipped with PC detectors are being investigated for CT applications (Z. Yu et al. 2016a, Kappler et al. 2014), and recently (November 2021) the first whole-body PC-CT scanner has been released on the market (NAEOTOM Alpha by Siemens Healthineers, Forchheim, Germany). Direct-conversion PC detectors and their potentials in clinical CT will be treated in detail in Section 2.2.

2.1.4 CT System

X-ray computed tomography (CT) is a transmission imaging-modality developed by Sir Godfrey N. Hounsfield (Hounsfield 1972, Hounsfield 1973). Since its introduction for clinical applications, CT became an indispensable tool for visualization of the inside of the human body, and nowadays is the imaging modality mostly used in radiology departments (Buzug 2008, p.1). A clinical CT system is composed of an x-ray source and a detector mounted on the opposite sides of a rotating gantry. The gantry is hollow at the center in order to accommodate the sample to be imaged (Figure 2.5). In industrial applications instead, the source and the detector are stationary, whereas the sample is placed on a rotating platform.

In CT, the detector measures the intensity I of the x-ray attenuated by the sample (Equation (2.8), (2.9)), which is normalized by a flat field acquisition I_0 (acquisition without the sample), and then used to calculate the projection value $p = -\ln(I/I_0)$. The monochromatic version of the Beer-Lambert law (Equation (2.1)) can be used to express the projection value as the line integral of the attenuation coefficient of the object:

$$p = -\ln \frac{I}{I_0} = \int_L \mu(\mathbf{r}, E_0) \cdot dl, \quad (2.10)$$

where E_0 is a defined energy. By rotating the gantry around its axis (\mathbf{z}), it is possible to acquire all the line integral on a 2D plane through the object ($\mathbf{x} - \mathbf{y}$ plane). For a parallel-beam geometry, a rotation of 180° is sufficient, whereas for a fan-beam geometry the rotation should be of 180° plus the fan angle. With a complete set of line integrals it is possible to reconstruct the 2D distribution of the attenuation coefficient $\mu(\mathbf{r}, E_0)$ using a filtered backprojection algorithm (Radon 1971, Ramachandran et al. 1971).

Since the human body is mostly composed of water-equivalent materials, it is very practical in clinical CT to express the reconstructed attenuation coefficients μ relative to the attenuation coefficient of water $\mu_{\text{H}_2\text{O}}$. This relative number is called CT-value and is calculated as:

$$CT = \frac{\mu - \mu_{\text{H}_2\text{O}}}{\mu_{\text{H}_2\text{O}}} \cdot 1000 \text{ HU}, \quad (2.11)$$

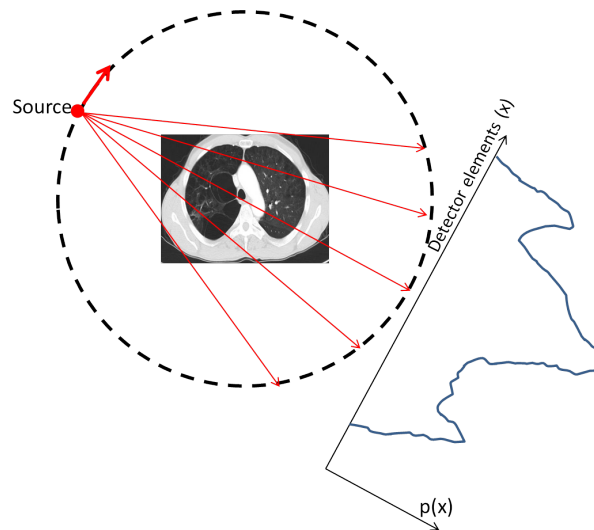


Figure 2.5: Schematic of a CT scanner. The x-ray emitting source moves on a circular pattern around the sample to be imaged. On the opposite side, the detector measures the transmitted spectrum for each angle and the projection values $p(x)$ can be calculated.

where HU is the Hounsfield unit. By applying this conversion, water will have a CT-value of 0 HU, air (considered vacuum) -1000 HU, and bone ~ 500 HU and higher.

2.2 Photon-Counting CT

Photon-counting (PC) detectors (introduced in Section 2.1.3) have a huge potential for clinical CT applications (Taguchi et al. 2013, Willemink et al. 2018, Lell et al. 2020). The PC detectors are based on the direct detection of photons in a semiconductor layer (usually CdTe). The fast front-end electronics associated with each pixel allow for single photon-counting and therefore an equal weight is assigned to each detected photon. Conversely, the energy-integrating (EI) detectors assign a weight that is proportional to the photon energy, and the signals of all photons detected within one frame are integrated. In recent years, PC-CT has been thoroughly investigated and compared to the state-of-art EI-CT. Advantages of PC-CT over conventional EI-CT have been already shown regarding image noise (Klein et al. 2020), spatial resolution (Mannil et al. 2018) and iodine contrast enhancement (Sawall et al. 2020b). Furthermore, each pixel of a PC-detectors can be equipped with multiple and adjustable energy thresholds. This feature allows classifying the detected photons in different energy bins according to the photon energy, thus providing spectral information. Spectral imaging is

possible also with EI-detectors, but different acquisition techniques have to be used, like dual-source, kV-switching, or sandwich detector (Faby et al. 2015). The spectral information may be used to differentiate the different materials of the imaged sample. This process is called material decomposition and it is especially of interest in clinical CT.

In this section, the response of PC-detectors will be analyzed in more detail and the material decomposition process will be described.

2.2.1 Spectral Response and Bin Sensitivity

The spectral response of a detector $R(E', E)$ is the ratio between the amount of photons $N(E', E)$ detected at energy E' when $N(E)$ photons at energy E impinge on the detector:

$$R(E', E) = \frac{N(E', E)}{N(E)} \quad . \quad (2.12)$$

For an ideal detector, the spectral response is a Dirac delta function $\delta(E - E')$, and corresponds to a complete photoelectric absorption of the incoming photon (Figure 2.6). In realistic scenarios, several physical effects must be taken into account, like noise, charge sharing, fluorescent peaks, K-escape peaks, and Compton scattering (Ballabriga et al. 2016). A realistic spectral response can be estimated using Monte Carlo simulations (Nilsson et al. 2002), parametric models calibrated on measurements (Roessl et al. 2007) or increment matrix approaches (Faby et al. 2016). A spectral response at 100 kV calculated using the latter method is shown in Figure 2.6 for a CdTe detector with a pixel size of 225 μm . It is possible to see the photopeak at 100 keV, the K_α -fluorescence peak of cadmium at 25.4 keV, the K-escape peak at 74.6 keV and the noise peak around 0 keV. The background is due to the Compton scattering and to the charge sharing. It is important to notice that the sum of the spectral response over the different energies can be higher than 1 since a single photon can be counted multiple times if its signal is shared between multiple pixels. The pixel size plays an important role in the spectral response: with smaller pixels, it is more likely that K-fluorescent photons escape the origin pixel or that the charge cloud generated in the semiconductor is shared between adjacent pixels. This phenomenon will be observed in Sections 3.3.3 and 3.1.1, where the spectral response is calculated for PC-detectors with different pixel sizes.

A more practical quantity to be used in realistic scenario is the bin sensitivity $s_b(E)$, which is defined as the fraction of photons of energy E detected in the b -th energy bin. The spectral responses can be used to calculate the bin sensitivity according to the chosen energy thresholds:

$$s_b(E) = \int_{E_b}^{E_{b+1}} R(E', E) dE' \quad , \quad (2.13)$$

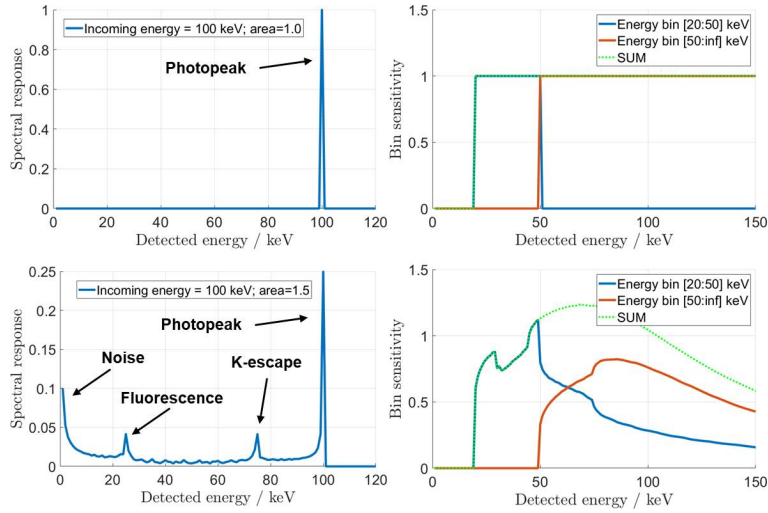


Figure 2.6: Left column: examples of the spectral response of an ideal (top) and realistic (bottom) PC detector. The spectral responses are evaluated for incoming photons at 100 keV. Right column: examples of the bin sensitivity on an ideal (top) and realistic (bottom) PC detector with two energy thresholds set at 20 keV and 50 keV. In the realistic scenario, the photons with energy higher than 50 keV contribute to the low energy bin as well. The total sensitivity is displayed as well.

where E_{b+1} and E_b are the upper and lower threshold of the b -th energy bin, respectively. An example of bin sensitivity is given in Figure 2.6 for $T_0 = 20$ keV and $T_1 = 50$ keV. The photons with energy higher than 50 keV contribute not only to the high-energy bin but also to the lower one because of the effects previously mentioned (e.g. charge sharing). The detection efficiency of the detector (Equation (2.7)) is included in the spectral response and therefore in the bin sensitivity. This can be noticed since the sum of the two bin sensitivities decreases at energies higher than ~ 70 keV. As for the spectral response, the bin sensitivity exceeds 1 at certain energies because of multiple counts due to the charge sharing. The bin sensitivity is very useful since it can be multiplied to the spectrum in the air to calculate the detected spectrum for each energy bin.

2.2.2 Material Decomposition

As described in Section 2.1.2, the attenuation coefficient of matter $\mu(E)$ in the diagnostic energy range is mainly a combination of photoelectric effect and Compton scattering. This means that the distribution of $\mu(\mathbf{r}, E)$ within a sample can be expressed as linear combination of $\mu_{\text{PH}}(E)$ and $\mu_{\text{CS}}(E)$ (Alvarez et al. 1976,

Roessl et al. 2007):

$$\mu(\mathbf{r}, E) = a_{\text{PH}}(\mathbf{r})\mu_{\text{PH}}(E) + a_{\text{CS}}(\mathbf{r})\mu_{\text{CS}}(E), \quad (2.14)$$

where $a_{\text{PH}}(\mathbf{r})$ and $a_{\text{CS}}(\mathbf{r})$ are the weights describing the spatial distribution of the two basis functions $\mu_{\text{PH}}(E)$ and $\mu_{\text{CS}}(E)$. Other basis function can be chosen under the condition that they are linearly independent. In clinical scenario, a more practical and common choice is to use the attenuation coefficients of water $\mu_{\text{H}_2\text{O}}(E)$ and calcium $\mu_{\text{Ca}}(E)$. In good approximation, all the biological materials can be described as a linear combination of these two basis functions (Willemink et al. 2018).

Equation (2.14) holds true if no K-edges are present in the used energy range. In clinical practice, it is common to deploy contrast agents based on iodine (Section 2.3), which has a K-edge at 33.3 keV. In this case, the attenuation coefficient of iodine $\mu_{\text{I}}(E)$ must be included as a basis function to properly describe the attenuation coefficient of the specimen:

$$\mu(\mathbf{r}, E) = a_{\text{H}_2\text{O}}(\mathbf{r})\mu_{\text{H}_2\text{O}}(E) + a_{\text{Ca}}(\mathbf{r})\mu_{\text{Ca}}(E) + a_{\text{I}}(\mathbf{r})\mu_{\text{I}}(E), \quad (2.15)$$

where $a_{\text{I}}(\mathbf{r})$ describes the spatial distribution of the iodine. The previous equation can be extended to an arbitrary number of basis function M with the condition that all the basis function must be linearly independent:

$$\mu(\mathbf{r}, E) = \sum_{m=0}^M a_m(\mathbf{r})\mu_m(E). \quad (2.16)$$

As for the iodine, materials with a K-edge in the used energy range are always independent of any other material.

The material decomposition process consists in solving Equation (2.16) in order to obtain $a_m(\mathbf{r})$, which is the spatial distribution of the m -th material, usually called material map. For this purpose, it is fundamental to sample the attenuation coefficient of matter at different energies E_b , so that a system of equations can be written and inverted. For a PC detector, the sampling energies E_b are the energy bins defined by the different energy thresholds, whereas for a dual source EI-CT, two sampling energies are obtained by using two different spectra. The number of energy samples must be equal to or higher than the number of basis materials, otherwise, the system is under-determined. Exceptions can be made if extra constraints are introduced in the system, like mass conservation (Liu et al. 2009) or volume conservation (L. Yu et al. 2009).

The material decomposition can be performed in projection domain or in image domain. In projection domain, the material decomposition takes place before the image reconstruction. A maximum-likelihood algorithm (Schlomka et al. 2008) is

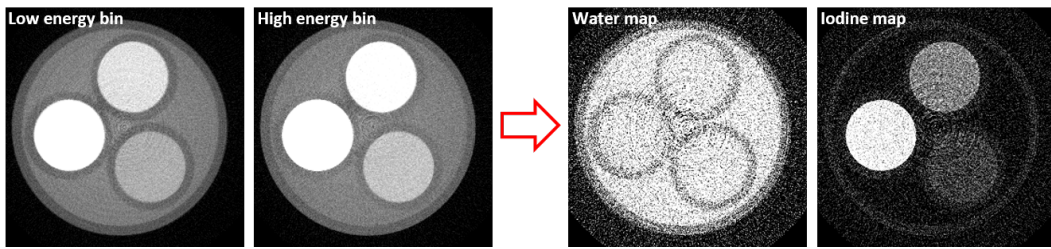


Figure 2.7: Example of material decomposition. Left: bin images of a water phantom filled with iodine inserts. Right: material maps of water and iodine.

used to estimate the integral form of $a_m(\mathbf{r})$:

$$A_m = \int_L a_m(\mathbf{r}) \cdot dl, \quad (2.17)$$

where L is the ray path (as in Equation (2.6)). Then, the material map of the m -material is reconstructed using the same algorithms used for CT-image reconstruction. In image domain, the material decomposition takes place after the image reconstruction and it consists of the inversion of the system (2.16). In order to write the system, the basis materials $\mu_m(E_b)$ should be known for all the energy bin b . This can be easily achieved by performing a calibration measurement of known samples containing the basis materials. An example of material decomposition is shown in Figure 2.7: a mouse-sized water phantom with three inserts with different iodine concentrations was imaged with a PC detector and two energy thresholds. The high and low energy bin images were used to perform an imaged-based material decomposition into water and iodine. As it is possible to notice, by performing a material decomposition the image noise increases.

2.3 Contrast Agents in CT

Contrast agents play an essential role in diagnostic imaging since they allow (e.g.) imaging of the cardiovascular system, the detection of perforations of organs, and dysfunction of the esophageal sphincter. More than 85 million CT scans are performed in the USA every year, and approximately half of them are performed with the injection of intravenous contrast agents (Yeh et al. 2017).

The only contrast agents approved in CT imaging are based on iodine ($Z = 53$) for intravenous injection, and on barium for oral ingestion ($Z = 56$). Such agents have been thoroughly investigated during the past century in order to increase their biocompatibility and their efficiency. Despite the continuous development,

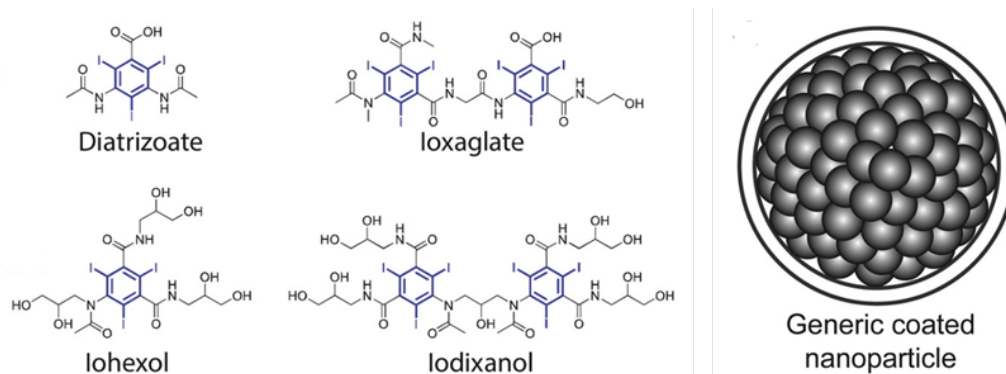


Figure 2.8: Right: four molecules of iodinated contrast agent commercially available. All the molecules are based on tri-iodinated benzene rings. Right: example of a generic coated nanoparticle filled with atoms of a high-Z element. Adapted from Yeh et al. 2017

the fundamental structure of the molecules containing the high-Z element (tri-iodinated benzene rings and barium sulfate) remained almost unchanged (Lusic et al. 2013). Four examples of contrast agent molecules based on the tri-iodinated benzene ring are displayed in Figure 2.8 left.

2.3.1 High-Z Elements

Iodine and barium have a K-edge at 33.2 keV and 37.1 keV, respectively. Such energies are low compared to the spectra usually used in clinical CT. If an average patient is modeled as a water cylinder with a diameter of 32 cm, it is possible to see how the 90 % of the transmitted photons of a 100 kV spectrum are above 50 keV (Figure 2.9). This means that from a strictly physical point of view, iodine and barium may be not the best choice when considering x-ray attenuation properties. Poor attenuation may also be provided by elements with K-edges at too high energy compared to the transmitted spectrum. This can be seen in Figure 2.9, where also the attenuation coefficient of bismuth is shown.

The interest in developing new contrast agents arose since the introduction of dual-energy CT, and further increased with the introduction of PC detectors. With these technologies, it is possible to sample the attenuation coefficient of matter at different energies and therefore perform material decomposition. As explained in Section 2.2.2, if an element has a K-edge in the range of used energy, it can be exploited as an additional basis function for the material decomposition. This is extremely fascinating because it means that if a contrast agent is based on such an element, a material map of the agent can be calculated. High-Z elements are being investigated for CT applications concerning both their attenuation (Nowak

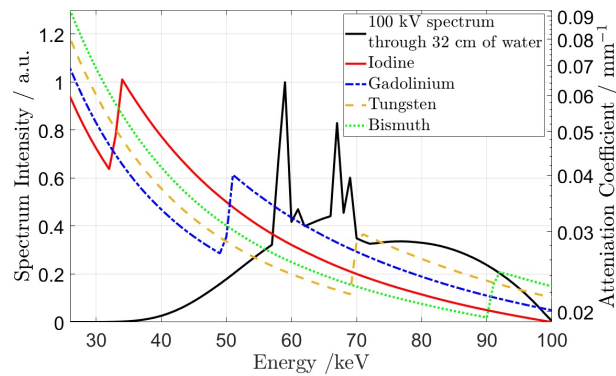


Figure 2.9: Example of a 100 kV simulated spectrum transmitted through 32 cm of water. The attenuation coefficients of iodine, gadolinium, tungsten and bismuth are displayed as well. The K-edges are visible at 33.2 keV (I), 50.2 keV (Gd), 69.5 keV (W) and 90.5 keV (Bi). No photons are transmitted below the iodine K-edge energy.

et al. 2011, Roessler et al. 2016) and material decomposition properties (Rabin et al. 2006, Popovtzer et al. 2008, Aydogan et al. 2010, Moghiseh et al. 2018). Furthermore, since PC detector can have more than two energy thresholds, more than two materials can be decomposed simultaneously. If more than one K-edge is present, the corresponding materials can also be decomposed simultaneously. This approach is defined multi contrast agent imaging (Symons et al. 2017a, Badea et al. 2019).

In figure 2.10, some basic characteristics of the candidate high-Z elements are listed.

Atomic number (Z)	Name	Symbol	K edge (keV)	Annual production (metric tons)	Raw cost of material per 30 g dose (USD)	Concerns*
53	Iodine	I	33.2	>30,000	<1	I >100 kVp
54	Xenon	Xe	34.6	<1		G
55	Cesium	Cs	36.0	<20	>600	T
56	Barium	Ba	37.4	6,000,000	<1	BaSO ₄ T for IV
57	Lanthanum	La	38.9	12,000	<1	La ₂ O ₃
58	Cerium	Ce	40.4	23,000	<1	CeO ₂
59	Praseodymium	Pr	42.0	2500	<1	Pr ₆ O ₁₁
60	Neodymium	Nd	43.5	7000	<3	Nd ₂ O ₃
61	Promethium	Pm	45.2			Synthetic
62	Samarium	Sm	46.8	700	<1	Sm ₂ O ₃ A
63	Europium	Eu	48.5	100	<30	Eu ₂ O ₃ C, A
64	Gadolinium	Gd	50.2	400	<1	Gd ₂ O ₃ T, A
65	Terbium	Tb	52.0	10	<30	Tb ₄ O ₇ C, A
66	Dysprosium	Dy	53.8	100	<20	Dy ₂ O ₃ C, A
67	Holmium	Ho	55.6	10	<1	Ho ₂ O ₃ A
68	Erbium	Er	57.5	500	<1	Er ₂ O ₃ A
69	Thulium	Tm	59.4	50	<1	Tm ₂ O ₃ A
70	Ytterbium	Yb	61.3	50	<1	Yb ₂ O ₃ T, A
71	Lutetium	Lu	63.3	10	<50	Lu ₂ O ₃ C, A
72	Hafnium	Hf	65.3	50	<20	HfO ₂ C, A
73	Tantalum	Ta	67.4	>1200	<1	Ta ₂ O ₅ I <90 kVp
74	Tungsten	W	69.5			T
75	Rhenium	Re	71.7	49	>100	C, A
76	Osmium	Os	73.9	<1		C, A
77	Iridium	Ir	76.1	3	>500	C, A
78	Platinum	Pt	78.4	160	>1000	C, A
79	Gold	Au	80.7	2800	>1000	C, I
80	Mercury	Hg	83.1			High T
81	Thallium	Tl	83.5			High T
82	Lead	Pb	88.0			High T
83	Bismuth	Bi	90.5	8500	<1	I
84	Polonium	Po	93.1			High R

*G – gas; no stable solid compounds at room temperature.

T – toxicity.

C – cost.

A – availability.

I – imaging performance.

R – radioactivity (toxic).

Figure 2.10: Candidate high-Z elements for CT contrast agents. Light green (iodine): only element allowed as CT contrast agent. Medium green (tantalum): currently under investigation as a general purpose CT contrast agent. Dark green: under investigation but with some limitations. Orange: limited world production. Red: low potential due to toxicity, radioactivity, or gaseous phase. Adapted from Yeh et al. 2017.

2.3.2 Nanoparticle-based Contrast Agents

The contrast agents based on iodine and barium have been proved to be clinically safe and highly tolerable by patients. The development of contrast agents based on heavier elements is not trivial since such elements can be toxic or difficult to include in biocompatible molecules. To address the biocompatibility challenge, a successful approach is to use nanoparticles to densely pack a specific element and then apply a biocompatible coating to the nanoparticle (Figure 2.8, right). Some example of contrast agents based on high-Z nanoparticles have been already investigated for preclinical use (Badea et al. 2019, El Ketara et al. 2020). Nanoparticles are especially interesting for cardiovascular imaging since they usually have a large diameter (up to hundreds of nanometers) and consequently they do not undergo fast renal clearance. Therefore nanoparticles have long circulating time, acting as blood-pool agents, and they are cleared via the liver. It is interesting to notice that thanks to their size, nanoparticles preferentially accumulate in solid tumors. This is due to extravasation in the tumor through a leaky endothelium, which can have pores with a size up to 800 nm (Karathanasis et al. 2009). Furthermore, the particle coating can be engineered to obtain targeted contrast agents which may be used for molecular imaging (Li et al. 2014, Sawall et al. 2021) or theranostic applications (Bejarano et al. 2018).

3 | Materials and Methods

3.1 Assembling a New Experimental Micro-CT

In order to develop the new photon-counting technologies and new high-Z contrast agents, it is fundamental to have a versatile platform for experimentation. Since mice are the best model for *in-vivo* experimentation of new drugs (e.g. experimental contrast agents), this platform should be a micro-computed tomography (micro-CT): a scanner with spatial resolution and field of view suitable for small-animal imaging. Siemens has already developed a whole-body PC-CT prototype, the SOMATOM CounT (described in the following in Section 3.3.2) which is a powerful tool for clinical investigation, but since it is designed for human imaging, it does not have a sufficient spatial resolution for small-animal imaging (Sawall et al. 2020c). Therefore, assembling a new micro-CT system with a PC detector was one of the main goals of my work. In the following, the main components and the geometry of the gantry will be presented. At the end of the section, the data processing chain developed for the system will be described.

3.1.1 Novel Photon-Counting Detector by Dectris

The PC detector which was mounted in the new experimental gantry is the Sántis 3204 ME by Dectris ltd. (Baden-Dättwil, Switzerland). The detector (visible in Figure 3.1) was specifically developed for the Eurostars collaboration between the DKFZ, Dectris ltd., and NanoPET Pharma GmbH (Berlin, Germany) and was modeled specifically for micro-CT applications, therefore with a small pixel size of 150 μm . The detector is based on a direct conversion technology and consists of a 1 mm thick layer of Cadmium Tellurite (CdTe) to which a bias voltage of 500 kV is applied. The sensor has a total size of 308.4 mm \times 38.55 mm and it is divided into a 16 \times 2 matrix of smaller modules. At the edge between adjacent modules, a gap is present. These intermodule gaps have a size between 1 and 7 pixels and need to be inpainted before the image reconstruction (Section 3.1.4). The detector is also equipped with four energy thresholds which can be individually enabled, allowing the acquisition of multiple energy-bin images. In Table 3.1, all



Figure 3.1: Picture of the Dectris Säntis PC detector. The sensitive area measures 308.4 mm × 38.55 mm and the pixel size is 150 μm.

Table 3.1: Technical specifications of the Dectris Säntis PC detector.

Parameter	Value
Sensor material	Cadmium Tellurite (CdTe)
Sensor thickness	1000 μm
Sensor area	308.4 mm × 38.55 mm
Bias voltage	500 V
Pixel size	150 μm
Maximum count rate	1×10^8 photons/s/mm ²
Energy range	20 keV - 140 keV
Energy thresholds number	4
Energy threshold value	20 keV - 140 keV
Maximum frame rate	200 Hz
Weight	10 kg
Connection	10 Gigabit Ethernet

the technical specifications of the detector are listed.

Further than the power supply and Ethernet connection, the detector needs also water cooling and a dry air supply. The implementation of these requirements in the rotating gantry will be described in the following section.

The semirealistic detector model described in Faby et al. 2016 was used to calculate the spectral response of the detector, which is displayed in Figure 3.2. A comparison with the spectral response of the Siemens SOMATOM CountT (Figure 3.17) shows how the smaller pixel size of the Säntis detector affects the spectral response by decreasing the relative height of the photopeak and by increasing the charge sharing tail.

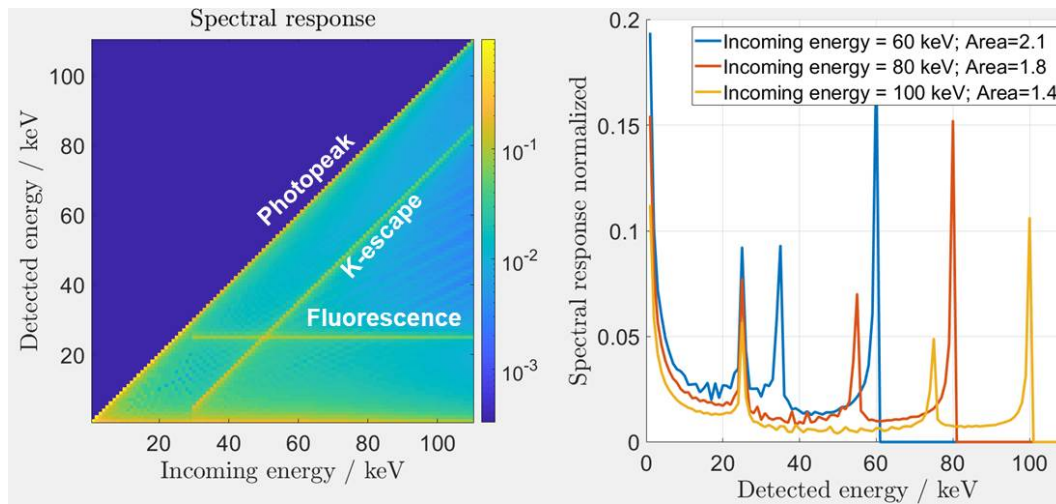


Figure 3.2: Spectral response of the Dectris Säntis detector. Left: 2D plot of the spectral response between 0 keV and 110 keV for incoming photons with energy up to 110 keV. Right: spectral response for an incoming photon energy of 60 keV, 80 keV and 100 keV.

3.1.2 Gantry Geometry

As it will be explained in the next section, a micro-CT scanner already present at DKFZ was modified for this purpose. Since the new Säntis detector had to be installed in the gantry, a new gantry geometry had to be modeled. In order to avoid substantial modification to the gantry structure, I decided to not modify the source-isocenter distance (R_F) and to model the new geometry as a function of the detector-isocenter distance (R_D). In order to obtain a scanner suitable for small animal imaging, three requirements had to be satisfied: a field of view (FOV) of at least 4 cm in diameter to accommodate both a mouse and the mouse table, a spatial resolution lower than 100 μm and a z -coverage appropriate to mouse cardiac imaging.

The spatial resolution can be modelled as:

$$resolution = \sqrt{\left(W_F \frac{R_D}{R_D + R_F}\right)^2 + \left(W_D \frac{R_F}{R_D + R_F}\right)^2}, \quad (3.1)$$

where W_F is the focal spot width and W_D is the detector pixel width. The radius of the FOV (R_M) (Figure 3.3) can be calculated as:

$$R_M = R_F \cdot \sin\left(\arctan\left(\frac{N_u/2 \cdot W_D}{R_D + R_F}\right)\right), \quad (3.2)$$

where N_u is the number of pixels in a detector row.

As it is shown in (Figure 3.3), the z -coverage can be measured at the isocenter

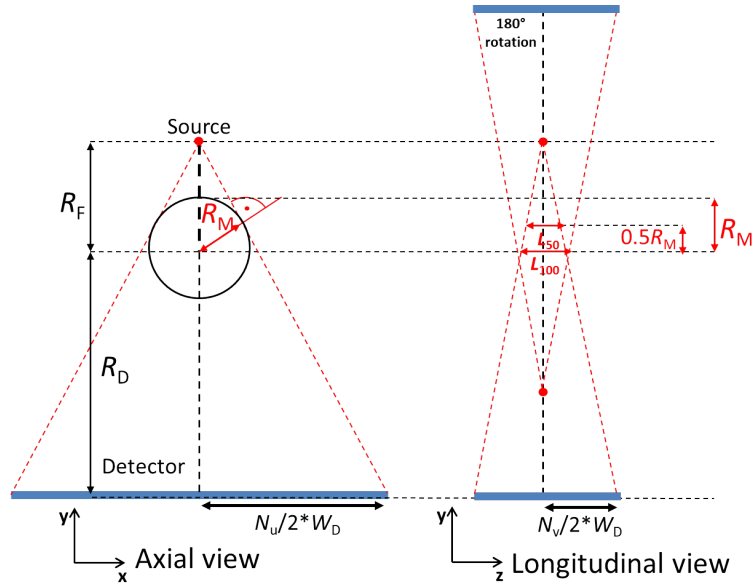


Figure 3.3: Schematic of the experimental gantry geometry. Left: axial view. Right: longitudinal view. R_F : source-isocenter distance. R_D : isocenter-detector distance. W_D : pixel size. N_u and N_v : detector elements in the longitudinal and axial direction. R_M : radius of the field of view. L_{100} and L_{50} : z -coverage.

(L_{100}) and at a radial distance of $R_M/2$ from the isocenter (L_{50}). These quantities can be modelled as:

$$L_{100} = 2 \cdot R_F \cdot \left(\frac{N_v/2 * W_D}{R_D + R_F} \right), \quad (3.3)$$

and

$$L_{50} = 2 \cdot (R_F - R_M/2) \cdot \left(\frac{N_v/2 * W_D}{R_D + R_F} \right), \quad (3.4)$$

where N_v is the number of detector rows.

The plots of these four quantities as a function of the R_D are shown in Figure 3.4. The spatial resolution (Equation (3.1)) was plotted both for the smallest and the largest focal spot size available with the deployed x-ray tube. More detail about the x-ray tube will be given in Section 3.1.3. As shown in the plots, by increasing the detector-isocenter distance and therefore the magnification, the resolution improves but the FOV and the z -coverage sizes decrease. Since the Sántis detector is 8 times wider than tall, it is not possible to exploit all the potential magnification without sacrificing the z -coverage.

The typical size of a mouse heart in the z -direction is ~ 8 -10 mm, therefore the

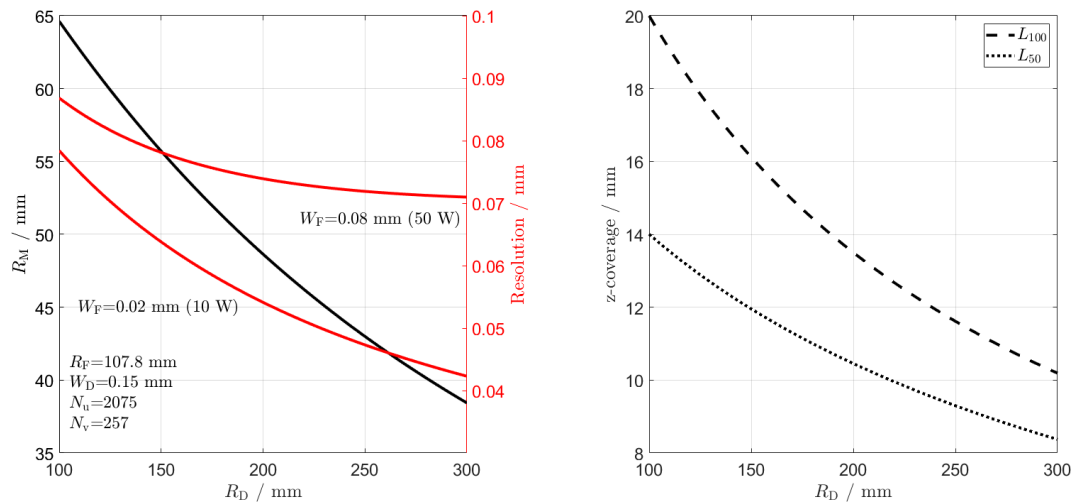


Figure 3.4: Left: plot of the spatial resolution and field of view as function of the isocenter-detector distance (R_D). The spatial resolution is evaluated for the smallest and the largest focal spot size (W_F). Right: plots of the z -coverage at the FOV center (L_{100}) and at a distance of $R_M/2$ (L_{50}) as a function of the isocenter-detector distance (R_D).

final R_D should be smaller than 210 mm. In order to account for mispositioning of the sample or anatomical changes, a slightly higher value can be chosen. For $R_D=200$ mm, the FOV is ~ 95 mm and the expected spatial resolution is below $80 \mu\text{m}$ for all the focal spot sizes. These values fulfill all the requirements mentioned at the beginning of the section, therefore the new geometry was modeled with $R_D=200$ mm.

3.1.3 CT-system and Hardware

The starting point of the new gantry assembling was a Siemens Sensation CT scanner, a gantry that was originally designed for clinical use. One Sensation scanner was available at DKFZ since 2014 and was refurbished in the last years for micro-CT applications (Sawall et al. 2017). The need to accommodate the new Santis detector led to a complete change of the gantry geometry. As a result, all the internal components already present in the gantry had to be dismantled and, whenever possible, modified and reused. In Figure 3.5, it is possible to see the empty gantry before the assembling started.

In the following, I am going to list the different components that I installed in the gantry and the modifications required.

- **X-ray source:** An x-ray tube suitable for mouse imaging was already mounted in the previous implementation of the micro-CT scanner. The tube



Figure 3.5: Picture of the experimental gantry before the assembling of the new components.

is a Hamamatsu L10951 Microfocus, a transmission tube that can operate up to 110 kV and has a maximum power of 50 W. Such a low power ensures a small focal spot size, which can range from 20 μm at 10 W up to 80 μm at 50 W. The existing tube mounting plates set the distance of the focal spot from the isocenter to 107.8 mm. Only minor modifications were needed in order to adjust the z -position of the tube.

- **Detector:** In order to mount the Sántis detector (Section 3.1.1) in the gantry, a new mounting plate had to be designed from scratch. By using the schematics of the detector and of the gantry, a plate was designed to ensure a detector-isocenter distance of 200 mm. The plate was manufactured from a 20 mm thick aluminum plate and fixed to the gantry with M10 bolts. In order to control the detector and retrieve the acquired data, a 10 Gigabit Ethernet connection is required between the stationary detector control unit and the rotating detector. Since this kind of fast connection cannot be handled by the gantry slip-rings, a rotary joint and two media converters were used for the purpose. One media converter is placed in the gantry and converts the detector Ethernet connection into two fiber optics. Then, the fiber optics enter the fiber optic rotary joint, a device (BN 549758C2000, by Spinner GmbH, Munich) capable of transferring the signal of up to 20

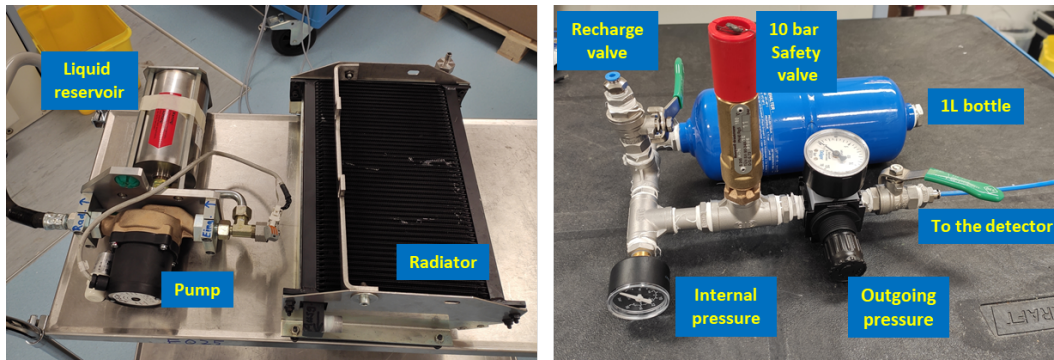


Figure 3.6: Left: water cooling system refurbished from an old x-ray tube. Right: 1 L dry air bottle with gauges for measuring the internal and outgoing pressure.

fibers from the rotating to the stationary part of the gantry. The fiber optic signal is converted again to Ethernet thanks to the second media converter and finally connected to the detector control unit. Despite the fiber optic rotary joint being already present in the previous version of the micro-CT scanner, new media converters had to be purchased and installed to fulfill the detector connection requirements.

- **Water cooling system:** As described in Section 3.1.1, the detector needs constant water cooling, also when the gantry is rotating. An old cooling system was refurbished for the purpose (Figure 3.6). The cooling system was originally used to cool the x-ray tube of the Sensation scanner when it was used for clinical applications. The old oil that was used to cool the tube was replaced with a 1:2 mixture of water and ethylen-glycol. Then, the cooling system was installed in the gantry and connected to the detector using new hoses.
- **Dry air supply:** In order to supply dry air to the detector while rotating, a small bottle (1 L) for pressurized air was installed in the gantry. The bottle can stand a maximum pressure of 10 bar and continuously provide dry air to the detector for about 40 minutes. The bottle (Figure 3.6) was equipped with valves for recharging and manometers to read the internal pressure and to adjust the airflow to the detector.
- **Angular position reader:** The angular position of the gantry can be measured thanks to a perforated ring placed in the internal circumference of the gantry. On the ring, two sets of holes distributed over 360° are available. The first consists of 1160 equally-spaced holes and it is used to read the relative increment of the angular position. The second set consists of one

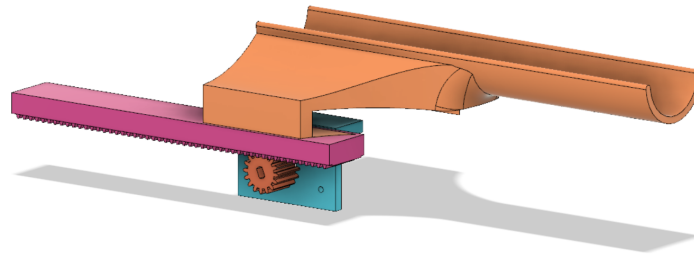


Figure 3.7: 3D rendering the mouse table equipped with a rack and a gear. A stepper motor connected to the gear can be remotely controlled to adjust the z -position of the sample.

single hole which provides an absolute reference. To read the passage of the two sets of holes, an Arduino with a multi-photodiode module was already installed in the gantry. The device had to be modified to include also a trigger mechanism that can start the acquisition whenever the detector is armed and the single hole per rotation is detected. The trigger signal is sent to the detector via a Lemo00 coaxial cable.

- **Mouse table:** A new sample/mouse holder had to be designed from scratch. An aluminum extrusion was mounted horizontally on the front side of the gantry and used to hold a plexiglass plate. Such plate which extends in the z -direction, is used as a rail for a sliding mouse table (Figure 3.7). The table can be moved along the z -direction thanks to a rack and a gear connected to a stepper motor. The motor is connected to an Arduino, which can be controlled remotely. I personally 3D-modelled all the components and programmed the Arduino. The sliding table allows for fast, precise and reproducible positioning of the sample, which is critical since the z -coverage of the system is only ~ 10 - 12 mm. The ability to control the table without entering the room also allowed to considerably decrease the acquisition time of sequence scans, where the mouse is scanned at different z -positions.

After having all the components installed in the gantry, a balancing procedure had to be carried out in order to compensate for the uneven distribution of weight. A balancing machine (Caroba Balancer, PMB GmbH, Kaiserslautern) was used to detect the unbalanced weight, which was then compensated by adding the proper amount of lead slabs where needed.

Two pictures of the assembled gantry are displayed in Figure 3.8 and Figure 3.9.

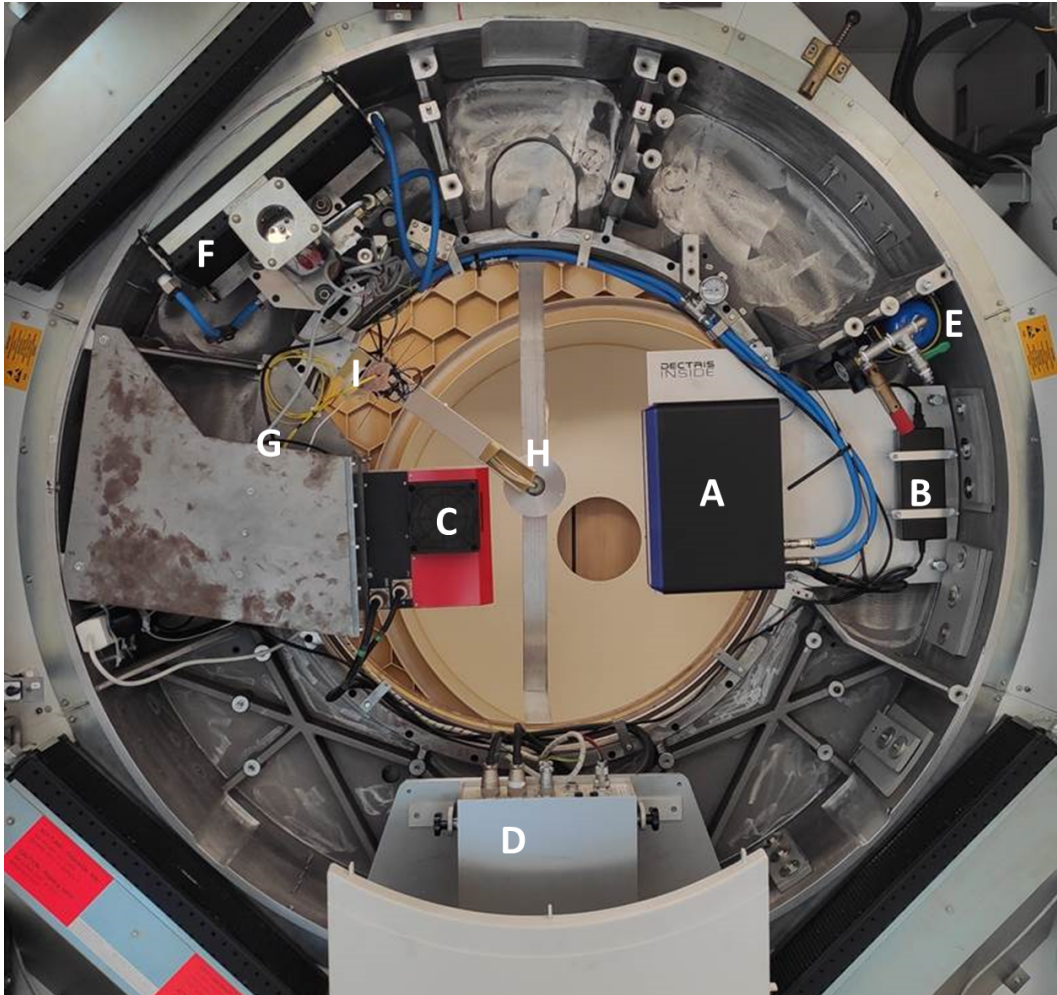


Figure 3.8: Picture of the experimental gantry after the assembling of the new components: detector (A), detector power supply (B), x-ray tube (C), tube control unit (D), dry air bottle (E), water cooling system (F), media converter (G, behind the metal plate), rotary joint (H), Arduino for angular position reading (I).



Figure 3.9: Picture of the front of the experimental gantry with the cover closed and the sample table installed.

3.1.4 Projection Processing and Image Reconstruction

Before the image reconstruction, the projections acquired with the gantry have to be corrected for defective pixels, intermodule gaps, and ring artifacts.

The inpainting of the defective pixels and the intermodule gaps is done via linear interpolation using a predefined mask. The mask was generated by merging the well-defined gaps, the pixels which are always on or off, and the randomly flickering pixels. A dilation (morphological operation) is applied to the mask in order to inpaint also the neighbors of defective pixels. In Figure 3.10, an example of a raw projection before and after the inpainting is shown. The deployed mask is shown as well. As it is possible to notice from the projection of a mouse cadaver, the heart, which is filled with contrast agent, is completely included in the field of measurement. This is obtained thanks to the gantry geometry estimated in Section 3.1.2 and thanks to the finely adjustable sample table (Section 3.1.3).

Another kind of artifact that must be corrected, are ring artifacts. Such artifacts are present in image domain, but herein corrected in projection domain. An example of uncorrected image is shown in Figure 3.11. The visible concentric pattern is due to inhomogeneity in the detector pixel response. In order to correct for that, a ring artifact correction algorithm was implemented by taking inspiration from the work of Clark et al. 2017. All the projections acquired during a scan were averaged and then a 2D median filter (radius=10 pixels)

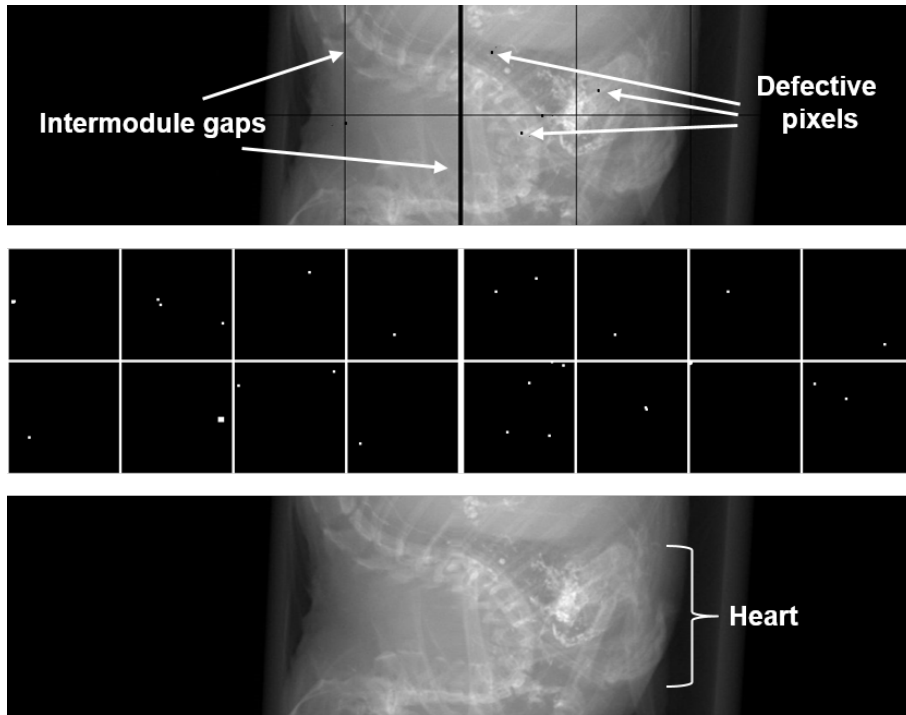


Figure 3.10: Top: Raw projection of a mouse cadaver at the experimental gantry. Center: mask for inpainting of not-working pixels and intermodule gaps. Bottom: corrected projection.

was applied to the obtained mean projection. The original mean projection was subtracted to the filtered mean projection in order to generate a correction projection image. The purpose of the projection's average is to highlight an eventual behavior by each pixel that is consistent during the acquisition. The purpose of the median filter is to ensure that this behavior is not due to any spatial feature of the sample. Finally, the correction image was added to all the original projections. In Figure 3.11, it is possible to see a reconstructed image without and with the ring artifact correction. A substantial improvement is visible.

After the two corrections described, an intrinsic calibration method for geometry estimation was applied (Meng et al. 2013). This is necessary since the real geometry of the assembled gantry can have some slight deviations from the geometry modeled in Section 3.1.2. After having rebinned the projections to the estimated geometry, the CT-volumes could be reconstructed using an FDK algorithm (Feldkamp et al. 1984).

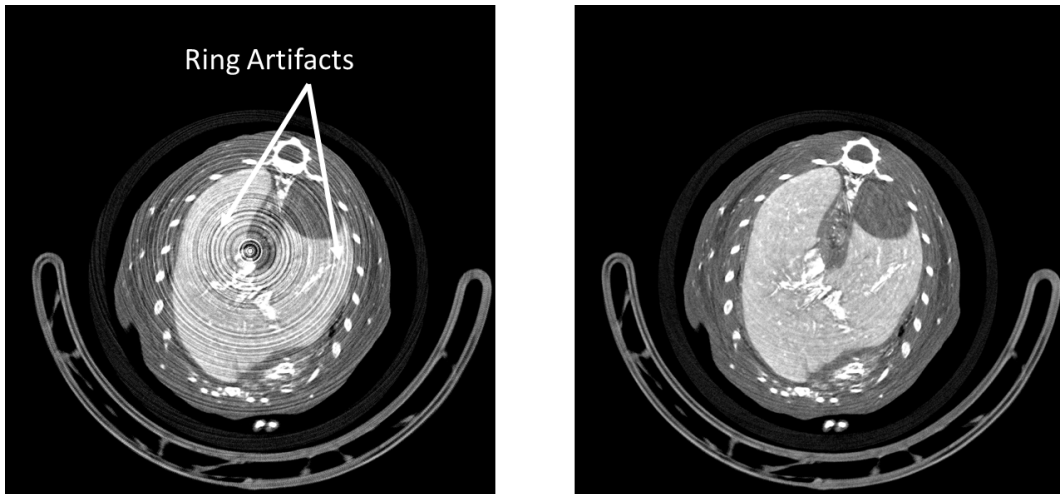


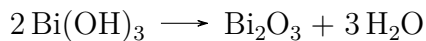
Figure 3.11: Left: axial slice of a mouse cadaver without ring artifact correction. Right: Axial slice corrected for ring artifacts. $C = 750$ HU, $W = 2000$ HU.

3.2 A Novel Contrast Agent for Preclinical Imaging

Within the Eurostars collaboration, a novel high-Z contrast agent was developed by NanoPET Pharma GmbH (Berlin, Germany) for preclinical imaging. In this study, the contrast agent was tested for the first time *in-vivo* using the photon-counting micro-CT described in Section 3.1. The biodistribution of the contrast agent was characterized as a function of time and a proof of concept for multi contrast agent imaging is provided.

3.2.1 Novel Bismuth-Based Contrast Agent by NanoPET Pharma

The novel contrast agent is a nanoparticle agent based on bismuth ($Z=83$, K-edge at 90.5 keV). The nanoparticle core consists of bismuth oxide, which is produced with an aqueous precipitation method:



After the addition of the coating (proprietary information), the nanoparticles are sterilized through autoclaving. The final size of the nanoparticles is 300 nm

and the bismuth concentration is about 200 mg/mL.

As explained in Section 2.3.2, based on the size of the nanoparticles is it possible to expect a circulating time longer than 1 h (blood-pool action) and an accumulation of the agent in the liver and in the spleen, but not in the kidneys.

3.2.2 Characterization of the Contrast Agent Biodistribution

To characterize the biodistribution of the novel bismuth-based contrast agent, *in-vivo* experiments were conducted on mice using the newly assembled experimental gantry (Section 3.1). Four healthy black mice of approximately 25 g were injected with 5 μ L per g of body weight (125 μ L for a 25 g mouse). The mice were scanned before the injection and 0.25, 0.5, 1, 1.5, 2, 3, 4, and 5 h after the injection of the agent. The acquisition settings used for the experiments are listed in Table 3.2. The framerate of 65 fps corresponds to an integration time of 15 ms, which according to Sawall et al. 2020a ensures a sufficient temporal resolution for cardiac and respiratory gating. Despite this, no gating or motion compensation were performed on the measurements because this was out of the scope of this study. A single energy threshold was used and the projections were processed as described in Section 3.1.4 and reconstructed using a voxel size of 34 μ m.

The mice were anesthetized with isoflurane (airflow of 0.5 L/min at 1-2% concentration) by means of a vaporizer (Figure 3.12) and kept under anesthesia via a nose mask which was fixed to the gantry table during measurements (Figure 3.13).

The CT-values were measured in the vena cava, liver, spleen, bladder, kidney, and intestinal walls. The enhancement in the vasculature was measured in the vena cava and not in the heart since the vena cava barely moves during the cardiac and respiratory cycles and images were not compensated for motion. For each organ, the values measured in five ROIs were used to calculate the mean and the standard deviation. By measuring the CT-values as a function of time, it is possible to generate a time-enhancement curve for each organ and evaluate the distribution of the agent.

3.2. A NOVEL CONTRAST AGENT FOR PRECLINICAL IMAGING

Table 3.2: List of the parameters used in the mouse experiments to characterize the biodistribution of the novel bismuth-based contrast agent.

Parameter	Value
Tube voltage	90 kV
Tube current	556 μ A
Additional prefiltration	None
Gantry rotation time	10 s
Framerate	65 fps
Projections per rotation	656
Number of rotations	6
Energy threshold	20 keV
Dose per acquisition	400 mGy



Figure 3.12: Machine used to vaporize the isoflurane and plexiglas box for initial anesthetization of the mice.



Figure 3.13: Picture of an anesthetized mouse on the sample holder at the experimental gantry. A syringe body has been used as nose mask to supply the vaporized isoflurane to the mouse during the acquisition.

3.2.3 Multi Contrast Agent Protocol

One of the main advantages of a non-iodinated contrast agent is the possibility to use it in combination with established iodine-based agents to perform multi contrast agent imaging. Since the two agents have K-edges at different energies, the two elements could in principle be decomposed simultaneously (Section 2.2.2). A novel protocol for multi contrast agent imaging is here proposed and tested for the first time. The novel bismuth-based contrast agent (Section 3.2) is used in combination with the Exytron Myoc 8000 by NanoPET Pharma GmbH (Berlin, Germany), a nanoparticle contrast agent based on iodine. The agent has an iodine concentration of 210 mg/mL, the nanoparticles have a size of 300 nm and a half-life in the vasculature of 120 minutes. Thanks to the proprietary coating of the nanoparticles, the Exytron Myoc accumulates in the myocardium and in the brown adipose tissue even at low doses (50 μ L of injected volume), and provides a contrast enhancement peak in the myocardium approximately 3 h after injection (Sawall et al. 2017).

The proposed multi contrast agent protocol aims at the simultaneous imaging of the myocardium tissue, brown adipose tissue, and vasculature. The protocol is depicted in Figure 3.14 and consist of three steps. The first step consists of the injection of 100 μ L of the iodine-based agent. The mouse can be scanned at this point to visualize the blood-pool phase of the agent. Then, the mouse is let to rest for 3 h so that the agent is cleared from the vasculature and accumulates in the myocardium and in the brown adipose tissue (second step). At this point, 100 μ L of the bismuth-based agent is injected to enhance the vasculature. The scan after the injection of the bismuth agent will then image the late phase of the Exytron Myoc and the early phase of the bismuth agent simultaneously.

To provide a proof of concept of the proposed protocol, an in-vivo experiment was carried out on one healthy mouse (BL6). The mouse was anesthetized as described in the previous section and imaged at the experimental gantry before and after every step of the protocol. The acquisition settings remained the same listed in Table 3.2 with some differences. In order to enable the material decomposition, two energy thresholds were used: the lower threshold remained at 20 keV, whereas the higher threshold was set at 33 keV (iodine K-edge). To optimize the tube voltage for the specific application, the material decomposition performance was tested on a mouse-size calibration phantom (Figure 3.15) composed of vials of water, iodine (10 mg/mL), bismuth (10 mg/mL) and a iodine-bismuth mixture (5 mg/mL each). The phantom was scanned at 90 kV and 60 kV with 6 and 11 rotations, respectively, to match the dose. For both acquisitions, the contrast-to-noise ratio was measured in the iodine and bismuth vials in the corresponding material map. The CT-scan of the phantom and the material maps of iodine and bismuth are displayed in Figure 3.15. On average, the contrast-to-noise ratio of

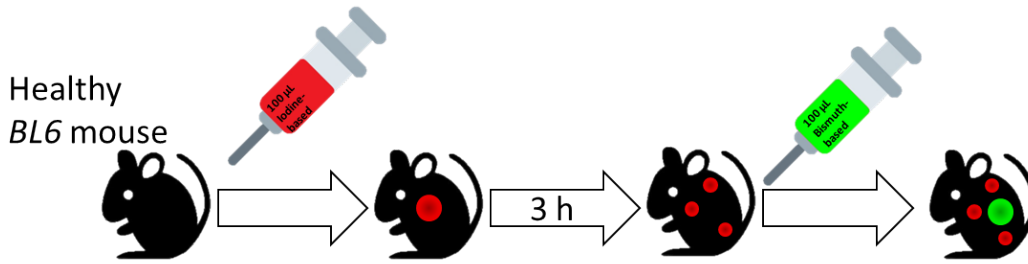


Figure 3.14: Multi contrast agent protocol for imaging the brown adipose tissue, the myocardium, and the vasculature at the same time. The iodine-based agent (Exitron Myoc) is injected first. After 3 h, the iodine agent is cleared from the vasculature and it accumulates in the brown adipose tissue and in the myocardium. The novel bismuth agent is then injected to enhance the vasculature.

the acquisition at 60 kV resulted 25% higher than the one measured at 90 kV. Therefore, the acquisitions for the multi contrast agent protocol were performed at 60 kV and 11 rotations.

The performed material decomposition is an image-based decomposition which uses water (H_2O), iodine and bismuth as basis function. A volume conservation equation is added to the system of equations (2.16) in order to decompose three materials with two energy thresholds (L. Yu et al. 2009):

$$\mu(\mathbf{r}, E_1) = a_{\text{H}_2\text{O}}(\mathbf{r})\mu_{\text{H}_2\text{O}}(E_1) + a_{\text{I}}(\mathbf{r})\mu_{\text{I}}(E_1) + a_{\text{Bi}}(\mathbf{r})\mu_{\text{Bi}}(E_1) \quad (3.5)$$

$$\mu(\mathbf{r}, E_2) = a_{\text{H}_2\text{O}}(\mathbf{r})\mu_{\text{H}_2\text{O}}(E_2) + a_{\text{I}}(\mathbf{r})\mu_{\text{I}}(E_2) + a_{\text{Bi}}(\mathbf{r})\mu_{\text{Bi}}(E_2) \quad (3.6)$$

$$1 = a_{\text{H}_2\text{O}}(\mathbf{r}) + a_{\text{I}}(\mathbf{r}) + a_{\text{Bi}}(\mathbf{r}) \quad (3.7)$$

, where E_i is the i -th energy bin, μ_m and a_m are the attenuation coefficient and the material map of the m -th basis material, respectively.

In order to invert the system, it is essential to first characterize the basis materials. To do so, the aforementioned phantom composed of water, 10 mg/mL iodine solution and 10 mg/mL bismuth solution was scanned using the same acquisition settings of the multi contrast agent protocol. Then, the attenuation coefficients of the three materials were measured in the two energy bins to obtain $\mu_{\text{H}_2\text{O}}$, μ_{I} and μ_{Bi} .

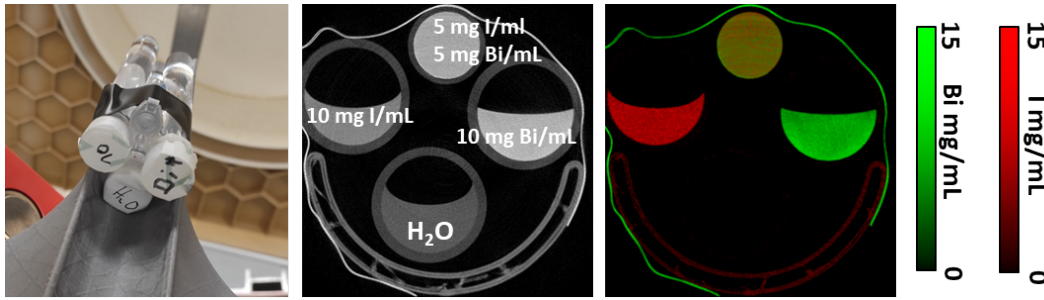


Figure 3.15: Left: Mouse-size multi contrast agent phantom composed of four vials of water, 10 mg/mL iodine solution, 10 mg/mL bismuth solution, 5 mg/mL iodine and 5 mg/mL bismuth solution. Center: CT image. Right: material decomposition.

3.3 Potential of High-Z Elements for Clinical Contrast-Enhanced CT

As described in Section 2.3, only iodine-based contrast agents are allowed for intravenous injections in clinical CT imaging. From a physical point of view, these elements may not be the best choice since their K-edges (Section 2.1.2) are at relatively low energy if compared to the spectra used clinically. Therefore, in a usual clinical scenario, the a K-edge of iodine or barium is not exploited. Having an element with K-edge in the transmitted spectrum can offer many benefits concerning contrast enhancement and material decomposition.

These opportunities are even more fascinating if a PC-detector (Section. 2.2) is used since such detector has multiple energy thresholds which can be adjusted according to the K-edge of the deployed element. In this first study, the potentials of high-Z elements in contrast-enhanced PC-CT are evaluated as a function of tube voltage, filtration setting, patient size, and energy-threshold settings.

3.3.1 Contrast in Photon-Counting CT

The contrast-to-noise ratio (CNR) is a basic figure of merit to assess the contrast provided by a contrast agent. The CNR is defined as:

$$\text{CNR} = \frac{\Delta\mu}{\sqrt{V}} = \frac{|\mu_A - \mu_B|}{\sqrt{V}}, \quad (3.8)$$

where $\mu_{A/B}$ are the mean CT-values measured in a contrast-enhanced and in an unenhanced soft-tissue region of interest (ROI), respectively. V is the variance of pixel values measured in a homogeneous region.

Since the tube voltage and the spectrum filtration are being varied in this study,

the CNR has to be normalized for the patient absorbed dose D . By normalizing also for the concentration C of each contrast agent, it is possible to define the CNR at unit dose and at unit concentration (CNRC D):

$$\text{CNRC D} = \frac{\text{CNR}}{C\sqrt{D}} \quad . \quad (3.9)$$

Since in PC-CT multiple energy thresholds are available, multiple bin images (f_i) are acquired simultaneously. These images can be combined to calculate a composed image. In the case of two energy thresholds, the composed image f_{PC2} can be calculated as:

$$f_{\text{PC2}} = w_1 f_1 + w_2 f_2 \quad , \quad (3.10)$$

where $w_{1/2}$ are the weighting coefficients and $w_1 + w_2 = 1$. The CNR of the composed image can be directly computed as:

$$\text{CNR}_{\text{PC2}} = \frac{(w_1 \Delta\mu_1 + w_2 \Delta\mu_2)^2}{w_1^2 V_1 + w_2^2 V_2} \quad . \quad (3.11)$$

In order to maximize the CNRC D of the composed image, the weights can be chosen $w_i \propto \Delta\mu_i/V_i$. In this scenario, the CNRC D of the final image can be directly calculated as (L. Yu et al. 2011, Faby et al. 2015, Sawall et al. 2020b):

$$\text{CNRC D}_{\text{max}} = \sqrt{\text{CNRC D}_1^2 + \text{CNRC D}_2^2} \quad , \quad (3.12)$$

where CNRC D_i is the CNRC D of the i -th bin image.

3.3.2 Experimental Setup

In order to simulate an adult patient, a semi-anthropomorphic liver phantom (QRM, Möhrendorf, Germany) (figure 3.16) was equipped with a 2.5 cm fat ring to reach a final size of 35 cm \times 25 cm. Five vials were filled with solutions of high-Z elements (Table 3.3) and placed in the liver insert of the phantom. The solution concentrations were chosen to simulate values that can be found in clinical realistic scenarios. An iodine-based contrast agent used in clinical CT practice (OptirayTM 300, Covidien, Neustadt/Donau, Germany) was diluted with water to obtain a final iodine concentration of 14.2 mg/mL. For the gadolinium vial, a gadolinium-based contrast agent used in magnetic resonance imaging (Multihance[®] 0.5 M, Bracco, Milan, Italy) was diluted with water to obtain a final gadolinium concentration of 15.8 mg/mL. The ytterbium, tungsten and bismuth acid solutions were purchased directly with a concentration of 10 mg/mL and no further dilution was needed. A broad range of K-edges is available with these solutions. The gold

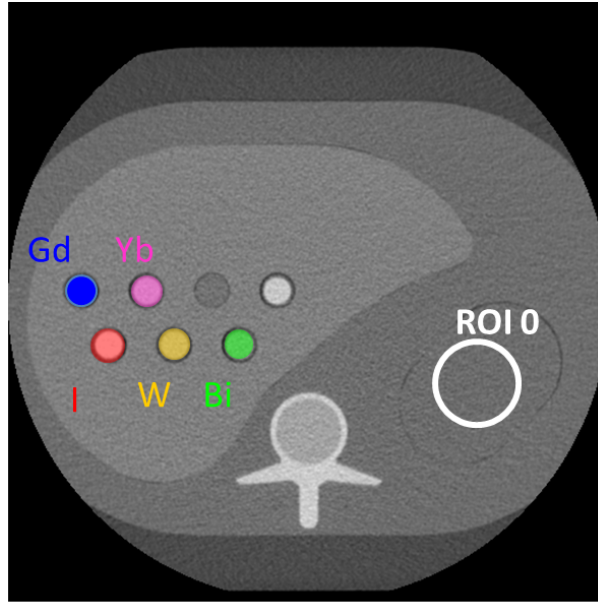


Figure 3.16: Adult liver phantom with high-Z solution inserts. The phantom is cropped because of the limited FOV of the PC detector of the Siemens SOMATOM CounT.

standard iodine is at the lower limit with its K-edge at 33.2 keV. Since there are nearly no transmitted photons below 33.2 keV (see figure 2.9), elements with a K-edge lower than iodine were neglected. The bismuth is the upper limit since it is the stable element with the highest K-edge (90.5 keV).

The SOMATOM CounT scanner was used to acquire all the measurements. The SOMATOM CounT is a whole-body PCCT prototype by Siemens Healthineers, Forchheim, Germany. The scanner is based on the SOMATOM Definition Flash, a dual-source scanner where a PC detector is installed in place of one of the two EI detectors (Kappler et al. 2014, Z. Yu et al. 2016a). Only the PC detector was used for this study. The PC detector has a 1.6 mm CdTe sensitive layer with a pixel size of 225 μm and a bias voltage of 1000 V. Up to four energy thresholds can be used, according to the used mode. The Macro mode was used for all the measurements of this study. In Macro mode the pixels are binned in a 4×4 pattern, resulting in a pixel size of 900 μm . The PC detector is smaller than the EI detector and has a field of view (FOV) of 27.5 cm. When objects larger than 27.5 cm are scanned, an additional data completion scan has to be performed with the EI detector to avoid truncation artifacts (Z. Yu et al. 2016b).

Two sets of measurements were acquired and used for comparison with simula-

Table 3.3: List of the contrast agents and high-Z solutions used in measurements. The same formulations were used in the simulations.

High-Z Element	K-edge	Material and concentration	Composition	Concentration of the solution
I	33.2 keV	Optiray 300 300 mg I/mL	$C_{18}H_{24}I_3N_3O_9$ in H_2O	14.2 mg I/mL
Gd	50.2 keV	Multihance 0.5 M 78 mg Gd/mL	$C_{36}H_{65}GdN_5O_{21}$ in H_2O	15.8 mg Gd/mL
Yb	61.3 keV	Ytterbium Oxide 10 mg Yb/mL	Yb_2O_3 in 5% HNO_3	10.0 mg Yb/mL
W	69.5 keV	Tungsten 10 mg W/mL	W in 10% NH_3	10.0 mg W/mL
Bi	90.5 keV	Bismuth 10 mg Bi/mL	Bi in 10% HNO_3	10.0 mg Bi/mL

tions. For the first set, the CNRCD of the different solutions was evaluated as a function of the tube voltage. A single energy threshold (T_0) at 20 keV was used while scanning the phantom with a tube voltage of 80, 100, 120, and 140 kV. For the second set of measurements, the CNRCD of the solutions was measured with a fixed tube voltage and two energy thresholds. The aim of this measurement is to assess the relationship between the high-Z element K-edges and the threshold values. The lower threshold (T_0) was set at 20 keV, and the higher threshold (T_1) was varied between 50 keV and 90 keV, which is the maximum values available at the scanner. In order to avoid photon starvation in the high energy bin image for high values of T_1 , the tube voltage was fixed at 120 kV. The CNRCD was evaluated in the individual bin images and the $CNRCD_{max}$ was evaluated for the optimally combined image (Equation. 3.12).

The latter set of measurements, which was performed with two energy thresholds, was also used to evaluate the material decomposition performance of the different high-Z solutions. For each high-Z element, the set of two bin images was used to perform a two material decomposition (Section 2.2.2) of the soft tissue and of the specific element. Then the CNRCD was evaluated in the material map of the decomposed element.

3.3.3 Simulations

In order to investigate a wider range of scenarios, the whole body PC-CT system was modeled through simulations according to the specification of the Siemens

3.3. POTENTIAL OF HIGH-Z ELEMENTS FOR CLINICAL CONTRAST-ENHANCED CT

Table 3.4: List of the parameters used to simulate the PCCT.

Parameter	Value
Source to isocenter distance	595 mm
Detector to isocenter distance	490 mm
Detector pixel size	225 μm
Pixel binning	4×4
Detector material	CdTe, 6.3 g/cm ³
Detector thickness	1.6 mm
Bias voltage	1000 V
Prefilters	6.8 mm Al, 1.0 mm C, 0.7 mm Ti , 0.008 mm W
Voxel size	0.78 mm

SOMATOM CounT. The gantry geometry and the detector parameters are listed in Table 3.4. The x-ray source was modeled as a point source using a semiempirical spectrum model (Barnes et al. 1991) and prefilters (see Table 3.4) were applied to harden the spectrum. Scans of a 3D model of the liver phantom were simulated using 1024 projections and circular trajectories. For each projection and each detector pixel, the number of photons n transmitted through the phantom and detected in the b -th energy bin was evaluated using the following forward model:

$$n_b = \int_0^{E_{\max}} \Phi(E) \cdot s_b(E) \cdot e^{-\sum_{m=1}^M \mu_m(E) \cdot L_m} \cdot dE \quad , \quad (3.13)$$

where $\Phi(E)$ is the spectrum in air already prefiltered, $s_b(E)$ is the bin sensitivity, L_m is the intersection length through the different materials m of the phantom and $\mu_m(E)$ is the material attenuation coefficient. The bin sensitivity (Section 2.2.1) was calculated using the semirealistic detector model described in Faby et al. 2016 (Figure 3.17). Poisson noise was added to the photon number, the projection values were calculated and then the water precorrection was applied. A 4×4 pixel binning was applied on the detector elements since the measurements were acquired in Macro mode. Finally, the volume was reconstructed using the FDK cone-beam algorithm (Feldkamp et al. 1984). The $\text{CTDI}_{\text{vol } 32 \text{ cm}}$ was estimated for each scan using in-house developed Monte Carlo simulations. The Monte Carlo code has been verified against Geant4 and further details can be found in Baer et al. 2012.

Two sets of simulations were performed: the first one for direct comparison with measurements and the second to investigate further high-Z elements, patient sizes, and filtration settings.

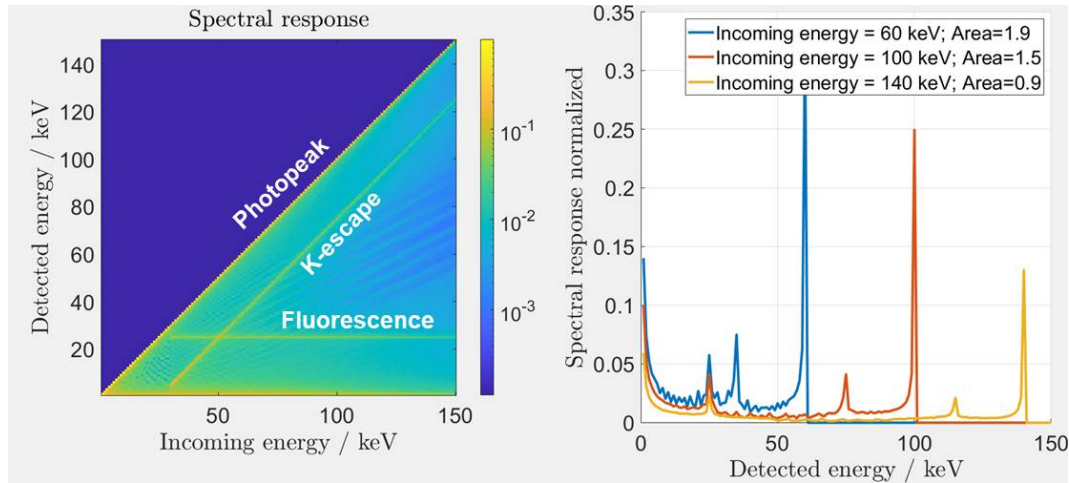


Figure 3.17: Spectral response of the PC detector of the Siemens SOMATOM CounT. Left: 2D plot of the spectral response between 0 keV and 150 keV for incoming photons with energy up to 150 keV. Right: spectral response for an incoming photon energy of 60 keV, 10 keV and 140 keV.

In the first set, the adult-sized liver phantom was equipped with five high-Z solution vials. The composition and the concentration of the vials were simulated according to the ones used in the measurements (Table 3.3). The concentration of the solvent was slightly adjusted (within 5%) to match the attenuation of each solution. The scans of the adult-sized phantom were simulated using a tube voltage between 70 kV and 150 kV in steps of 5 kV. A single threshold at 20 keV was used. Phantom scans were also simulated for a fixed tube voltage (120 kV) and two energy thresholds. In this case, as in the measurements, the low energy threshold T_0 was set at 20 keV and the high threshold T_1 was varied between 50 keV and 90 keV in 5 keV steps.

The second set of simulations was performed using more high-Z elements, different patient sizes, and different prefiltrations of the x-ray beam. The model of the phantom was equipped with seven vials containing solutions of iodine, cerium, gadolinium, ytterbium, tungsten, gold, and bismuth. In this case, ideal water solutions were used and the concentration of the high-Z elements was set to 10 mg/mL (Table 3.5). Further than the adult-sized phantom (35 cm \times 25 cm), the 3D model of the phantom was scaled to simulate an infant patient (15 cm \times 10 cm) and an obese patient (50 cm \times 40 cm). The number of pixels in the detector rows was scaled according to the different phantom sizes. In this way, each phantom could fit the field of view without the need of an additional data completion scan. Each phantom size was scanned with two sets of prefilters: the first one is the one already used for the previous simulations and measurements (Table 3.4), whereas the second one includes an additional 0.4 mm Sn filter. The

3.3. POTENTIAL OF HIGH-Z ELEMENTS FOR CLINICAL CONTRAST-ENHANCED CT

Table 3.5: List of the ideal high-Z solutions used in simulations. The contrast enhancement refers to the simulation of the adult size phantom at 100 kV without Sn filter. The contrast enhancement with respect to water was measured in each vial in the low threshold image ($T_0= 20$ keV).

High-Z Element	K-edge	Concentration of the solution	Contrast enhancement at 100 kV
I	33.2 keV	10.0 mg I/mL	305 HU
Ce	40.4 keV	10.0 mg Ce/mL	370 HU
Gd	50.2 keV	10.0 mg Gd/mL	422 HU
Yb	61.3 keV	10.0 mg Yb/mL	357 HU
W	69.5 keV	10.0 mg W/mL	287 HU
Au	80.7 keV	10.0 mg Au/mL	246 HU
Bi	90.5 keV	10.0 mg Bi/mL	232 HU

latter was chosen since it is already present in the Siemens Flash and in the Siemens CounT scanners. The simulations were performed for each phantom size and each prefiltration setting using an energy threshold fixed at 20 keV and varying the tube voltage between 70 kV and 150 kV.

3.3.4 Image Analysis

The CNRCD (Equation (3.9)) provided by the different high-Z solutions in the different scenarios was evaluated both in measurements and in the simulations. For each solution, the contrast was measured with respect to water, therefore in Equation (3.8) the CT-value of the background was set to 0 HU. A homogeneous region in the soft tissue (ROI0 in Figure 3.16) was used to measure the noise as the variance of the pixel values. Whenever two energy thresholds are used, the CNRCD was measured in both bin images and the CNRCD_{\max} (Equation 3.12) was measured in the combined image. The error on the CNRCD was quantified as the standard deviation of the CNRCD over the different slices. For each scenario, the measured CNRCD of each high-Z solution was normalized to the CNRCD of iodine (gold standard) at a reference tube voltage (U_{ref}) without Sn filter:

$$\text{Relative CNRCD}_X(U) = \frac{\text{CNRCD}_X(U)}{\text{CNRCD}_I(U_{\text{ref}}, 0 \text{ mm Sn})} \quad . \quad (3.14)$$

The reference voltage was adjusted according to the different patient sizes: 80 kV for the infant phantom, 100 kV for the adult phantom and 120 kV for the obese phantom.

The relative CNRCD can be used to quantify the potential dose reduction as:

$$\text{Dose Reduction}_X(U) = 1 - \left(\frac{\text{CNRCD}_I(U_{\text{ref}}, 0 \text{ mm Sn})}{\text{CNRCD}_X(U)} \right)^2 . \quad (3.15)$$

In the different scenarios, only values of the relative CNRCD and dose reduction obtained for a tube voltage higher than U_{ref} were considered. This is because the usage of lower tube voltages could be limited by the power of the x-ray tube. This limitation could lead to undesired long scan time, especially for obese patients (Kalender et al. 2009).

4 | Results

4.1 A Novel Contrast Agent for Preclinical Imaging

In this section, the *in-vivo* results concerning the novel bismuth-based contrast agent are presented. First, the biodistribution of the agent in mice is evaluated as a function of time, then the multi contrast agent protocol described in Section 3.2.3 is presented.

4.1.1 Characterization of the Contrast Agent Biodistribution

Four BL6 healthy mice were injected with the novel bismuth-based contrast agent (Section 3.2.1) and measured using the assembled CT experimental gantry (Section 3.1). The contrast enhancement in the different organs was measured as a function of time as described in Section 3.2.2 and averaged over the four mice. The time-dependent signal enhancement curves are shown in Figure 4.1 for the vasculature and the main abdominal organs.

As a baseline, Figure 4.2 and Figure 4.3 show the CT images of a mouse thorax and abdomen prior the injection. As it is possible to see, no contrast enhancement is present in the vasculature and soft tissues. Despite it is possible to recognize the shape of some organs like the heart and the liver, most of the organs and soft tissues exhibit approximately the same CT-value of 100 ± 50 HU. Especially in the abdomen, it is impossible to discern the different organs of the digestive and urinary systems.

Right after the injection of the agent, the same thorax CT (Figure 4.4) image shows a significant contrast enhancement in the vasculature. The mean CT-value measured in the vena cava is 1200 ± 200 HU. This is defined as the early phase of the contrast agent. The myocardium and the liver are clearly visible and it

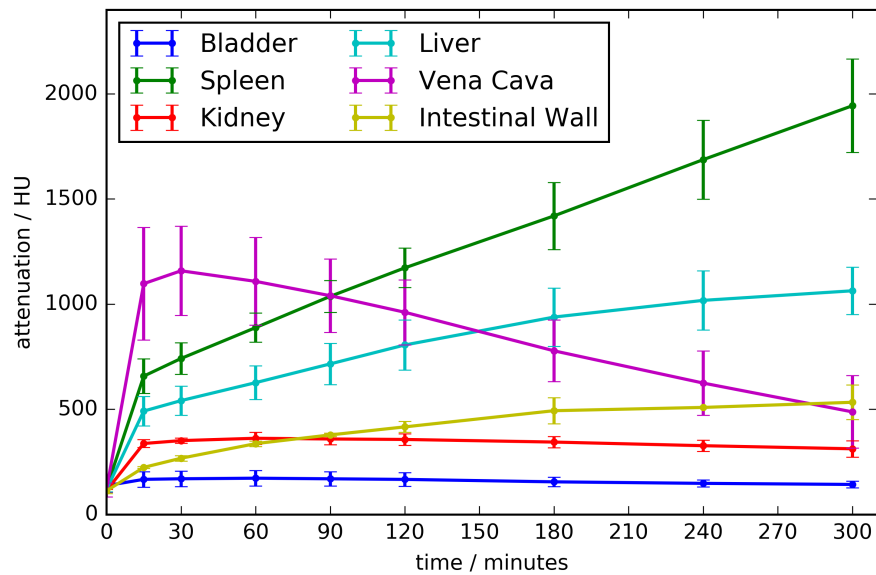


Figure 4.1: Time-dependent signal enhancement curves for the mice experiment with the novel bismuth-based contrast agent. The measurements at 0 minutes are performed before the injection of the agent.

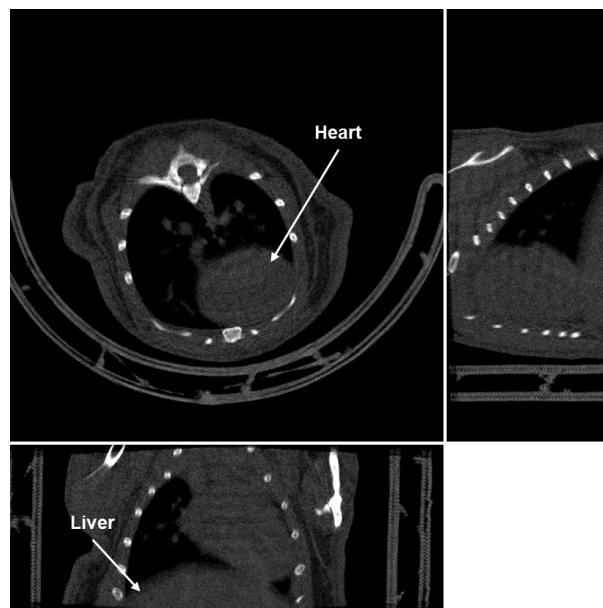


Figure 4.2: Axial, sagittal and coronal views of a mouse thorax before the injection of the bismuth contrast agent. The CT-value of soft tissue is about 100 ± 50 HU. $C = 750$ HU, $W = 2000$ HU.

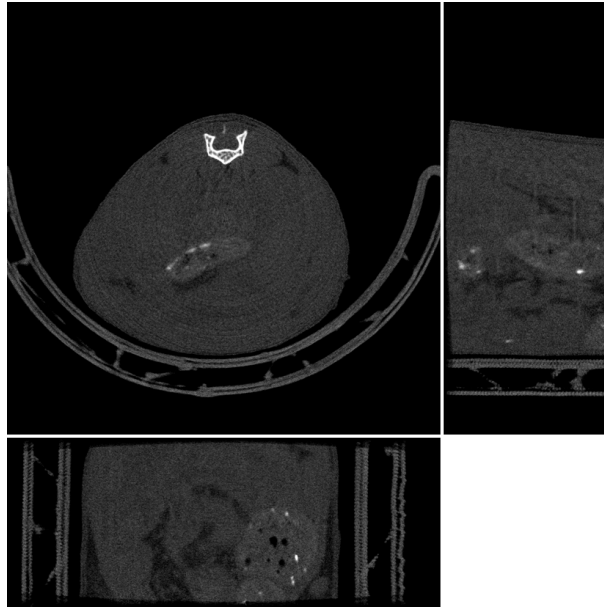


Figure 4.3: Axial, sagittal and coronal views of a mouse abdomen before the injection of the bismuth contrast agent. The CT-value of soft tissue is about 100 ± 50 HU. $C = 750$ HU, $W = 2000$ HU.

is possible to discern the myocardium from the atria and ventricles even if the measurements are not compensated for cardiac or breathing motion. A slight contrast enhancement of 350 HU is measured in the kidney. This is mostly due to the difficulty to place an ROI in the kidney which does not include vessels.

As time passes by, the contrast agent is cleared from the vasculature and it starts to accumulate in the liver and in the spleen. This is defined late phase and is shown in Figure 4.5, where the mouse was scanned 5 h after the injection. At the end of the measurements (5 h after the injection), the spleen has a CT-value of 1940 ± 220 HU, whereas the liver has a CT-value of 1060 ± 100 HU. The half-life of the contrast agent in the vasculature is estimated to be around 250 minutes.

An interesting finding of this study was that the contrast agent slowly accumulates in the intestinal walls as well. As it is shown in Figure 4.1 by the yellow line, the CT-value of the intestinal walls monotonically increases after the injection and reaches a value of 530 ± 80 HU at the end of the measurements. The slope of the curve suggests that the contrast in the intestinal wall could further increase if the measurements are acquired more than 5 h after the injection. The contrast enhancement of the intestinal walls is shown in Figure 4.6, where the abdominal CT images of a mouse were acquired 3.5 h after the injection. Up to my knowledge,

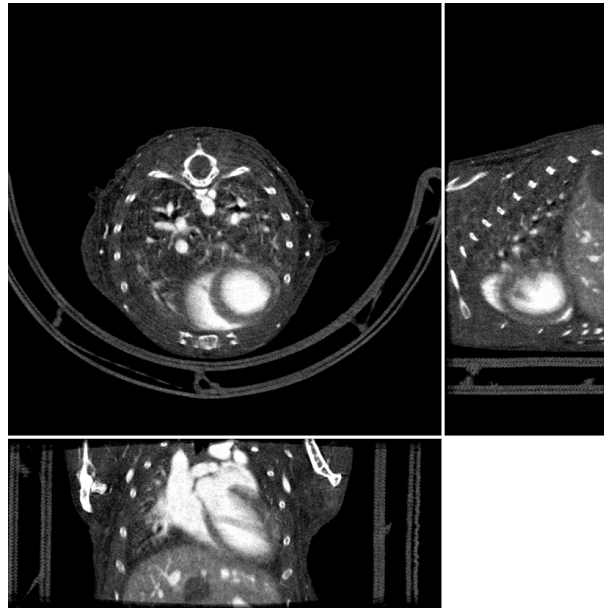


Figure 4.4: Axial, sagittal and coronal views of a mouse thorax right after the injection of the bismuth contrast agent (early phase). The CT-value of the vasculature is 1200 ± 200 HU. $C = 750$ HU, $W = 2000$ HU.

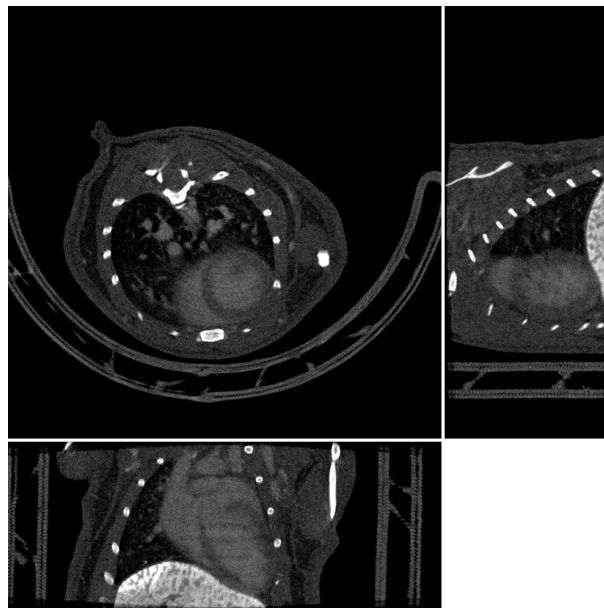


Figure 4.5: Axial, sagittal and coronal views of a mouse thorax 5 h after the injection of the bismuth contrast agent (late phase). The contrast agent is almost completely been cleared from the vasculature and it accumulates in the liver. $C = 750$ HU, $W = 2000$ HU.

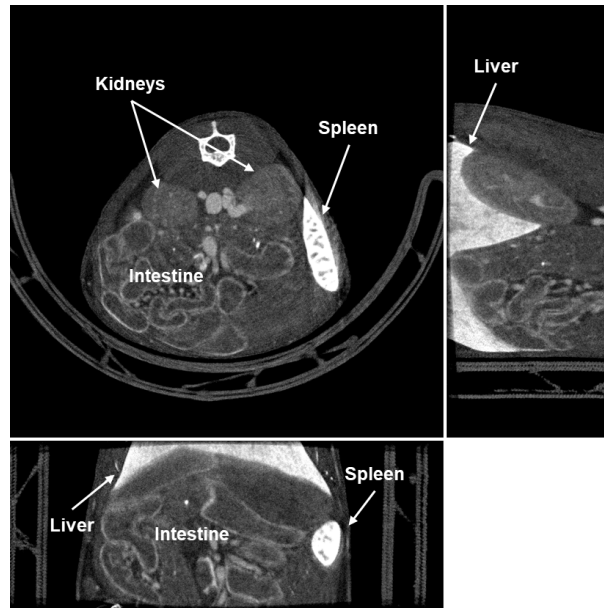


Figure 4.6: Axial, sagittal and coronal views of a mouse abdomen 3.5 h after the injection of the bismuth contrast agent (late phase). The contrast agent is being cleared from the vasculature and it accumulates in the spleen and in the intestinal walls. $C = 750$ HU, $W = 2000$ HU.

it is the first time a CT contrast agent exhibits such behavior. No other examples of contrast agents accumulating in the intestinal walls were found in the literature. The specific behavior of the contrast agent is probably due to the engineered coating of the bismuth nanoparticles, which is a property of NanoPET Pharma. In the same image of the abdomen, the spleen and the liver are visible.

For all the measurements, no contrast enhancement was measured in the bladder, confirming that the nanoparticle-based contrast agent is not cleared from the system as usual agents based on small molecules. Furthermore, no enhancement was measured in the muscle tissue, adipose tissue, or brain.

4.1.2 Multi Contrast Agent Protocol

The multi contrast agent protocol described in Section 3.2.3 was tested in-vivo for the first time. One mouse was injected with 100 μ L of Exitron Myoc 8000 (iodine-based) and then it was left to rest for 3 h. According to the finding of Sawall et al. 2017, during this time the agent is cleared from the vasculature and it accumulates in the liver, spleen, myocardium, and brown adipose tissue.

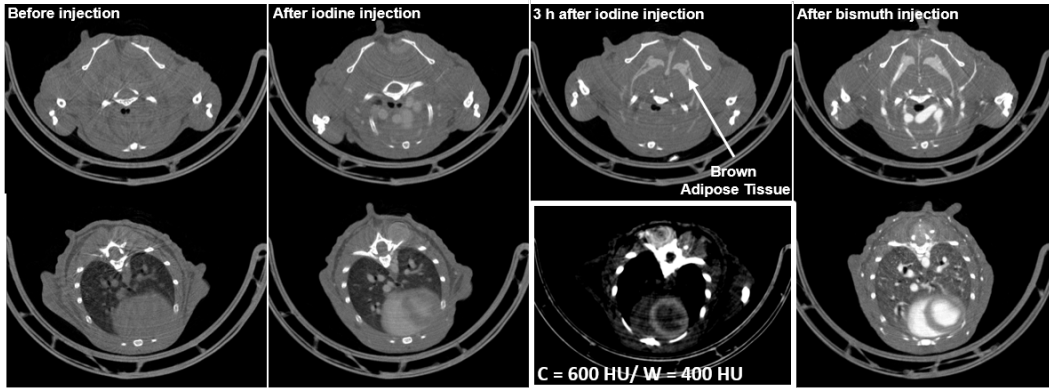


Figure 4.7: Axial CT-images of the multi contrast agent protocol. From left to right: before the injection, after the injection of the Exitron Myoc (vasculature enhancement), 3 h after the injection of the Exitron Myoc (myocardium and brown adipose tissue enhancement), after the injection of the bismuth agent (vasculature enhancement). Top row: axial slices across the mouse shoulders. Bottom row: axial slice across the mouse thorax. $C = 750$ HU, $W = 2000$ HU.

The mouse was scanned before, right after, and 3 h after the injection of Exitron Myoc. After the 3 hours of rest, the mouse was injected with 100 μ L of the novel bismuth-based contrast agent and scanned again. In Figure 4.7 two axial slices are shown for each time point. Before the injection, no contrast enhancement is visible in the vasculature or in other tissue. Right after the injection, the contrast agent is in its early phase, therefore the vasculature is enhanced. Around 3 h after the injection, the iodine-based agent is cleared from the vasculature and it accumulates in the brown adipose tissue, myocardium, spleen, and liver. After the injection of the bismuth-based agent, the vasculature is enhanced again and both contrast agents are visible at the same time. This is particularly noticeable in the axial slice across the shoulder of the mouse, where both the brown adipose tissue and the vessels are enhanced by the two contrast agents.

By performing a three material decomposition as described in Section 3.2.3, it is possible to display the material map of each individual contrast agent and to quantify the amount of contrast agent in each organ. The decomposition of the acquisition after the iodine injection is shown in Figure 4.8. As it is possible to see, the vasculature is filled with iodine with a concentration of 6.5 ± 0.3 mg/mL. The K-edge of bismuth is not exploited in this case, since its K-edge is at 90.5 keV whereas the measurements were acquired with a 60 kV tube voltage. This means that highly attenuating materials like bone cannot be differentiated by bismuth and can be found in the material map of bismuth.

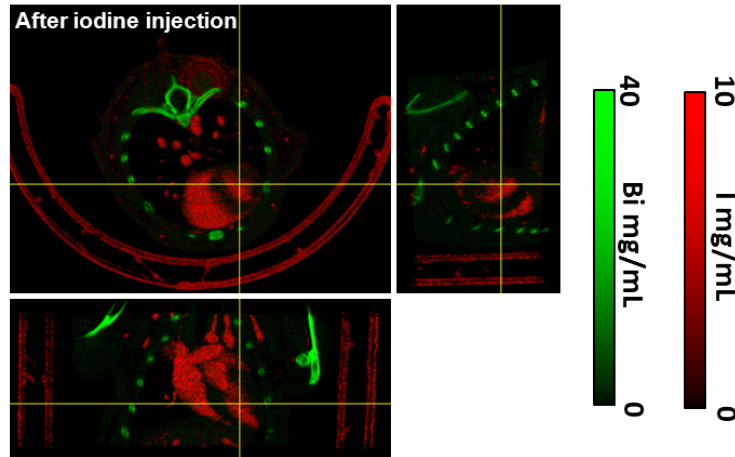


Figure 4.8: Axial, sagittal and coronal views of the material decomposition of the mouse thorax right after the injection of iodine agent (early phase). The vasculature is decomposed as iodine, whereas the bone is decomposed as bismuth.

After 3 h, the material decomposition shows an accumulation of iodine in the brown adipose tissue (11.0 ± 1.0 mg/mL) (Figure 4.9) and in the myocardium (0.7 ± 0.2 mg/mL) (Figure 4.10). The material map of iodine in Figure 4.10 had to be smoothed with a 3D Gaussian filter ($\sigma=3$ pixels) and it had to be displayed with a very narrow window (1 mg/mL) in order to properly visualize the iodine in the myocardium. The ring artifact at the center of the image which is slightly decomposed as iodine, became much more visible with these display settings. The material decomposition after the injection of the bismuth agent is displayed in Figure 4.11 and 4.12. The bismuth in the vasculature is properly decomposed as bismuth and its concentration is 18.8 ± 0.4 mg/mL. The overlay of iodine and bismuth maps provides a simultaneous visualization of the two contrast agents distribution: the vessels and the heart filled with bismuth and the brown adipose tissue and the myocardium containing iodine.

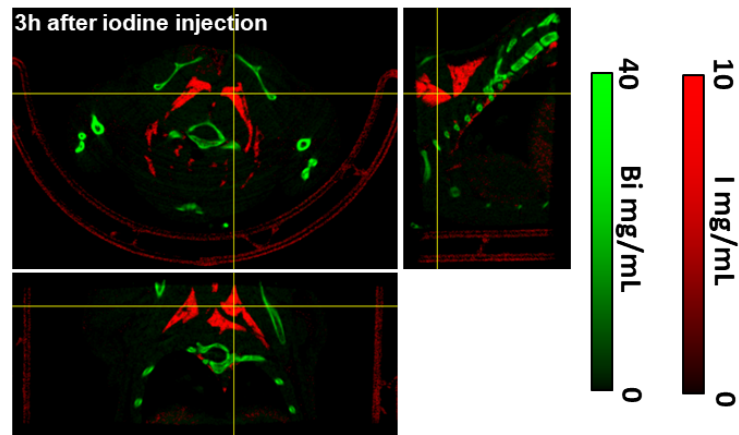


Figure 4.9: Axial, sagittal and coronal views of the material decomposition of the mouse shoulders 3 h after the injection of iodine agent (late phase). The brown adipose tissue is decomposed as iodine, whereas the bone is decomposed as bismuth.

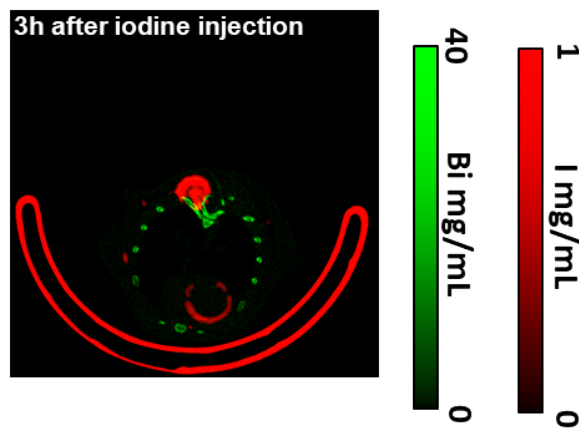


Figure 4.10: Axial view of the material decomposition of the mouse thorax 3 h after the injection of iodine agent (late phase). The iodine material map was smoothed with a 3D Gaussian filter ($\sigma=3$ pixels) to visualize the myocardium. A ring artifact is visible at the center of the image.

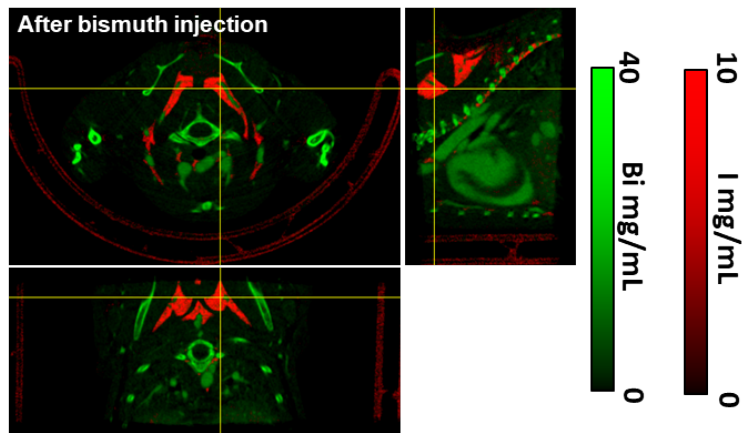


Figure 4.11: Axial, sagittal and coronal views of the material decomposition of the mouse shoulders right after the injection of bismuth agent (early phase). The brown adipose tissue is decomposed as iodine, whereas the bone and the vasculature are decomposed as bismuth.

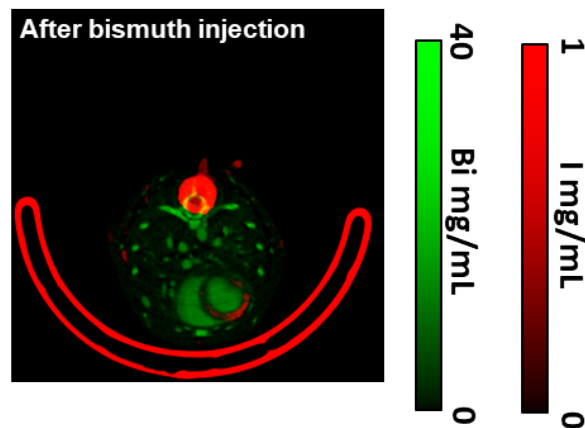


Figure 4.12: Axial view of the material decomposition of the mouse thorax right after the injection of bismuth agent (early phase). The iodine material map was smoothed with a 3D Gaussian filter ($\sigma=3$ pixels) to visualize the myocardium. A ring artifact is visible at the center of the image. The bone and the vasculature are decomposed as bismuth.

4.2 Potential of High-Z Elements for Clinical CT

In the following, the results on the contrast enhancement of high-Z elements are presented. In Section 4.2.1, the measurements are presented together with the simulations of the realistic high-Z solutions. Then, in Section 4.2.2, the simulations with ideal high-Z solutions, different patient sizes, and prefiltrations are presented. The results achieved in this study have been collected in a publication for the journal *Medical Physics* (Amato et al. 2020).

4.2.1 Measurements

The first measurement of the adult liver phantom was performed with the five high-Z solutions of iodine, gadolinium, ytterbium, tungsten, and bismuth (Table 3.3). The CNRCDs measured in the low threshold image ($T_0 = 20$ keV) are plotted (dots) in figure 4.13 as a function of the tube voltage U . The values were normalized for the CNRCD of iodine at 100 kV. In the same plot, the simulations of the realistic solutions are shown as continuous lines for comparison and validation. The CNRCD of iodine decreases as the tube voltage increases, accordingly with the fact that its K-edge is at too low energy compared to the used spectra. The other solutions exhibit a maximum which can be found at increasing tube voltages as the energy of the K-edge increases. For gadolinium, the maximum is at approximately 80 kV, whereas for tungsten it is at 110 kV. Gadolinium outperforms the other high-Z solutions for all tube voltages, with a measured maximum of 1.75 at 80 kV.

Good agreement between measurements and simulations is found. The relative deviations between the measured and simulated points were evaluated: a mean deviation of 4% is found, with a maximum deviation of 9% for gadolinium at 80 kV.

The second set of measurements aimed to evaluate how a set of two energy thresholds can be used to maximize the CNRCD. At a fixed tube voltage of 120 kV and with a variable T_1 , the CNRCD of the solutions was measured in the low and high energy bin images. These values were also combined to calculate the CNRCD_{\max} (Equation (3.12)). In Figure 4.14 left, the measured and simulated CNRCDs of the tungsten solution are shown as a function of the high threshold T_1 . As T_1 increases, the CNRCD of the low and high energy bin image exhibits an increasing and decreasing behavior, respectively. The measured CNRCD_{\max} is instead almost constant for T_1 between 50 keV and 70 keV. For higher values of T_1 , the CNRCD_{\max} decreases up to 10%, probably because of photon starvation in the high-energy bin image. For each solution, the CNRCD_{\max} is plotted in figure 4.14

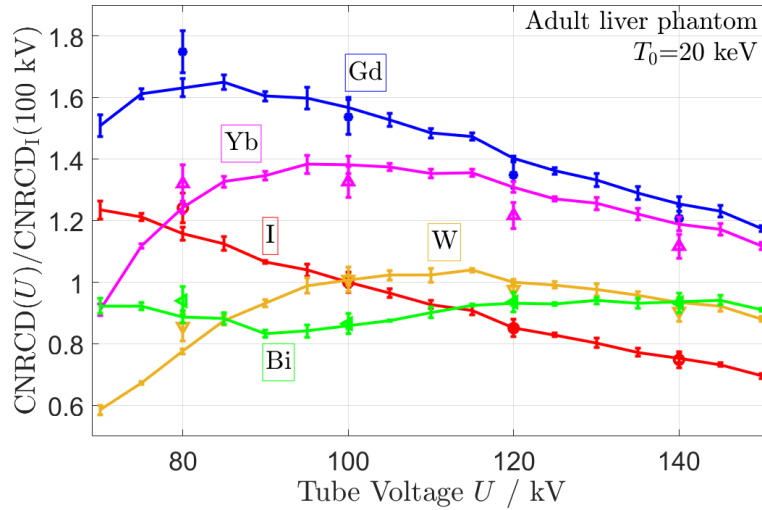


Figure 4.13: For the adult liver phantom, the CNRCD in the low threshold image ($T_0 = 20$ keV) of high-Z element solutions as function of the tube voltage. Values are normalized for the value of iodine at 100 kV. Measurements are displayed with discrete markers, whereas simulations are displayed with continuous lines.

right. The values were normalized to the CNRCD_{\max} of iodine at $T_1 = 50$ keV. The behavior of the measured CNRCD_{\max} is the same as the previously described for tungsten. Good agreement is found between simulations and measurements, with a mean deviation of 5.6% and a maximum deviation of 14% for ytterbium at $T_1 = 85$ keV.

For each solution, the maximum measured CNRCD_{\max} can be compared to the CNRCD previously measured in low threshold images at 120 kV. Despite the relative position of the contrast agents remaining the same, an improvement could be measured when using two optimally-combined bin images. For each solution, the improvement is listed in table 4.1 together with the value of T_1 which maximized CNRCD_{\max} .

Material decomposition

In Figure 4.15, the results of the material decomposition of the measurements with two energy thresholds are shown. The lower threshold T_0 was fixed at 20 keV, whereas the higher threshold T_1 was varied. For each value of the T_1 , the two bin images were decomposed in soft tissue and each individual high-Z element. Then, the CNRCD was evaluated in the material map of the specific high-Z element and plotted as a function of higher thresholds T_1 . The values were normalized to the CNRCD of iodine at $T_0 = 50$ keV.

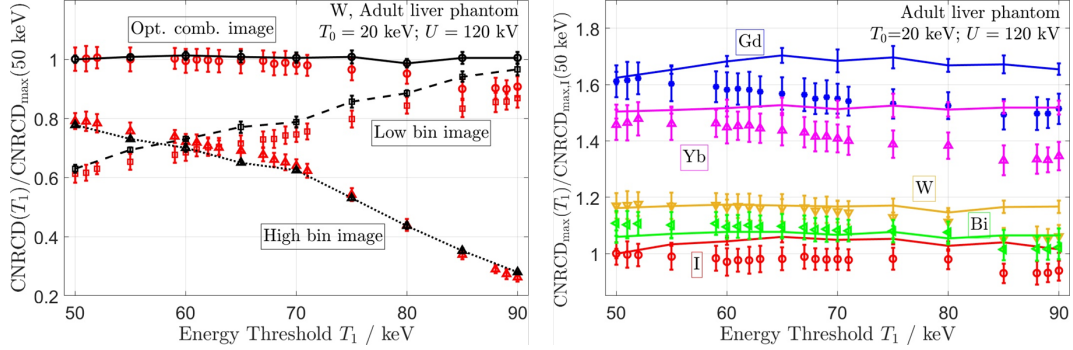


Figure 4.14: Left: for measurements and simulations, the CNRCD of the tungsten solution is plotted as function of the high energy-threshold (T_1). The CNRCD was evaluated in the low and high bin images, and $\text{CNRCD}_{\text{max}}$ was evaluated in the optimally combined image. Values were normalized to the $\text{CNRCD}_{\text{max}}$ at $T_1 = 50$ keV. Right: for the five high-Z solutions, the $\text{CNRCD}_{\text{max}}$ is plotted as function of the T_1 for measurements and simulations. Values were normalized to the $\text{CNRCD}_{\text{max}}$ of iodine at $T_1 = 50$ keV. Measurements are displayed with discrete markers, whereas simulations are displayed with continuous lines.

Table 4.1: For each high-Z element, the CNRCD improvement obtained by using two optimally combined bin images compared to one low threshold image. In both cases, T_0 was 20 keV and the tube voltage was 120 kV.

Element	Improvement	T_1
I	$(5.8 \pm 7.7)\%$	50 keV
Gd	$(8.3 \pm 7.2)\%$	52 keV
Yb	$(9.4 \pm 8.2)\%$	52 keV
W	$(8.4 \pm 7.6)\%$	52 keV
Bi	$(6.6 \pm 7.8)\%$	50 keV

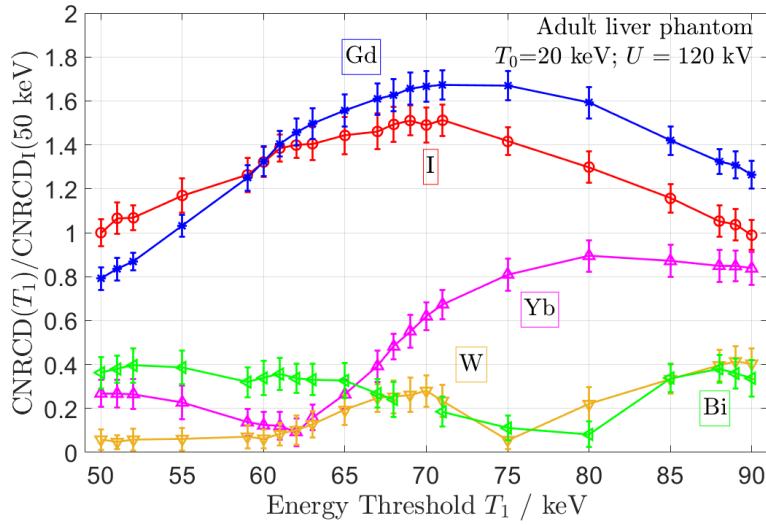


Figure 4.15: For the adult liver phantom, the CNRCD of the material decomposition of each high-Z element as function of the high energy threshold (T_1). The values are normalized for the value of iodine at $T_1=50$ keV.

Unlike the results showed in Figure 4.14, the CNRCD measured in the material decomposition maps is highly dependent on the value of T_1 . The CNRCD of iodine increases for increasing values of T_1 , up to a value of 1.51 for $T_1=70$ keV, then it decreases. The highest CNRCD is provided by gadolinium and it measures 1.67 at $T_1=71$ keV. The material map of gadolinium at its maximum CNRCD is shown in Figure 4.16 left. As it can be seen, in the material map of gadolinium, also contributions by the iodine and the bone can be found. The same contributions are found in the iodine and ytterbium material maps at their maximum CNRCD. The heavier elements like tungsten and bismuth have a local CNRCD maximum when T_1 is around their K-edge (70 keV for tungsten and 90 keV for bismuth). The value of the maxima found at the K-edge is lower than the maxima of iodine and gadolinium, but the corresponding material decompositions do not exhibit contribution by bone. In Figure 4.16, the material decomposition of bismuth for $T_1=88$ keV is displayed: despite the noise being higher than the material map of the gadolinium, no contribution by other high-Z elements nor bone is visible, and thus strongly suppressed.

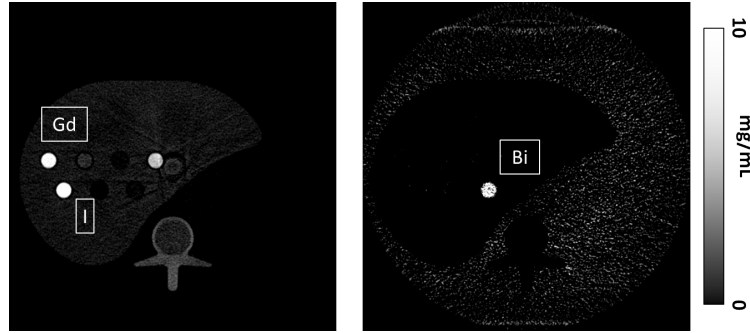


Figure 4.16: Left: material map of the gadolinium for $T_1=71$ keV. The map contains contributions of other high-Z elements and bone. Right: material map of bismuth for $T_1=88$ keV. Since the K-edge of bismuth is exploited, the material map contains only contributions by bismuth.

4.2.2 Simulations

The first set of simulations (described in section 3.3.3) was performed with five realistic high-Z element solutions and has been already presented together with measurements in section 4.2.1. The second set of simulations was performed with seven ideal high-Z element water solutions and it is presented in the following for the three different patient sizes and the two sets of prefiltrations.

i.) Infant Patient Phantom

In figure 4.17 the CNRCD of the seven solutions is shown for the infant size phantom with and without additional Sn filtration. The CNRCD values were normalized to the value of iodine at $U_{\text{ref}} = 80$ kV without Sn filter. The dose reduction was also calculated (Equation (3.15)) and plotted.

When using no Sn filtration, gadolinium and cerium outperformed iodine at all tube voltages, except for gadolinium at 70 kV. The highest dose reduction for $U \geq U_{\text{ref}}$ is $27 \pm 2\%$ with cerium at 80 kV, followed by gadolinium ($17 \pm 4\%$) at a tube voltage between 80 and 90 kV.

When using the additional Sn prefiltration, the CNRCD of iodine and cerium decreases, whereas the maximum CNRCD of gadolinium, ytterbium and tungsten increases. The highest dose reduction ($30 \pm 4\%$) is seen for gadolinium at 80 kV.

ii.) Adult Patient Phantom

In figure 4.18, the results for the adult phantom simulated with and without Sn prefiltration are shown. For this phantom size, the reference value is iodine at $U_{\text{ref}} = 100$ kV without Sn filter.

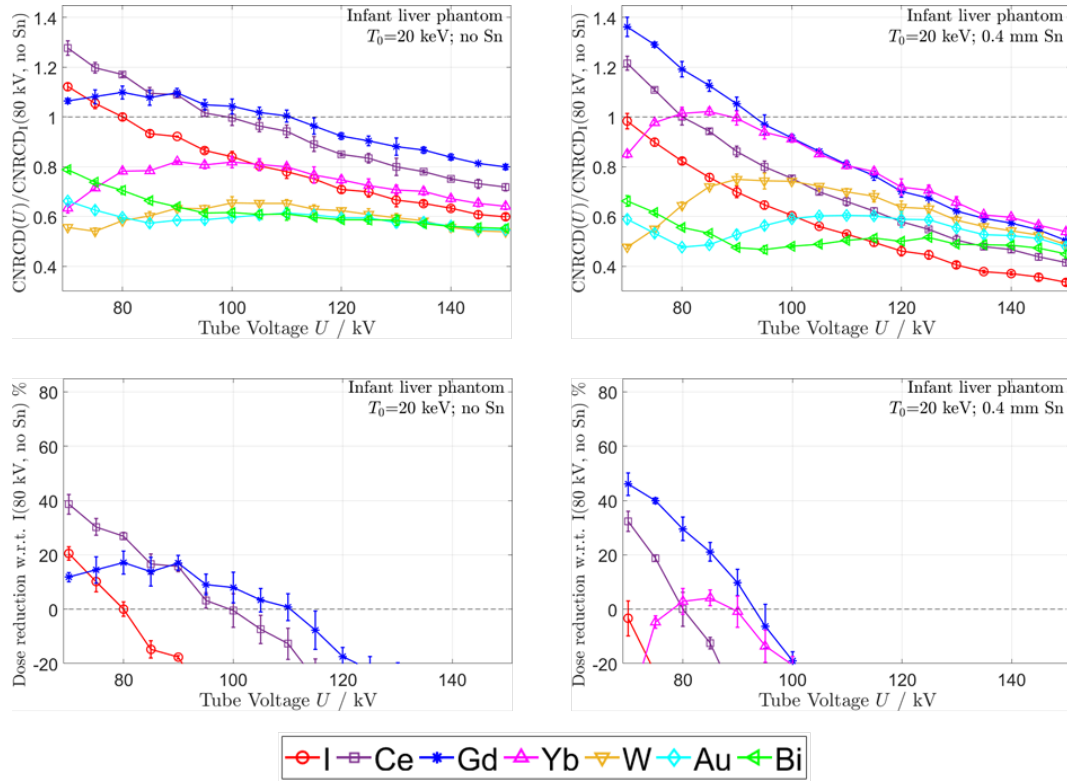


Figure 4.17: For the simulations of an infant patient ($15 \text{ cm} \times 10 \text{ cm}$), the relative CNRCD in the low threshold image ($T_0 = 20$ keV) (top row) and the dose reduction (bottom row) of the different high- Z solutions are shown as a function of the tube voltage. In the right column, the additional Sn filter was deployed. Results are normalized to the value of iodine at 80 kV with no Sn filter.

Without Sn filtration, iodine is outperformed by cerium, gadolinium, and ytterbium for tube voltages higher than U_{ref} . Gadolinium at 100 kV provides the highest dose reduction ($48 \pm 1\%$). Cerium and ytterbium provide approximately the same dose reduction of $30 \pm 2\%$ at 100 kV.

With the Sn filter, the CNRCD of iodine and cerium decreases. Also, the CNRCD of gadolinium decreases for tube voltages $\geq U_{\text{ref}}$, reaching a maximum dose reduction of $44 \pm 1\%$ at 100 kV. The maximum dose reduction is provided by ytterbium ($49 \pm 1\%$) at 100 kV. When using the Sn filter, also heavier elements provide a positive dose reduction: tungsten at 100 kV has a maximum of $33 \pm 1\%$ and the gold at 115 kV has a maximum of $5 \pm 2\%$.

4.2. POTENTIAL OF HIGH-Z ELEMENTS FOR CLINICAL CT

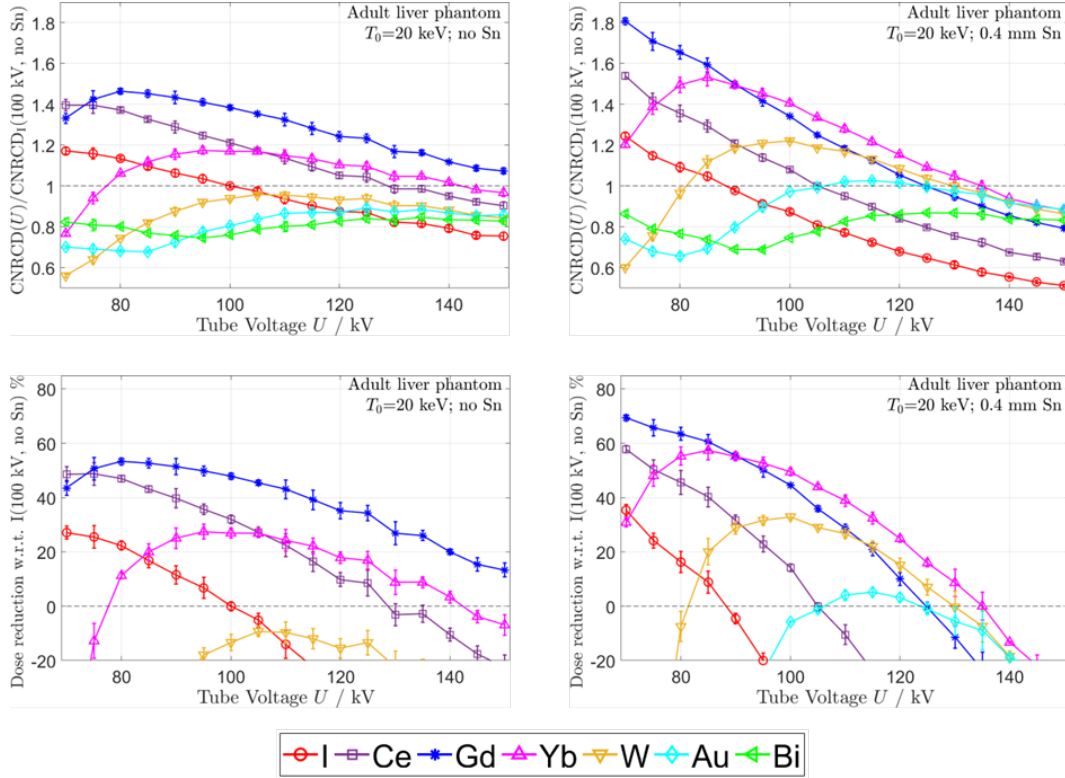


Figure 4.18: For the simulations of an adult patient ($35 \text{ cm} \times 25 \text{ cm}$), the relative CNRCD in the low threshold image ($T_0 = 20$ keV) (top row) and the dose reductions (bottom row) of the different high-Z solutions are shown as a function of the tube voltage. In the right column, an additional Sn filter was deployed. Results are normalized to the value of iodine at 100 kV with no Sn filter.

iii.) Obese Patient Phantom

In figure 4.19, the results of simulations are shown for an obese-sized phantom, with and without additional Sn prefiltration. The CNRCD values of the different high-Z solutions were normalized to the value of iodine at 120 kV with no Sn filter.

When using no additional Sn filter, iodine is outperformed by all the heavier elements for tube voltages higher than U_{ref} . The highest dose reduction ($53 \pm 2\%$) is provided by gadolinium (closely followed by ytterbium) at 120 kV.

With the Sn filtration, the CNRCD of elements lighter than ytterbium decreases, whereas ytterbium and tungsten provide the best performance and a dose reduction of approximately $52 \pm 3\%$ with a tube voltage of 120 kV. Also maximum CNRCD of gold and bismuth increase.

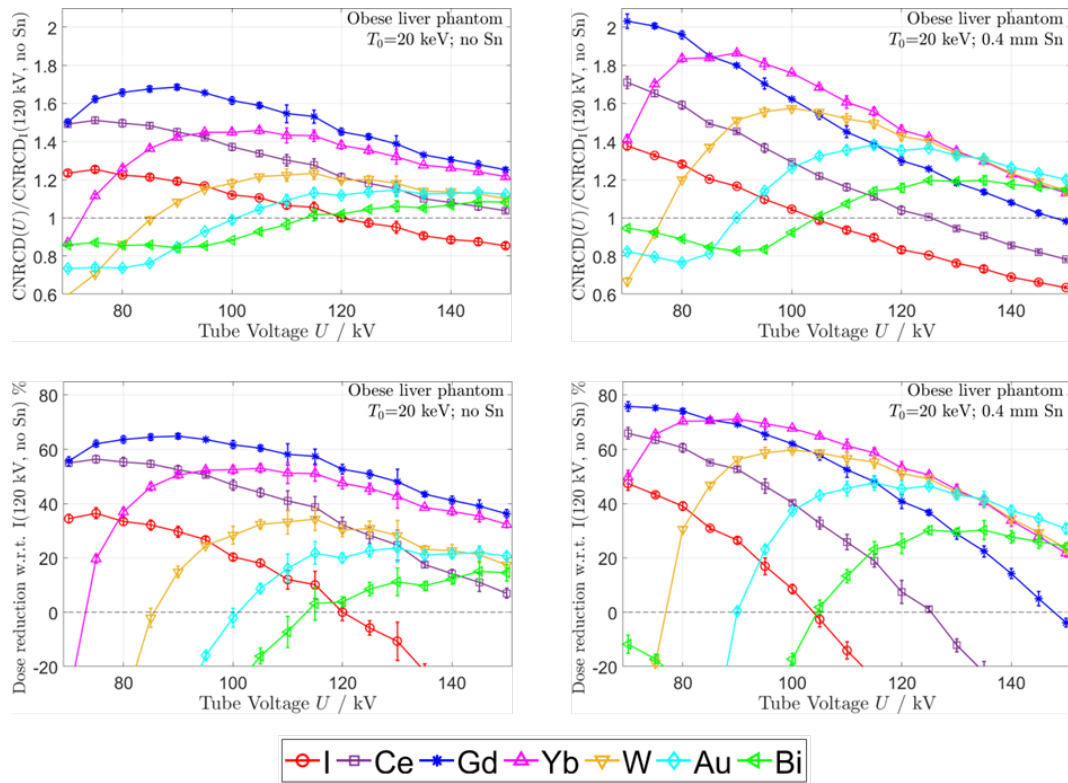


Figure 4.19: For the simulations of an obese patient ($50 \text{ cm} \times 40 \text{ cm}$), the relative CNRCD in the low threshold image ($T_0 = 20$ keV) (top row) and the dose reductions (bottom row) of the different high-Z solutions are shown as a function of the tube voltage. In the right column, an additional Sn filter was deployed. Results are normalized to the value of iodine at 120 kV without Sn filter.

5 | Discussion

5.1 A Novel Contrast Agent for Preclinical Imaging

The novel bismuth-based agent developed by NanoPET Pharma GmbH (Berlin, Germany) was tested on four healthy black mice. The biodistribution of the agent in the mice was monitored over 5 h and time-enhancement curves were generated for the vasculature and the main abdominal organs. The mice tolerated the bismuth agent and quickly recovered from the anesthesia after each measurement. Right after the injection of the agent, the CT-value of the vasculature was measured to be 1200 ± 200 HU, whereas the soft tissue baseline was 100 ± 50 HU. As expected for a nanoparticle-based agent, the agent is slowly cleared from the vasculature by means of the spleen and of the liver, which after 5 h reach a CT-value of 1940 ± 220 HU and 1060 ± 100 HU, respectively. At the end of the experiments, a CT-value of approximately 500 HU was still measured in the vasculature, suggesting that the clearance process was not yet completed and therefore a higher CT-value in the spleen and in the liver has to be expected once all the agent is cleared from the vasculature. The half-life of the agent in the vasculature was estimated to be 250 minutes. The long circulation time of the agent may be exploited for the detection of “leaky” tumors (K. B. Ghaghada et al. 2011). Such tumors have vessels with large pores in the endothelial which can be transverse by the agent nanoparticles, resulting in a contrast enhancement of the tumor tissue (Badea et al. 2019).

A very interesting finding of this study was the detection of contrast enhancement in the intestinal walls. After the injection of the agent, the intestinal walls uptake the agent and reached a CT-value of 530 ± 80 HU at the end of the experiment. As for the liver and the spleen, the slope of the time-enhancement curves suggests that a higher CT-value may be measured once the clearance process is completed. No other examples of CT contrast agents accumulating in the intestine could be found in the literature. The peculiar behavior of the agent is probably due to the nanoparticle coating, which is property of NanoPET Pharma. The enhancement

of the intestinal walls may have multiple applications in diagnostic imaging as the detection of polyps or cancer colon. Another possible application could be the detection of intestinal ischemia, where sections of the intestine may remain unenhanced because of the reduction of blood flow.

5.1.1 Comparison with Iodinated Contrast Agent

A comparison between the novel bismuth-based agent and state-of-art iodinated agents can be done using the measurements performed within this study. An estimation of the vasculature enhancement provided by the iodine agent can be obtained from the measurements of the multi contrast agent protocol, 15 minutes after the injection of 100 μL of the Exitron Myoc (iodine-based). The enhancement measured in the vena cava is 426 ± 21 HU. The estimation for the bismuth enhancement was obtained by measuring one of the mice for the characterization of the novel agent. In order to have comparable results, the mouse injected with 125 μL of bismuth agent was scanned 15 minutes after the injection using the same acquisition settings of the multi contrast agent protocol. The enhancement measured in the vena cava for the bismuth agent had to be proportionally scaled according to the used volume, resulting in an enhancement of 800 ± 23 HU per 100 μL . According to the measurement, the bismuth agent provides 87% more contrast than the iodine contrast agent at the same concentration and at the same injected volume. This can be explained by considering the used tube voltage and the half-life of the two agents. The measurements were performed with a tube voltage of 60 kV without prefiltration. The deployed spectrum can be simulated using the tools described in Section 3.3.3 for a transmission tube. The resulting spectrum has a center of mass around 28 keV, which is lower than the K-edge of iodine. As it can be seen in Figure 5.1, at energies lower than the iodine

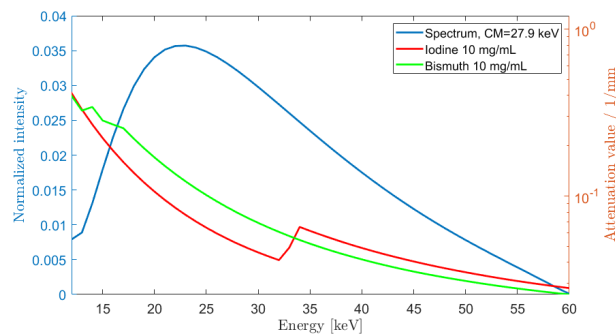


Figure 5.1: Attenuation coefficients of iodine and bismuth at the same concentration.

K-edge the attenuation coefficient of bismuth is higher than the one of iodine. Another factor to consider is that the half-life of the Exitron Myoc (120 minutes) is considerably shorter than the one of the bismuth agent (250 minutes). This means that in the 15 minutes between the injection and the measurement the deployed iodine agent is cleared from the vasculature at a higher rate than the bismuth agent.

5.1.2 Multi Contrast Agent Protocol

The proposed multi contrast agent protocol was successfully tested in-vivo on one healthy BL6 mouse. The Exitron Myoc iodine-based agent was used to enhance the brown adipose tissue and the myocardium, whereas the novel bismuth agent was used to simultaneously enhance the vasculature. The iodine accumulated in the myocardium could be decomposed despite the low concentration (0.7 mg/mL). Nonetheless, the narrow windowing settings required for its visualization highlighted also some ring artifacts at the center of the image. Such artifacts are located in correspondence of the main intermodule gap of the detector (7 pixels), which was herein inpainted using linear interpolation. A possible strategy to mitigate the artifact is to use more advanced inpainting algorithms (exemplar or neural network-based (Eulig et al. 2018)) or to use ring artifact correction methods (Feng et al. 2021). Furthermore, the visualization of the myocardium will benefit cardiac gating and motion compensation. This will also highly improve the potential of the proposed protocol, especially concerning myocardium infarct imaging. In fact, as it has been shown by Sawall et al. 2017, the Exitron Myoc iodine agent does not accumulate in the collagenous scar of the myocardium infarcted tissue, which will therefore remain unenhanced. At the same time, if cardiac motion compensation is applied, the bismuth agent can be used for coronary artery imaging (Sawall et al. 2020a). This will enable the simultaneous visualization of the infarcted tissue and of the myocardium vascularization, resulting in a better characterization of the disease.

The potential of material decomposition is especially highlighted in the scenarios where two enhanced features exhibit similar CT-values. An example of this scenario can be found in daily clinical practice in the detection of calcified plaques. Such highly attenuating features can have the same CT-value of the contrast-enhanced vasculature and can therefore remain undetected. Another example is clearly displayed by Figure 5.2, where an axial slice of the mouse injected with the multi contrast agent protocol is shown. The image is acquired after the injection of the second agent, therefore both the brown adipose tissue and the vasculature are enhanced. As it is possible to see, it is extremely difficult to discern the two features in the CT image (left). If the spectral information is exploited

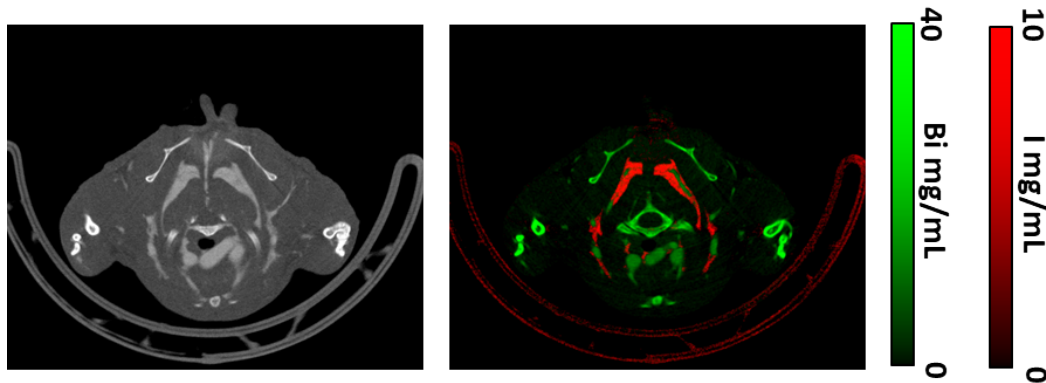


Figure 5.2: Axial slice of the shoulders of the mouse injected with the multi contrast agent protocol. Right: CT image. The tissues enhanced by the iodine and the bismuth agents exhibit the same CT-value. Left: material decomposition. The different tissues are decomposed as different materials and can be discerned.

and the material decomposition is performed, the brown adipose tissue is now clearly visible in the iodine map whereas the vasculature is decomposed as bismuth.

The proposed protocol can be further improved by thoroughly exploiting the characteristic of the novel bismuth agent. In fact, the half-life of the agent is 250 minutes, which is longer than the time needed by the Exitron Myoc to accumulate in the myocardium (3 h). Therefore, the two contrast agents may be simultaneously injected at the beginning of the experiment and then a single CT acquisition can be performed 3 h after the injection. The maximum allowed volume for intravenous injection is 125 μL (for an average 25 g mouse) and therefore it must be shared between the two contrast agents. Since it has been proven that the Exitron Myoc provides sufficient contrast enhancement in the myocardium with only 50 μL (Sawall et al. 2017), the remaining 75 μL can be used for the bismuth injection. Using the results achieved in Section 4.1.1, it can be estimated that 3 h after the injection of 75 μL of bismuth agent, the vasculature will have a CT-value of approximately 460 HU, which will be enough for a clear visualization of the vasculature. An example of the vasculature at ~ 500 HU is visible in Figure 4.5.

Finally, the novel bismuth agent can be exploited to design further multi contrast agent protocols. These may involve more than one additional contrast agent or different injection protocols. For example, a protocol (Figure 5.3) for abdominal imaging can be designed by exploiting the late phase of the bismuth agent and the early phase of another agent (e.g. iodine blood-pool) for the enhancement

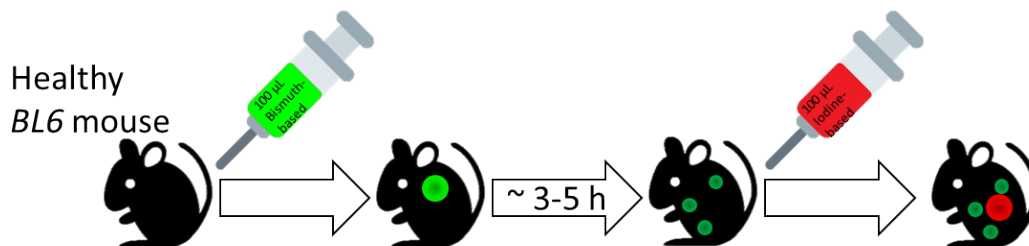


Figure 5.3: Multi contrast agent protocol for abdominal imaging. The bismuth-based agent is injected first. After 3-5 h, the bismuth agent is cleared from the vasculature and it accumulates in intestinal walls. Then, to enhance the vasculature in the abdomen, an iodine-based agent is injected.

of the vasculature. This will enable the simultaneous imaging of the vasculature, liver, spleen, and especially of the intestinal walls.

5.2 Potential of High-Z Elements for Clinical CT

The measurements of the adult liver phantom with a fixed low energy threshold ($T_0=20$ keV) have shown how the contrast enhancement provided by elements with K-edges at different energies is dependent on the tube voltage. In this scenario, gadolinium outperformed all the other investigated high-Z elements for all the tube voltages. The second set of measurements was performed with a fixed tube voltage (120 kV) and two energy thresholds (T_0 fixed at 20 keV and T_1 varied between 50 and 90 keV), and the two bin images were combined to maximize the CNRCD. In this scenario, the CNRCD_{\max} of each element exhibited a wide flat maximum for T_1 between 50 keV and 70 keV, indicating that a fine threshold optimization can not significantly increase the CNRCD. As a rule of thumb, T_1 could be fixed to 50 keV independently of the high-Z element. This effect was already described for iodine in Sawall et al. 2019. For each element, the CNRCD_{\max} measured with two energy thresholds was higher than the one measured with only one energy threshold for the same tube voltage. The values herein found are compatible with the ones obtained for iodine by Sawall et al. 2020b for the same phantom size and tube voltage. The material decomposition performed on the same set of two bin images showed how also in this scenario gadolinium outperforms all the other investigated elements. Nonetheless, the material decomposition map of gadolinium contained also contributions by iodine and bone. For elements with K-edge at higher energies, the material decomposition had a significantly lower CNRCD, but it showed only contributions by the specific element, without interference from other highly attenuating materials. This suggests that, despite

5.2. POTENTIAL OF HIGH-Z ELEMENTS FOR CLINICAL CT

Table 5.1: For each patient size, prefilter setting and high-Z solution, the maximum CNRCD in the simulated low threshold image ($T_0 = 20$ keV). The values are normalized to the CNRCD of iodine at U_{ref} without Sn filter. The tube voltage correspondent to the maximum is listed as well. For each scenario, the maximum CNRCD was highlighted in bold.

High-Z element	Infant 15 cm \times 10 cm $U_{\text{ref}} = 80$ kV		Adult 35 cm \times 25 cm $U_{\text{ref}} = 100$ kV		Obese 50 cm \times 40 cm $U_{\text{ref}} = 120$ kV	
	no Sn	0.4 mm Sn	no Sn	0.4 mm Sn	no Sn	0.4 mm Sn
I	1.00 80 kV	0.82 80 kV	1.00 100 kV	0.87 100 kV	1.0 120 kV	0.83 120 kV
Ce	1.17 80 kV	1.00 80 kV	1.21 100 kV	1.08 100 kV	1.21 120 kV	1.04 120 kV
Gd	1.10 80 kV	1.19 80 kV	1.39 100 kV	1.34 100 kV	1.45 120 kV	1.30 120 kV
Yb	0.82 90 kV	1.02 85 kV	1.17 100 kV	1.41 100 kV	1.38 120 kV	1.46 120 kV
W	0.65 100 kV	0.75 90 kV	0.96 105 kV	1.22 100 kV	1.20 125 kV	1.43 120 kV
Au	0.62 110 kV	0.60 110 kV	0.89 125 kV	1.03 115 kV	1.16 130 kV	1.37 125 kV
Bi	0.71 80 kV	0.57 80 kV	0.85 135 kV	0.87 125 kV	1.09 145 kV	1.20 135 kV

providing less contrast enhancement in the CT-images, the heavier elements like tungsten and bismuth could be a more suitable choice when a clear decomposition of the contrast agent from bone is essential (e.g. calcified plaques detection). Good agreement was found between the measurements and the simulations for all high-Z elements. The maximum measured deviations were found for the two bins experiment for $T_1 > 70$ keV. This is probably due to the simulated spectral response does not reproduce accurately the real spectral response in the whole interval of investigated energies.

After being validated with the measurements, the simulations were used to investigate CNRCDs and dose reductions in different scenarios. A set of seven ideal high-Z solutions (I, Ce, Gd, Yb, W, Au, and Bi) in water was used to avoid contrast-enhancement due to the solvent or molecular structure of the contrast agent. The maximum CNRCDs relative to iodine are listed in Table 5.1 for the different high-Z elements in the different scenarios. The elements providing the highest CNRCD are highlighted in Table 5.1 for each scenario

Table 5.2: For the investigated cases with simulations, the maximum dose reductions for tube voltages $\geq U_{\text{ref}}$ are listed.

	Infant		Adult		Obese	
	$U_{\text{ref}} = 80 \text{ kV}$		$U_{\text{ref}} = 100 \text{ kV}$		$U_{\text{ref}} = 120 \text{ kV}$	
Sn filter	None	0.4 mm	None	0.4 mm	None	0.4 mm
Max dose reduction	$27 \pm 2\%$	$30 \pm 4\%$	$48 \pm 1\%$	$49 \pm 1\%$	$53 \pm 2\%$	$53 \pm 2\%$
Element	Ce	Gd	Gd	Yb	Gd	Yb
Tube voltage	80 kV	80 kV	100 kV	100 kV	120 kV	120 kV

and the corresponding dose reductions are summarized in Table 5.2. A result common to all the patient sizes is that the maximum CNRCD is achieved at a tube voltage equal to U_{ref} . This is due to the general tendency of the CNRCD to decrease with increasing tube voltage. Furthermore, as explained in Section 3.3.4, only improvements for $U > U_{\text{ref}}$ were considered. For the adult and obese patient size, a potential dose reductions around 50% can be achieved by using gadolinium instead of iodine at the same concentration. For the infant patient size, a $27 \pm 2\%$ dose reduction was achieved using cerium. As it can be seen in figures 4.17 to 4.19, further dose reductions can be achieved in all scenarios if tube voltages below U_{ref} are considered. The examination of obese patients is the most challenging concerning an adequate tube current time product. However for these patients, the maximum dose reduction with $U < U_{\text{ref}}$ is $65 \pm 1\%$ (gadolinium at 90 kV without Sn filter), which is only slightly better than the $53 \pm 2\%$ dose reduction already found for gadolinium at 120 kV without Sn filter.

As shown in table 4.1, further increases of the CNRCD and consequent dose reductions can be achieved by using two optimally-combined bin images instead of only one threshold image. Despite improvements being measured for all the considered elements, some specific elements benefit more than others from this effect. From table 4.1, it can be seen how the ytterbium CNRCD increases by 9.5%, whereas for iodine the improvement is only 5.8%.

Gadolinium resulted to be the most promising high-Z element for contrast-enhanced CT among all the investigated elements: it could provide around 50% dose-reduction for adult and obese patients, and up to 30% for infant patients if used in combination with a 0.4 mm Sn filter. Unlike the other high-Z elements, the implementation of gadolinium as a CT contrast agent should be facilitated since it is a well-established contrast agent for magnetic resonance imaging. However, it has to be stressed that the gadolinium-based contrast agents which are currently available in clinics have a concentration significantly lower than the iodine-based contrast agents (see Table 3.3). A simplistic increase of the gadolinium con-

centration is not the solution since gadolinium-based contrast agents are being investigated for their potential toxicity for the human neurons (Pasquini et al. 2018; Bower et al. 2019). Nonetheless, nanoparticle contrast agents based on gadolinium have been already studied for applications in magnetic resonance (K. Ghaghada et al. 2008; Sitharaman et al. 2005) and micro-CT (Badea et al. 2019).

Besides contrast-enhancement and biocompatibility, also K-edge imaging and material decomposition performance must be taken into account when evaluating high-Z elements as potential CT contrast agents. Unlike iodine, the heavier elements have K-edges at energies where photons are still transmitted through the patient. This can be nicely exploited in combination with the adjustable thresholds of PC detectors to generate bone-free material maps of the contrast agent, as it was shown by the decomposition of bismuth in Figure 4.16. Another application is the decomposition of multiple contrast agents at the same time, as done in preclinical settings in Section 4.1.

5.2.1 Comparison with EI detectors

The findings of this work can be compared to the ones found by Nowak et al. 2011 for a similar investigation with an EI detector. One of the main differences is that the CNRCD of the different elements decreases more rapidly for the EI detector than for the PC detector as the tube voltage increases. For example, when increasing the tube voltage from 80 kV to 140 kV for the adult phantom size, the iodine CNRCD decreases by 31% for the PC detector, whereas for the EI detector the decrease is 44%. This can be explained by considering that the spectrum detected by the EI detector is weighted by the photon energy, and therefore it becomes harder than the one detected by the PC detector as the tube voltage increases. In figure 5.4 left the detected spectra (through a 32 cm water phantom) are plotted for both detectors. The EI detector was simulated as a Gd_2O_3S layer 1.4 mm thick. The PC detector was simulated as described in section 3.3.3 at 80 and 140 kV. As it can be seen, for a tube voltage of 80 kV the centers of mass of the two spectra are approximately the same, whereas at 140 kV the center of mass of the EI spectrum is 9% higher than the PC's one. In the interval of energies relevant for CT imaging, the attenuation coefficient of matter without K-edge decreases with increasing energies. Therefore the contrast measured by the EI detector will be lower than for the PC detector.

Another difference between the two investigations is that in each scenario the maximum dose reduction for the EI detector is achieved by an element slightly heavier than for the PC detector. For each scenario and detector, the atomic

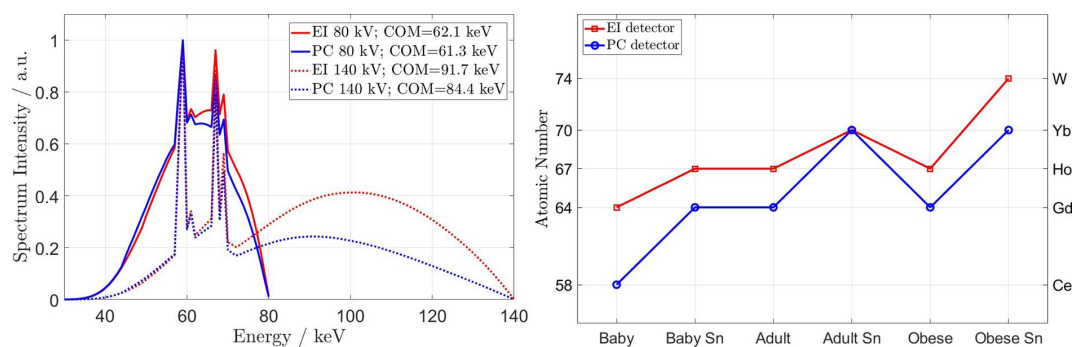


Figure 5.4: Left: For EI and PC detectors, the detected spectra through 32 cm of water are shown for tube voltages of 80 and 140 kV. The center of mass (COM) is evaluated for each spectrum. Right: For each investigated scenario, the high-Z elements which maximized the dose reduction are displaced for EI (Nowak et al. 2011) and PC detectors.

number of the element providing the highest dose reduction is shown in figure 5.4 right. As discussed before, the spectrum detected by an EI detector has a higher center of mass than that of a PC detector and therefore the maximum CNRCD for EI detector is reached by elements with a K-edge at slightly higher energy compared to PC detector.

6 | Summary

Recently, two innovations are being investigated for clinical CT applications: nanoparticle-based contrast agents and photon-counting (PC) detectors. Nanoparticles can be used to densely pack a highly attenuating element different than iodine and an engineered coating can be applied to the nanoparticles to create targeted agents and to enhance the biocompatibility of the contained high-Z element. This is particularly of interest for clinical applications since it may allow to exploit the physical properties of elements heavier than iodine, which, at the moment, is the only element allowed for intravenous injection for CT imaging. The PC detectors originally developed at CERN for particle tracking are being investigated for CT applications, and whole body PC scanners are already commercially available since November 2021. PC detectors have been already proven to provide better performance than conventional energy-integrating (EI) detectors concerning image noise, spatial resolution and iodine quantification. The main feature of the PC detector is the possibility to acquire spectral data thanks to the multiple and adjustable energy thresholds. This feature can be used in combination with high-Z materials which exhibit a K-edge in the energy interval of interest.

In this thesis, the potential of high-Z elements for novel non-iodinated contrast agents was investigated in combination with the novel PC-CT technology. The topic was addressed both at a preclinical and clinical level.

In preclinical imaging, contrast agents based on elements heavier than iodine are already commercially available and new ones are constantly developed. In this frame, a novel contrast agent based on bismuth was herein tested for the first time *in-vivo*. To do so, an experimental gantry equipped with a PC detector was assembled specifically for this application. The gantry geometry was modelled to fulfill the requirements of a micro-CT scanner. The bismuth agent was injected in four healthy black mice, which were then scanned at regular time intervals to quantify the biodistribution of the agent as a function of time. The results showed that right after the injection, the bismuth agent provides a contrast enhancement of about 1200 HU in the vasculature. Then the agent is slowly cleared from the

system with a biological half-life of approximately 250 minutes and accumulates in the liver and in the spleen. Interestingly, the agent also accumulates slowly in the intestinal wall and provides 530 HU of contrast enhancement 5 h after the injection. This specific behavior of the novel agent is probably due to engineered coating applied to the nanoparticles, which is property of the manufacturer. Up to my knowledge, no other example of CT-agents accumulating in the intestinal walls are available in the literature, making the investigated bismuth agent an innovation with many possible application in abdominal diagnostic imaging, like polyps and intestinal ischemia detection or colon cancer imaging. Compared to an iodine-based nanoparticle agent, the bismuth agent provides about 80% more contrast than iodine at the same concentration and has a half-life more then twice longer. Furthermore, a protocol for multi contrast imaging was herein proposed and tested *in-vivo* on one mouse. The results showed that the novel bismuth agent can be used in combination with the Exitron Myoc (iodine-based) for the simultaneous imaging of the myocardium, brown adipose tissue and vasculature.

In a clinical scenario, the potential of high-Z elements for contrast-enhanced PC-CT was thoroughly investigated in a wide variety of scenarios, both with phantom measurements and simulations. For each element, the contrast-to-noise ratio at unit concentration and at unit dose (CNRCU) was compared to the gold standard iodine for different patient sizes (infant, adult and obese), tube voltages (from 70 to 150 kV), filtration settings (with and without 0.4 mm Sn filter) and energy threshold values. Between the investigated elements, gadolinium provided the highest contrast enhancement in most scenarios. Compared to iodine, the usage of gadolinium lead to dose reductions up to 50% for adult and obese patients, and up to 30% for infant patient in combination with a 0.4 mm Sn filter. Since gadolinium is already used as a contrast agent for magnetic resonance imaging, its implementation as a CT contrast agent should be facilitated compared to other high-Z elements. Further dose reductions can be achieved by using two optimally combined bin images. The material decomposition performance of the high-Z elements were quantified using the measurements of the adult liver phantom with two energy thresholds and a tube voltage of 120 kV. The results confirmed again that gadolinium outperforms all the other investigated high-Z elements, but its material map showed contributions from other materials contained in the phantom, especially bone. For other elements with a K-edge at higher energies, like tungsten and bismuth, the CNRCU of the material decomposition resulted up to four times lower than for gadolinium, but no undesired contributions by other materials were present in the material decomposition. This will be particularly of interest for applications like calcified plaque detection, where it is essential to discern between the contrast-enhanced lumen of the vessels and the highly attenuating plaques.

7 | Zusammenfassung

Aktuell werden zwei Neuerungen für klinische CT-Anwendungen untersucht: Kontrastmittel auf Basis von Nanopartikeln und photonenzählenden (PC)-Detektoren. Mit Hilfe von Nanopartikeln lässt sich ein stark absorbierendes Element dicht verpacken und es kann eine synthetisch hergestellte Beschichtung auf die Nanopartikel aufgebracht werden, um maßgeschneiderte Kontrastmittel zu erzeugen und die Biokompatibilität des eingeschlossenen Elements zu gewährleisten. Dies ist insbesondere für klinische Anwendungen von Interesse, da derzeit nur Kontrastmittel auf Basis von Jod für die intravenöse Injektionen in der klinischen CT-Bildgebung zugelassen sind. Die physikalischen Eigenschaften von Elementen mit hoher Kernladungszahl, welche schwerer als Jod sind, könnten allerdings Vorteile bringen. Die ursprünglich am CERN zum Teilchen-Tracking entwickelten PC-Detektoren werden für CT-Anwendungen untersucht. Ganzkörper-PC-Scanner sind bereits kommerziell erhältlich. Es wurde bereits nachgewiesen, dass PC-Detektoren hinsichtlich Bildrauschen, räumlicher Auflösung und Jodquantifizierung eine bessere Leistung als herkömmliche energieintegrierende (EI)-Detektoren bieten. Eines der Hauptmerkmale des PC-Detektors ist die Möglichkeit, Spektraldaten dank mehrerer einstellbarer Energieschwellen zu erfassen. Dieses Merkmal kann in Kombination mit Materialien mit hohem Z verwendet werden, die eine K-Absorptionskante im untersuchten Energieintervall aufweisen, um Bilder zu erzeugen, welche nur einzelne Materialien zeigen (Materialzerlegung).

In dieser Arbeit wurde das Potenzial von schweren Elementen für neuartige nicht auf Jod basierende Kontrastmittel in Kombination mit der neuartigen PC-CT-Technologie untersucht. Das Thema wurde sowohl auf präklinischer als auch auf klinischer Ebene bearbeitet.

In der präklinischen Bildgebung sind Kontrastmittel auf Basis schwererer Elemente als Jod bereits kommerziell erhältlich und werden ständig neu entwickelt. In diesem Rahmen wurde hier erstmals ein neuartiges Kontrastmittel auf Wismutbasis *in-vivo* getestet. Dazu wurde eigens für diese Anwendung eine mit einem PC-Detektor ausgestattete Versuchsgantry aufgebaut. Die Gantry-Geometrie wurde so modelliert, dass sie die Anforderungen eines Micro-CT-Scanners erfüllt. Das Wismut-Kontrastmittel wurde in vier gesunde schwarze Mäuse injiziert, die dann

in regelmäßigen Zeitabständen gescannt wurden, um die metabolische Verteilung des Agents als Funktion der Zeit zu quantifizieren. Die Ergebnisse zeigten, dass das Wismut-Kontrastmittel direkt nach der Injektion eine Kontrastverstärkung von 1200 HU im Gefäßsystem liefert. Anschließend wird es mit einer Halbwertszeit von ca. 250 Minuten langsam aus dem System ausgeschieden und reichert sich in Leber und Milz an. Interessanterweise reichert sich der Wirkstoff auch langsam in der Darmwand an und liefert 5 h nach der Injektion etwa 530 HU Kontrastverstärkung. Dieses spezifische Verhalten ist wahrscheinlich auf eine auf die Nanopartikel aufgebraute synthetische Beschichtung zurückzuführen, die Eigentum des Herstellers ist. Meines Wissens ist kein anderes Beispiel für CT-Kontrastmittel in der Literatur bekannt, welches sich in den Darmwänden anreichert. Daraus ergeben sich viele potenzielle Anwendungen in der diagnostischen Bildgebung des Abdomens mit Wismut-Kontrastmitteln, wie Bildgebung zur Erkennung von Polypen und Darmischämie oder die Bildgebung von Dickdarmkrebs. Im Vergleich zu einem jodbasierten Nanopartikel-Kontrastmittel bietet das wismutbasierte bei gleicher Konzentration etwa 80% mehr Kontrast als Jod und hat eine mehr als doppelt so lange biologische Halbwertszeit. Darüber hinaus wurde hier ein Protokoll für die Multikontrastbildgebung vorgeschlagen und *in-vivo* an einer Maus getestet. Die Ergebnisse zeigten, dass das neuartige Wismut-Kontrastmittel in Kombination mit dem Exitron Myoc (jodbasiert) zur simultanen Bildgebung des Myokardiums, des braunen Fettgewebes und der Gefäße eingesetzt werden kann.

Im klinischen Szenario wurde das Potenzial von schweren Elementen für die kontrastverstärkte PC-CT in einer Vielzahl von Szenarien sowohl mit Phantommessungen als auch mit Simulationen gründlich untersucht. Für jedes Element wurde das Kontrast-Rausch-Verhältnis bei Einheitskonzentration und bei Einheitsdosis (CNRCD) mit dem Goldstandard Jod für verschiedene Patientengrößen (Säuglinge, Erwachsene und Adipositas), Röhrenspannungen (von 70 bis 150 kV), Filtereinstellungen (mit und ohne 0,4 mm Sn-Filter) und Energieschwellen verglichen. Von den untersuchten Elementen lieferte Gadolinium in den meisten Szenarien die höchste Kontrastverstärkung. Im Vergleich zu Jod führte die Verwendung von Gadolinium zu Dosisreduktionen von bis zu 50% bei erwachsenen und adipösen Patienten und bis zu 30% bei Säuglingen in Kombination mit einem 0.4 mm Sn-Filter. Da Gadolinium bereits als Kontrastmittel für die Magnetresonanztomographie verwendet wird, sollte seine Umsetzung als CT-Kontrastmittel im Vergleich zu anderen schweren Elementen einfacher sein. Weitere Dosisreduktionen können durch die Verwendung von zwei optimal kombinierten Bin-Bildern erreicht werden. Die Eignung zur Materialdekomposition der schweren Elemente wurde anhand der Messungen des Erwachsenen-Leberphantoms mit zwei Energieniveaus und einer Röhrenspannung von 120 kV quantifiziert. Die Ergebnisse bestätigten erneut, dass Gadolinium alle anderen untersuchten schweren Elemente übertrifft, aber

Gadolinium-Bilder zeigten Beiträge anderer im Phantom enthaltener Materialien, insbesondere Knochen. Für andere Elemente mit einer K-Kante bei höheren Energien, wie Wolfram und Wismut, war die CNRCD der Materialdekomposition bis zu viermal niedriger als für Gadolinium, aber es waren keine unerwünschten Beiträge anderer Materialien in der Materialzerlegung vorhanden. Dies ist insbesondere für Anwendungen wie die Erkennung von verkalkten Plaques von Interesse, bei denen es wichtig ist, zwischen dem kontrastverstärkten Volumen der Gefäße und den stark abschwächenden Plaques zu unterscheiden.

8 | Reference list

- Alvarez, R. E. and A. Macovski (1976). “Energy-selective reconstructions in X-ray computerised tomography”. In: *Physics in Medicine and Biology* 21.5, pp. 733–744.
- Amato, C., L. Klein, E. Wehrse, L. T. Rotkopf, S. Sawall, J. Maier, C. H. Ziener, H. P. Schlemmer, and M. Kachelrieß (2020). “Potential of contrast agents based on high-Z elements for contrast-enhanced photon-counting computed tomography”. In: *Medical Physics* 47.12, pp. 6179–6190.
- Attix, F. H. (1986). *Introduction to Radiological Physics and Radiation Dosimetry*. Wiley.
- Aydogan, B., J. Li, T. Rajh, A. Chaudhary, S. J. Chmura, C. Pelizzari, C. Wietholt, M. Kurtoglu, and P. Redmond (2010). “AuNP-DG: Deoxyglucose-labeled gold nanoparticles as X-ray computed tomography contrast agents for cancer imaging”. In: *Molecular Imaging and Biology* 12.5, pp. 463–467.
- Badea, C. T., D. P. Clark, M. Holbrook, M. Srivastava, Y. Mowery, and K. B. Ghaghada (2019). “Functional imaging of tumor vasculature using iodine and gadolinium-based nanoparticle contrast agents: A comparison of spectral micro-CT using energy integrating and photon counting detectors”. In: *Physics in Medicine and Biology* 64.6.
- Baer, M. and M. Kachelrieß (2012). “Hybrid scatter correction for CT imaging”. In: *Physics in Medicine and Biology* 57.21, pp. 6849–6867.
- Ballabriga, R., J. Alozy, M. Campbell, E. Frojdh, E. H. Heijne, T. Koenig, X. Llopart, J. Marchal, D. Pennicard, T. Poikela, L. Tlustos, P. Valerio, W. Wong, and M. Zuber (2016). “Review of hybrid pixel detector readout ASICs for spectroscopic X-ray imaging”. In: *Journal of Instrumentation* 11.1.
- Barnes, G. T., D. M. Tucker, and D. P. Chakraborty (1991). “Semiempirical model for generating tungsten target x-ray spectra”. In: *Medical Physics* 18.2, pp. 211–218.
- Beer (1852). “Bestimmung der Absorption des rothen Lichts in farbigen Flüssigkeiten”. In: *Annalen der Physik* 162.5, pp. 78–88.
- Bejarano, J., M. Navarro-Marquez, F. Morales-Zavala, J. O. Morales, I. Garcia-Carvajal, E. Araya-Fuentes, Y. Flores, H. E. Verdejo, P. F. Castro, S. La-

-
- vandero, and M. J. Kogan (2018). “Nanoparticles for diagnosis and therapy of atherosclerosis and myocardial infarction: Evolution toward prospective theranostic approaches”. In: *Theranostics* 8.17, pp. 4710–4732.
- Bhavane, R., C. Badea, K. B. Ghaghada, D. Clark, D. Vela, A. Moturu, A. Annapragada, G. A. Johnson, J. T. Willerson, and A. Annapragada (2013). “Dual-energy computed tomography imaging of atherosclerotic plaques in a mouse model using a liposomal-iodine nanoparticle contrast agent”. In: *Circulation: Cardiovascular Imaging* 6.2, pp. 285–294.
- Bower, D. V., J. K. Richter, H. von Tengg-Kobligk, J. T. Heverhagen, and V. M. Runge (2019). “Gadolinium-Based MRI Contrast Agents Induce Mitochondrial Toxicity and Cell Death in Human Neurons, and Toxicity Increases With Reduced Kinetic Stability of the Agent”. In: *Investigative Radiology* 54.8, pp. 453–463.
- Buzug, T. M. (2008). *Computed tomography*. Springer.
- Clark, D. P. and C. T. Badea (2017). *Hybrid spectral CT reconstruction*. Vol. 12. 7, pp. 1–52.
- Cormack, A. M. (1963). “Representation of a function by its line integrals, with some radiological applications”. In: *Journal of Applied Physics* 34.9, pp. 2722–2727.
- De Santis, D., C. N. De Cecco, U. J. Schoepf, J. W. Nance, R. T. Yamada, B. A. Thomas, K. Otani, B. E. Jacobs, D. A. Turner, J. L. Wichmann, M. Eid, A. Varga-Szemes, D. Caruso, K. L. Grant, B. Schmidt, T. J. Vogl, A. Laghi, and M. H. Albrecht (2019). “Modified calcium subtraction in dual-energy CT angiography of the lower extremity runoff: impact on diagnostic accuracy for stenosis detection”. In: *European Radiology* 29.9, pp. 4783–4793.
- El Ketara, S. and N. L. Ford (2020). “Time-course study of a gold nanoparticle contrast agent for cardiac-gated micro-CT imaging in mice”. In: *Biomedical Physics and Engineering Express* 6.3, p. 35025.
- Eulig, E., J. Maier, A. Hahn, and M. Kachelrieß (2018). “Deep Inpainting for Photon-Counting Cone-Beam CT”. In: *Program of the 105th Scientific Assembly and Annual Meeting of the RSNA*.
- Faby, S., S. Kuchenbecker, S. Sawall, D. Simons, H. P. Schlemmer, M. Lell, and M. Kachelrieß (2015). “Performance of today’s dual energy CT and future multi energy CT in virtual non-contrast imaging and in iodine quantification: A simulation study”. In: *Medical Physics* 42.7, pp. 4349–4366.
- Faby, S., J. Maier, S. Sawall, D. Simons, H. P. Schlemmer, M. Lell, and M. Kachelrieß (2016). “An efficient computational approach to model statistical correlations in photon counting x-ray detectors”. In: *Medical Physics* 43.7, pp. 3645–3960.
- Feldkamp, L. A., L. C. Davis, and J. W. Kress (1984). “Practical cone-beam algorithm”. In: *Journal of the Optical Society of America A* 1.6, p. 612.
-

- Feng, M., X. Ji, R. Zhang, K. Treb, A. M. Dingle, and K. Li (2021). “An experimental method to correct low-frequency concentric artifacts in photon counting CT”. In: *Physics in medicine and biology* 66.17.
- Fitzgerald, P. F., M. D. Butts, J. C. Roberts, R. E. Colborn, A. S. Torres, B. D. Lee, B. M. Yeh, and P. J. Bonitatibus (2016). “A proposed CT contrast agent using carboxybetaine zwitterionic tantalum oxide nanoparticles: Imaging, biological, and physicochemical performance”. In: *Investigative radiology* 51.12, p. 786.
- Ghaghada, K., C. Hawley, K. Kawaji, A. Annapragada, and S. Mukundan (2008). “T1 Relaxivity of Core-encapsulated Gadolinium Liposomal Contrast Agents-Effect of Liposome Size and Internal Gadolinium Concentration”. In: *Academic Radiology* 15.10, pp. 1259–1263.
- Ghaghada, K. B., C. T. Badea, L. Karumbaiah, N. Fettig, R. V. Bellamkonda, G. A. Johnson, and A. Annapragada (2011). “Evaluation of tumor microenvironment in an animal model using a nanoparticle contrast agent in computed tomography imaging”. In: *Academic Radiology* 18.1, pp. 20–30.
- Hounsfield, G. N. (1972). “A method of and apparatus for examination of a body by radiation such as X-or gamma-radiation”. In: *British Patent No. 1,283,915*.
- Hounsfield, G. N. (1973). “Computerized transverse axial scanning (tomography). 1. Description of system”. In: *The British journal of radiology* 46.552, pp. 1016–1022.
- Kalender, W. A., P. Deak, M. Kellermeier, M. van Straten, and S. V. Vollmar (2009). “Application- and patient size-dependent optimization of x-ray spectra for CT”. In: *Medical Physics* 36.3, pp. 993–1007.
- Kappler, S., A. Henning, B. Kreisler, F. Schoeck, K. Stierstorfer, and T. Flohr (2014). “Photon counting CT at elevated X-ray tube currents: contrast stability, image noise and multi-energy performance”. In: *Proceedings of the SPIE Medical Imaging Conference* 9033, p. 90331C.
- Karathanasis, E., L. Chan, L. Karumbaiah, K. McNeeley, C. J. D’Orsi, A. V. Annapragada, I. Sechopoulos, and R. V. Bellamkonda (2009). “Tumor Vascular Permeability to a Nanoprobe Correlates to Tumor-Specific Expression Levels of Angiogenic Markers”. In: *PLOS ONE* 4.6, e5843.
- Klein, L., S. Dorn, C. Amato, S. Heinze, M. Uhrig, H. P. Schlemmer, M. Kachelrieß, and S. Sawall (2020). “Effects of Detector Sampling on Noise Reduction in Clinical Photon-Counting Whole-Body Computed Tomography”. In: *Investigative Radiology* 55.2, pp. 111–119.
- Knoll, G. (2000). *Radiation detection and measurement*. Third Edit. New York: John, Wiley & Sons.
- Lambert, J. H. (1760). *Photometria, sive de mensura et gradibus luminis, colorum et umbrae*. Eberhard Klett.

-
- Lell, M. and M. Kachelrieß (2020). “Recent and upcoming technological developments in computed tomography: High speed, low dose, deep learning, multienergy”. In: *Investigative Radiology* 55.1, pp. 8–19.
- Li, X., N. Anton, G. Zuber, and T. Vandamme (2014). “Contrast agents for preclinical targeted X-ray imaging”. In: *Advanced drug delivery reviews* 76.1, pp. 116–133.
- Liu, X., L. Yu, A. N. Primak, and C. H. McCollough (2009). “Quantitative imaging of element composition and mass fraction using dual-energy CT: Three-material decomposition”. In: *Medical Physics* 36.5, pp. 1602–1609.
- Lusic, H. and M. W. Grinstaff (2013). “X-ray-computed tomography contrast agents”. In: *Chemical Reviews* 113.3, pp. 1641–1666.
- Mannil, M., T. Hickethier, J. Von Spiczak, M. Baer, A. Henning, M. Hertel, B. Schmidt, T. Flohr, D. Maintz, and H. Alkadhi (2018). “Photon-Counting CT: High-Resolution Imaging of Coronary Stents”. In: *Investigative Radiology* 53.3, pp. 143–149.
- Meng, Y., H. Gong, and X. Yang (2013). “Online geometric calibration of cone-beam computed tomography for arbitrary imaging objects”. In: *IEEE Transactions on Medical Imaging* 32.2, pp. 278–288.
- Moghiseh, M., C. Lowe, J. G. Lewis, D. Kumar, A. Butler, N. Anderson, A. Raja, and A. Bombonati (2018). “Spectral Photon-Counting Molecular Imaging for Quantification of Monoclonal Antibody-Conjugated Gold Nanoparticles Targeted to Lymphoma and Breast Cancer: An in Vitro Study”. In: *Contrast Media and Molecular Imaging* 2018.
- Nilsson, H. E., E. Dubari, M. Hjelm, and K. Bertilsson (2002). “Simulation of photon and charge transport in X-ray imaging semiconductor sensors”. In: *Nuclear Instruments and Methods in Physics Research, Section A: Accelerators, Spectrometers, Detectors and Associated Equipment* 487.1-2, pp. 151–162.
- Nowak, T., M. Hupfer, R. Brauweiler, F. Eisa, and W. A. Kalender (2011). “Potential of high-Z contrast agents in clinical contrast-enhanced computed tomography”. In: *Medical Physics* 38.12, pp. 6469–6482.
- Pasquini, L., A. Napolitano, E. Visconti, D. Longo, A. Romano, P. Tomà, and M. C. R. Espagnet (2018). *Gadolinium-Based Contrast Agent-Related Toxicities*.
- Popovtzer, R., A. Agrawal, N. A. Kotov, A. Popovtzer, J. Balter, T. E. Carey, and R. Kopelman (2008). “Targeted gold nanoparticles enable molecular CT imaging of cancer”. In: *Nano Letters* 8.12, pp. 4593–4596.
- Rabin, O., J. M. Perez, J. Grimm, G. Wojtkiewicz, and R. Weissleder (2006). “An X-ray computed tomography imaging agent based on long-circulating bismuth sulphide nanoparticles”. In: *Nature Materials* 5.2, pp. 118–122.
- Radon, J. (1971). “Über die Bestimmung von Funktionen durch ihre Integralwerte längs gewisser Mannigfaltigkeiten”. In: *Berichte über die Verhandlungen der*
-

-
- Königlich-Sächsischen Akademie der Wissenschaften zu Leipzig* 69, pp. 262–277.
- Ramachandran, G. and A. Lakshminarayanan (1971). “Three-dimensional reconstruction from radiographs and electron micrographs: application of convolutions instead of Fourier transforms”. In: *Proceedings of the National Academy of Sciences of the United States of America* 68.9, pp. 2236–2240.
- Ren, L., K. Rajendran, J. G. Fletcher, C. H. McCollough, and L. Yu (2020). “Simultaneous Dual-Contrast Imaging of Small Bowel With Iodine and Bismuth Using Photon-Counting-Detector Computed Tomography”. In: *Investigative Radiology* Publish Ah.10, pp. 688–694.
- Roessl, E. and R. Proksa (2007). “K-edge imaging in x-ray computed tomography using multi-bin photon counting detectors”. In: *Physics in Medicine and Biology* 52.15, pp. 4679–4696.
- Roessler, A. C., M. Hupfer, D. Kolditz, G. Jost, H. Pietsch, and W. A. Kalender (2016). “High Atomic Number Contrast Media Offer Potential for Radiation Dose Reduction in Contrast-Enhanced Computed Tomography”. In: *Investigative Radiology* 51.4, pp. 249–254.
- Röntgen, W. C. (1898). “Ueber eine neue Art von Strahlen”. In: *Annalen der Physik* 300.1, pp. 12–17.
- Sawall, S., S. Dorn, J. Maier, L. Klein, S. Faby, M. Uhrig, H. Schlemmer, and M. Kachelrieß (2019). “Patienten-adaptierte Schwellwertstellungen für optimalen Jodkontrast in einem photonenzählenden Ganzkörper-CT”. In: *Deutscher Röntgenkongress*.
- Sawall, S., C. Amato, L. Klein, E. Wehrse, J. Maier, and M. Kachelrieß (2021). “Toward molecular imaging using spectral photon-counting computed tomography?” In: *Current Opinion in Chemical Biology* 63, pp. 163–170.
- Sawall, S., J. Beckendorf, C. Amato, J. Maier, J. Backs, G. Vande Velde, M. Kachelrieß, and J. Kuntz (2020a). “Coronary micro-computed tomography angiography in mice”. In: *Scientific Reports* 10.1.
- Sawall, S., D. Franke, A. Kirchherr, J. Beckendorf, J. Kuntz, J. Maier, A. Kraupner, J. Backs, A. Briel, and M. Kachelrieß (2017). “In vivo quantification of myocardial infarction in mice using micro-CT and a novel blood pool agent”. In: *Contrast Media and Molecular Imaging* 2017.
- Sawall, S., L. Klein, C. Amato, and M. Kachelrieß (2020b). “Iodine contrast-to-noise ratio improvement at unit dose and contrast media volume reduction in a whole-body photon-counting CT”. In: *European Journal of Radiology* 1675.June, pp. 1–26.
- Sawall, S., J. Kuntz, C. Amato, L. Klein, E. Wehrse, L. T. Rotkopf, D. Franke, N. Gehrke, A. Briel, H.-P. Schlemmer, C. H. Ziener, S. Heinze, and M. Kachelrieß (2020c). “Ultrahigh resolution whole body photon counting CT: a novel versatile
-

-
- tool for translational research from mouse to man”. In: *European Molecular Imaging Meeting*.
- Schlomka, J. P., E. Roessl, R. Dorscheid, S. Dill, G. Martens, T. Istel, C. Bäumer, C. Herrmann, R. Steadman, G. Zeitler, A. Livne, and R. Proksa (2008). “Experimental feasibility of multi-energy photon-counting K-edge imaging in pre-clinical computed tomography”. In: *Physics in Medicine and Biology* 53.15, pp. 4031–4047.
- Shahid, I., E. Lancelot, and P. Desché (2020). “Future of Diagnostic Computed Tomography: An Update on Physicochemical Properties, Safety, and Development of X-ray Contrast Media”. In: *Investigative radiology* 55.9, pp. 598–600.
- Sitharaman, B., K. R. Kissell, K. B. Hartman, L. A. Tran, A. Baikalov, I. Rusakova, Y. Sun, H. A. Khant, S. J. Ludtke, W. Chiu, S. Laus, E. Tóth, L. Helm, A. E. Merbach, and L. J. Wilson (2005). “Superparamagnetic gadonanotubes are high-performance MRI contrast agents”. In: *Chemical Communications* 31, pp. 3915–3917.
- Symons, R., T. E. Cork, M. N. Lakshmanan, R. Evers, C. Davies-Venn, K. A. Rice, M. L. Thomas, C. Y. Liu, S. Kappler, S. Ulzheimer, V. Sandfort, D. A. Bluemke, and A. Pourmorteza (2017a). “Dual-contrast agent photon-counting computed tomography of the heart: initial experience”. In: *International Journal of Cardiovascular Imaging* 33.8, pp. 1253–1261.
- Symons, R., B. Krauss, P. Sahbaee, T. E. Cork, M. N. Lakshmanan, D. A. Bluemke, and A. Pourmorteza (2017b). “Photon-counting CT for simultaneous imaging of multiple contrast agents in the abdomen: An in vivo study”. In: *Medical Physics* 44.10, pp. 5120–5127.
- Taguchi, K. and J. S. Iwaczyk (2013). “Vision 20/20: Single photon counting x-ray detectors in medical imaging.” In: *Medical physics* 40.10, p. 100901.
- Willeminck, M. J., M. Persson, A. Pourmorteza, N. J. Pelc, and D. Fleischmann (2018). “Photon-counting CT: Technical principles and clinical prospects”. In: *Radiology* 289.2, pp. 293–312.
- Yeh, B. M., P. F. FitzGerald, P. M. Edic, J. W. Lambert, R. E. Colborn, M. E. Marino, P. M. Evans, J. C. Roberts, Z. J. Wang, M. J. Wong, and P. J. Bonitatibus (2017). “Opportunities for new CT contrast agents to maximize the diagnostic potential of emerging spectral CT technologies”. In: *Advanced Drug Delivery Reviews* 113, pp. 201–222.
- Yu, L., J. A. Christner, S. Leng, J. Wang, J. G. Fletcher, and C. H. McCollough (2011). “Virtual monochromatic imaging in dual-source dual-energy CT: Radiation dose and image quality”. In: *Medical Physics* 38.12, pp. 6371–6379.
- Yu, L., X. Liu, and C. H. McCollough (2009). “Pre-reconstruction three-material decomposition in dual-energy CT”. In: *Medical Imaging 2009: Physics of Medical Imaging* 7258.March 2009, p. 72583V.

- Yu, Z., S. Leng, S. M. Jorgensen, Z. Li, R. Gutjahr, B. Chen, A. F. Halaweish, S. Kappler, L. Yu, E. L. Ritman, and C. H. McCollough (2016a). “Evaluation of conventional imaging performance in a research whole-body CT system with a photon-counting detector array”. In: *Physics in Medicine and Biology* 61.4, pp. 1572–1595.
- Yu, Z., S. Leng, Z. Li, A. F. Halaweish, S. Kappler, E. L. Ritman, and C. H. McCollough (2016b). “How low can we go in radiation dose for the data-completion scan on a research whole-body photon-counting computed tomography system”. In: *Journal of Computer Assisted Tomography* 40.4, pp. 663–670.

9 | Personal Publications

This project was conducted as part of the Eurostars project E!11793 MultiContrastPhotonCT.

Parts of this thesis have been published in the following journal article and conference contributions:

Journal Articles.

Sawall, S., Klein L., Wehrse E., Rotkopf L. T., **Amato** C., Maier J., Schlemmer H. P., Ziener C. H., Heinze S., and Kachelrieß M. (2021). Threshold-dependent iodine imaging and spectral separation in a whole-body photon-counting CT system. *European Radiology*, 31(9), 6631–6639.

Sawall, S., **Amato** C., Klein L., Wehrse E., Maier J., and Kachelrieß M. (2021). Toward molecular imaging using spectral photon-counting computed tomography? *Current Opinion in Chemical Biology*, 63, 163–170.

Amato, C., Klein L., Wehrse E., Rotkopf L. T., Sawall S., Maier J., Ziener C. H., Schlemmer H. P., and Kachelrieß M. (2020). Potential of contrast agents based on high-Z elements for contrast-enhanced photon-counting computed tomography. *Medical Physics*, 47(12), 6179–6190.

Sawall, S., Klein L., **Amato** C., and Kachelrieß M. (2020). Iodine contrast-to-noise ratio improvement at unit dose and contrast media volume reduction in a whole-body photon-counting CT. *European Journal of Radiology*, 1675(June), 1–26.

Sawall, S., Beckendorf J., **Amato** C., Maier J., Backs J., Vande Velde G., Kachelrieß M., and Kuntz J. (2020). Coronary micro-computed tomography angiography in mice. *Scientific Reports*, 10(1).

Klein, L., Dorn S., **Amato** C., Heinze S., Uhrig M., Schlemmer H. P., Kachelrieß M., and Sawall S. (2020). Effects of Detector Sampling on Noise Reduction in Clinical Photon-Counting Whole-Body Computed Tomography. *Investigative Radiology*, 55(2), 111–119.

Journal Articles in Preparation.

Amato, C., Kuntz J., Maier J., Sawall S., Gehrke N., Franke D., Thüring T., and Kachelrieß M. (In preparation 2022). Characterization of a novel bismuth-based contrast agent for micro-CT.

Conference Contributions.

Trapp, P., Vöth T., **Amato** C., Sawall S., and Kachelrieß M. (2022). DeepRAR: A CNN-based approach for CT and CBCT ring artifact reduction. *SPIE Medical Imaging Conference (SPIE 2022)*.

Sawall, S., Klein L., Wehrse E., **Amato** C., Maier J., Ziener C. H., Schlemmer H. P., Heinze S., and Kachelrieß M. (2021). Dose reduction in photon-counting CT by ultra-high resolution acquisitions compared to today's iterative reconstructions: Combined benefits of the "iodine effect" and the "small pixel effect". *European Congress of Radiology 2021*.

Amato, C., Klein L., Maier J., Sawall S., Gehrke N., Franke D., Gkoumas S., Thüring T., Briel A., Brönnimann C., and Kachelrieß M. (2020). Decomposition of Multiple Contrast Agents in Photon-Counting Micro-CT: Iodine and Bismuth. *International Conference on Image Formation in X-Ray Computed Tomography 2020*.

Amato, C., Klein L., Maier J., Sawall S., Gehrke N., Franke D., Gkoumas S., Thüring T., Brönnimann C., and Kachelrieß M. (2020). Potential of High-Z Elements in Photon-Counting Micro-CT for Optimized Material Decomposition. *European Molecular Imaging Meeting 2020*.

Sawall, S., Kuntz J., **Amato** C., Klein L., Wehrse E., Rotkopf L. T., Franke D., Gehrke N., Briel A., Schlemmer H. P., Ziener C. H., Heinze S., and Kachelrieß M. Ultrahigh resolution whole-body photon-counting CT. A novel versatile tool for translation research from mouse to man. (2020). *European Molecular Imaging Meeting 2020*.

Kuntz, J., **Amato** C., Klein L., Maier J., Franke, Gehrke N., Briel A., Vande

Velde G., Kachelrieß M., and Sawall S.. (2020). In-vivo coronary micro-computed tomography angiography in mice. European Molecular Imaging Meeting 2020.

Klein, L., Wehrse E., **Amato** C., Ziener C.H., Uhrig M., Heinze S., Schlemmer H. P., Kachelrieß M., and Sawall S. (2020). Context-sensitive ultra high resolution bone imaging in whole-body photon-counting CT. European Congress of Radiology 2020.

Sawall, S., Klein L., **Amato** C., Wehrse E., Maier J., Schlemmer H. P., Ziener C. H., Heinze S., and Kachelrieß M. (2020). Threshold-dependent dual energy performance and spectral separation in a clinical whole-body photon-counting CT. European Congress of Radiology 2020.

Trapp, P., Klein L., Maier J., **Amato** C., Ballach F., Hammer M., Christoph R., Leinweber C., Sawall S., Christoph R., and Kachelrieß M. (2020). Benefits of photon counting detectors for beam hardening artifact reduction in industrial CT applications. 10th Conference on Industrial Computed Tomography (iCT Conference 2020).

Klein, L., Wehrse E., Rotkopf L., **Amato** C., Maier J., Schlemmer H. P., Ziener C. H., Heinze S., Kachelrieß M. and Sawall S. (2020). Strategien zur Dosisoptimierung in der Photonenzählenden Ganzkörper-Computertomographie. 51. Jahrestagung der Deutschen Gesellschaft für Medizinische Physik (DGMP 2020).

Klein, L., Dorn S., **Amato** C., Maier J., Heinze S., Uhrig M., Schlemmer H. P., Kachelrieß M. and Sawall S. (2019). Detektorabtastung und Dosisreduktion in der Photonenzählenden Computertomographie – Eine Phantom- und Ex-Vivo-Studie. 50. Jahrestagung der Deutschen Gesellschaft für Medizinische Physik 2019.

Sawall, S., Klein L., Dorn S., **Amato** C., Maier J., Faby S., and Kachelrieß M. (2019). Scan protocol design and k-edge imaging in a clinical whole-body photon-counting CT. 105th Scientific Assembly and Annual Meeting of the Radiological Society of North America (RSNA) Chicago (2019).

Klein, L., Dorn S., **Amato** C., Maier J., Heinze S., Uhrig M., Schlemmer H. P., Kachelrieß M., and Sawall S. (2019). Detector sampling and dose reduction in whole-body photon counting computed tomography. 105th Scientific Assembly and Annual Meeting of the Radiological Society of North America (RSNA) Chicago (2019).

10 | Curriculum Vitae

Personal Information

Name: Carlo Amato
Date of birth: 12.01.1993
Place of birth: Scorrano (Italy)
Nationality: Italian
Marital Status: Single

School

SEP 1999 - JUN 2004 Elementary school "Don Bosco" Corsi (Italy)
SEP 2004 - JUN 2007 Middle school "Edmondo De Amicis" Corsi (Italy)
SEP 2007 - JUN 2012 High school "Leonardo Da Vinci" Maglie (Italy)
11 JUL 2012 High School final exam. Grade 100/100

University

SEP 2012 - JUL 2015 Bachelor degree in physics at the University of Pisa. Grade: 110/110 cum laude. Thesis title: "Dissolution dynamic nuclear polarization in risonanza magnetica" under the supervision of Prof. Michele Emdin.

SEP 2015 - DEC 2017 Master degree in Physics at the University of Pisa with curriculum in medical physics. Grade: 110/110 cum laude. Thesis title: "Helium-beam radiography and spatial resolution improvements" under the supervision of Prof. Alberto Del Guerra and Dr. Maria Martisikova.

OCT 2018 - DEC 2021 Ph.D. student in medical physics at the German Cancer Research Center under the supervision of Prof. Marc Kachelrieß. Thesis title "Novel Contrast Agents in Photon-Counting Computed Tomography".

11 | Acknowledgements

I would like to thank all the people who helped and supported me during my research.

First of all, I would like to express my gratitude to Prof. Dr. Marc Kachelrieß for letting me join his group at DKFZ and for guiding me during my research.

Thanks to Dr. Stefan Sawall, Dr. Joscha Maier and Dr. Jan Kuntz for their invaluable advice and for the fruitful discussions we had during the past three years.

A special thank goes to Dr. Thomas Thüring, Dr. Danielle Franke and Dr. Nicole Gehrke for the great collaboration we managed to establish between DKFZ, NanoPet Pharma and Dectris.

I am grateful to all my colleagues, old and new. Together we created a nice and relaxed environment, which has been very pleasant to work in.

I would like to thank all my friends from Heidelberg, Pisa and Lecce for their constant support.

Infine, vorrei ringraziare la mia famiglia per essermi sempre stata vicina quando ne avevo bisogno.

12 | Eidesstattliche Erklärung

1. Bei der eingereichten Dissertation zu dem Thema “Novel Contrast Agents in Photon-Counting Computed Tomography” handelt es sich um meine eigenständig erbrachte Leistung.
2. Ich habe nur die angegebenen Quellen und Hilfsmittel benutzt und mich keiner unzulässigen Hilfe Dritter bedient. Insbesondere habe ich wörtlich oder sinngemäß aus anderen Werken übernommene Inhalte als solche kenntlich gemacht.
3. Die Arbeit oder Teile davon habe ich bislang nicht an einer Hochschule des In- oder Auslands als Bestandteil einer Prüfungs- oder Qualifikationsleistung vorgelegt.
4. Die Richtigkeit der vorstehenden Erklärung bestätige ich.
5. Die Bedeutung der eidesstattlichen Versicherung und die strafrechtlichen Folgen einer unrichtigen oder unvollständigen eidesstattlichen Versicherung sind mir bekannt. Ich versichere an Eides statt, dass ich nach bestem Wissen die reine Wahrheit erkläre und nichts verschwiegen habe.

Heidelberg, January 5, 2022


(Carlo Amato)